TOWARDS ENABLING SHAPE MEMORY CERAMICS: CONSIDERATIONS FOR STRESS CONCENTRATION OPTIMISATION THROUGH ADDITIVE MANUFACTURING.

RAUT VIRAG SANATAN

PhD

The Hong Kong Polytechnic University

2021

The Hong Kong Polytechnic University

Department of Electrical Engineering.

Towards enabling shape memory ceramics: considerations for stress concentration optimisation through additive manufacturing.

Raut Virag Sanatan

A thesis submitted in partial fulfilment of the requirements for the degree of Doctor of Philosophy

January 2020

CERTIFICATE OF ORIGINALITY

I hereby declare that this thesis is my own work and that, to the best of my knowledge and belief, it reproduces no material previously published or written, nor material that has been accepted for the award of any other degree or diploma, except where due acknowledgement has been made in the text.

Some of the work in this thesis has been reported in the following publication.

V. S. Raut, T. S. Glen, H. A. Rauch, H. Z. Yu, and S. T. Boles: Stress-induced phase transformation in shape memory ceramic nanoparticles. *J. Appl. Phys.* **215109**(November) (2019).

Virag S Raut

30th January 2020.

Abstract

The shape memory effect observed in ceramics is of particular interest for various applications, especially for those with extreme environments where ceramic materials offer unique advantages over metallic materials. The shape memory effect depends on the capability of the structure to withstand the critical stress required to initiate an underlying martensitic transformation. However, in bulk-scale applications the brittle nature of polycrystalline ceramics often leads to excess stress accumulation at the grain boundaries, ultimately leading to fracture. The pre-mature fracture arrests the capability of the material to initiate the martensitic transformation.

In this work, it is proposed that an engineered microstructure will lead to amplified stress levels in the bulk of the material. The approach can suppress the occurrence of pre-mature brittle fracture and promote higher stresses that lead to phase transformation. A slurry-based technique is employed that uses a combination of additive manufacturing and tape casting to fabricate ceramic structures. The mesostructure that is developed (post thermal treatment) is a network of pores that act as stress concentrators due to the reduced cross-sectional area while undergoing compression. This thereby increases the probability of nucleation of the monoclinic phase, reduces the stress gradient between pores, and approaches oligocrystallinty, which is known to enhance transformation capabilities. Finite element analysis is used to further verify and confirm the effect of porosity on stress evolution during loading.

Furthermore, thermally treating ceramic powders shows that a gradual transition of rounded smooth-edged particles to sharp faceted edges occurs prior to the growth of the particle size. The effect of these microstructural changes on the stress-induced phase transformation in compacted pellets is investigated. The effect of the combination of peak temperature and dwell time during

thermal treatment on the total tetragonal phase recovery is explored to complete the shape memory effect cycle for these ceramic materials.

Cumulatively, this work shows how the aid of stress concentrators, either with porosity in bulk structures or particle shape in powders, can control and increase the phase transformation ability in shape memory ceramic materials. However, significant further work remains for both the slurry based and powder-based techniques to optimise the stress-induced phase transformation and realise it in real-world applications. This optimisation may be ideal for newly evolving methods stemming from additive manufacturing methods for ceramics.

Acknowledgements

During my time in PolyU, I had the pleasure to work with many individuals that broadened my outlook immensely. First and foremost, I would like to sincerely thank my advisor, Dr Steven T Boles for his kind and gentle guidance throughout the journey. His advice ensured the work had a perfect blend of both scientific and engineering aspects of this field. I would also like to thank him, especially for extending his support towards my entrepreneurial and hall tutor work.

I would also like to thank our collaborator Dr Hang Z Yu and Mr Hunter Rauch at Virginia Tech for the support they offered during the entire course of this project. The interactions over Skype provided helpful guidance with the work and also in answering essential questions.

Also, I would like to offer my gratitude to my past and present research group colleagues, Dr. Tom S Glen, Dr Mohammad Tahmasebi, Li Bei, Ran Sijia and Tianye Zhang. Thanks to Dr Kwok-ho Lam and his research group members for providing access to the high-temperature furnaces. I also appreciate the support provided by Dr A-ping Zhang and his research group members in developing SU-8 photocurable ceramic slurry.

The support provided by Hardy and Pei at the UMF/MRC in both XRD and SEM characterisation helped immensely in moving forward with the work. Also, thanks to Mr Lau from the department of ISE for his generous help with the mechanical testing equipment.

Besides research, as the residential hall tutor, I was involved in providing pastoral care and promoting mental health awareness for which I am greatly indebted to both the wardens, Dr Lit Siu Wai and Dr Mimi Li and all present and past tutor colleagues.

Of course, thanks to friends and associates who were always supportive and stayed in touch during this period. It would had been tough without you guys.

Lastly, my parents, no words can describe or thank the sacrifices you both have made in ensuring I reach this level for which I am eternally grateful. It was their support that counted the most in providing mental and emotional stability throughout this journey.

Table of Contents

Table of figures

Acronyms

SME Shape Memory Effect

CZ 12% (mole) Ceria doped Zirconia $Ce_{0.12}Zr_{0.88}O_2$

SEM Scanning Electron Microscopy

XRD X-ray Diffraction

TEM Transmission Electron Microscopy

AM Additive Manufacturing

P3P Pseudo-3D printing process

MP3P Modified Pseudo-3D printing process

PCP Powder Compressed Pellet

SPS Spark Plasma Sintering

CAD Computer Aided Design

FEA Finite Element Analysis

Chapter 1 Introduction

Section 1.1: Ceramics

Background

Ceramics are used in various engineering applications which harness the materials mechanical properties that are better than metals or polymers and is observed in Figure 1. Besides, ceramics are also stable at high temperature and are non-corrosive when exposed to chemical environments, etc. The material is used in applications like automotive, manufacturing, semiconductor, refractory and also as dishware in consumer applications [1]–[3]. It is observed in Ashby's chart (Figure 1) that the Young's modulus of ceramic materials is high compared to metals and polymers.

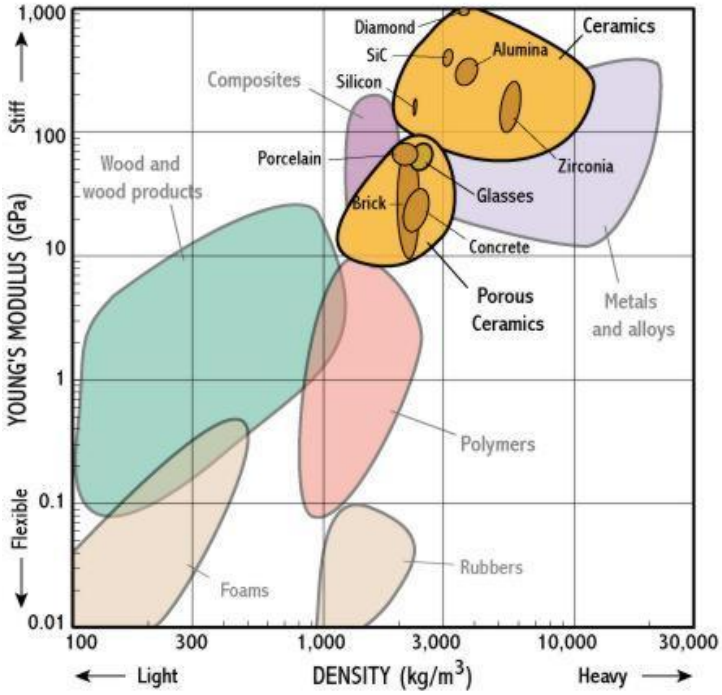

Figure 1 Ashby chart comparing Young's modulus with density of various materials [4].

Ceramics can generally be classified into traditional and advanced ceramics. The atomic bonds in ceramics, are either ionic and/or covalent bonds between non-metallic (O, N, C), semi-metallic (Si, B) and (Al, Mg, Na, Ti, W) [5]. However, the lack of free electrons in the outermost orbit as in the case of metallic systems, makes it a poor electrical and thermal conductor [5]. The high strength in the material due to the ionic and covalent bonds as compared to metallic bonds gives the material high strength, high elastic modulus, high melting point and temperature and chemical stability [5]. However, the material, being elastic in nature, undergoes brittle fracture above the failure point due to the inability to accommodate the energy associated with further displacement (i.e. strain). Covalent bonding at the atomic level results in hindered formation/motion of dislocations in the bulk material and further gives rise to the preference for new surface formation. Hence, ceramics rarely exhibit plasticity via dislocations [3] and instead display crack formation and propagation characteristic of brittle fracture when displacement cannot be accommodated elastically.

Zirconia

Zirconia has a broad range of mechanical properties like the elastic modulus is ~200 GPa, Vickers hardness is ~10.7 GPa, fracture toughness is up to 7-8 MPa $m^{1/2}$ besides being mechanically stable at high temperature and in corrosive environments [6]. Due to these properties, it is used in several engineering applications [7]–[10]. Zirconia has four pure phases, monoclinic, tetragonal, cubic and orthorhombic. The orthorhombic phase is only observed only under pressure. At ambient pressure, the material is stable in the monoclinic phase and remains stable up to 1205°C. Above 1205°C the tetragonal phase is stable and remains so up to 2377°C. Between 2377°C and 2710°C a cubic phase becomes preferred, and this holds true until the material reaches its melting point at approximately 2710°C [9]. The phase transformation between the tetragonal and the monoclinic phase is accompanied by large volume change. This results in the formation of cracks in the structure, and

therefore, in the pure phase, it is impossible for zirconia to be used as an engineering material in any applications.

Graphical representation of monoclinic and tetragonal unit cell in Figure 2.

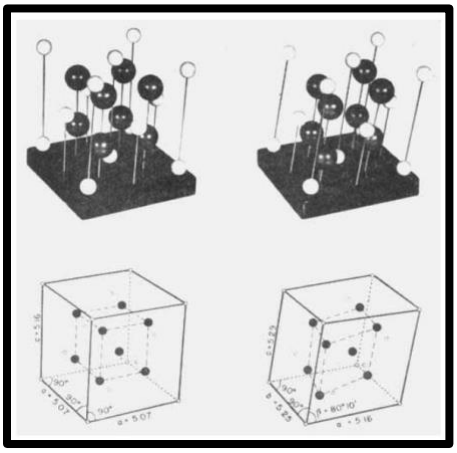

Figure 2 Tetragonal (left) and monoclinic (right) unit cell of zirconia [11].

The addition of rare earth elements like yttria, ceria, magnesia, calcia, etc. stabilises the tetragonal phase in zirconia at room temperature. The doping lowers the chemical-free energy of the tetragonal phase relative to the monoclinic phase as a function of temperature and solute content at room temperature [12]. The tetragonal phase has properties superior to that of the monoclinic phase, and therefore the doped compositions of zirconia can be used in different applications.

Based on the applications to be used, several doped compositions of zirconia exist like partially stabilised zirconia (PSZ), tetragonal zirconia polycrystalline (TZP), monoclinic polycrystalline zirconia (MPZ), calcium-cation-doped PSZ generally (Ca-PSZ and CaO-PSZ) and magnesium-cation-doped PSZ (Mg-PSZ and MgO-PSZ) [13].

An interesting mechanism that is observed in the doped compositions of zirconia is the martensitic transformation and this transformation enhances the properties of the material.

Martensitic transformation

This transformation was first discovered in steel wherein heating the low carbon steel to the austenite phase and rapidly cooling in cold water (quenching) lead to the transformation from the austenite phase to the martensite phase. This transformation is diffusionless, referred to as "military transformation" for its long-range systematic formation of a transformed crystal structure. The speed of this transformation can be compared to the speed of sound and the resulting crystal structure gives the material superior mechanical properties as compared to the properties before the phase transformation.

The martensitic transformation is observed in zirconia as well. The austenite phase is the tetragonal phase and the martensitic phase is the monoclinic phase. The mechanism of the martensitic transformation in doped zirconia is still a debated field and is explained in either the context of the classical heterogeneous nucleation theory or in the context of localised soft mode theory [14]. However, in both cases, the martensitic transformation is observed to be favoured in the regions that show local stress concentration and free surfaces [14].

The phase transformation in doped ZrO_2 compositions is facilitated by either stress or temperature, leading to the transformation of the austenite phase (tetragonal) to the martensite (monoclinic) phase and vice versa.

In doped zirconia, the tetragonal to monoclinic phase transformation is governed by the following free energy equation.

$$\Delta G_{T\rightarrow M} = \Delta G_c + \Delta U_{se} + \Delta U_s$$

Equation 1

Where, $\Delta G_{T\rightarrow M}$ is the free energy associated with the tetragonal to monoclinic phase transformation, ΔG_c is the chemical-free energy between the tetragonal and monoclinic phase, ΔU_{se} refers to the change in elastic strain energy as a result of the stress-induced phase transformation and ΔU_s is the energy associated with the formation of new interfaces, specifically concerning transformation toughening [15]. The doped composition of zirconia which occurs in the tetragonal phase at room temperature retains the tetragonal phase at room temperature provided that $\Delta G_{T\rightarrow M} > 0$ this is in the case of

$$|G_c| < \Delta U_{se} + \Delta U_s$$

Equation 2

With the lowering of the chemical energy, elastic strain energy or energy associated with interfaces would lower the free energy of the material resulting in the transformation from the tetragonal to the monoclinic phase. ΔG_c can be further mathematically explained as a function of temperature *T*

$$\Delta G_c = \Delta S^{t\rightarrow m}(T_0 - T)$$

Equation 3

Where $\Delta S^{t\rightarrow m}$ is the change in entropy associated with the transformation and T_0 is the temperature at which the tetragonal phase begins to transform into the monoclinic phase [12]. The addition of ceria to zirconia lowers the T_0 or M_s temperature below *T*. In the case of *T* equals to room temperature, the composition would be metastable at room temperature. ΔU_{se} i.e. the change in the elastic strain energy is greater than 0. However, with the formation of strain the free energy associated would reduce and this would also reduce the $\Delta G_{T\rightarrow M}$.

The transformation of doped zirconia from the tetragonal phase to the monoclinic phase and vice versa on applications of external stimuli like stress, temperature, etc. forms the basis of shape memory behaviour in ceramics.

Shape memory ceramics

Smart materials are a unique set of materials which exhibit structural changes upon application of a stimuli like electric field, magnetic field, stress, moisture and temperature [16]. Shape memory alloys, electroactive polymers, magnetorheological fluids and piezoceramics are different types of smart materials which have a wide range of applications. Upon application of stress, a shape memory ceramic undergoes elastic deformation, but in the case of the stress reaching critical levels, the formation of shear strain leads to atomic rearrangement resulting in plastic deformation of the crystal structure. The change in elastic strain energy lowers the free energy of the system associated with the tetragonal to monoclinic phase transformation. In the case of the shape memory effect, when the structure is compressed at stress above the critical stress levels threshold, the crystal structure undergoes a rearrangement and this deformation is retained upon removal of the stress viz. plastic deformation. The strain developed during this phase transformation needs to be accommodated especially in the case of polycrystalline dense ceramics to avoid the occurrence of accumulation at the grain boundaries. The transformed phase can be recovered by thermally treating the material and recovering the original shape. In the case of material that exhibits superelasticity, upon application of stress, the structure deforms but the shape can be easily recovered upon removal of the stress.

The material investigated in this study is 12% (mole) ceria doped zirconia (CZ) which exhibits the shape memory effect in the intermediate regime. The other compositions in this family that exhibit smart material behaviour includes 16% (mole) ceria doped zirconia in the superelastic regime and

10% (mole) ceria doped zirconia in the shape memory regime. CZ is metastable at room temperature and undergoes a stress-induced phase transformation from the tetragonal phase (austenite) to the monoclinic phase (martensite) and the transformation is irreversible upon removal of the stress. Thermally treating the deformed structure reverses the phase transformation and leads to recovery of the tetragonal phase. This effect is graphically represented in Figure 4.

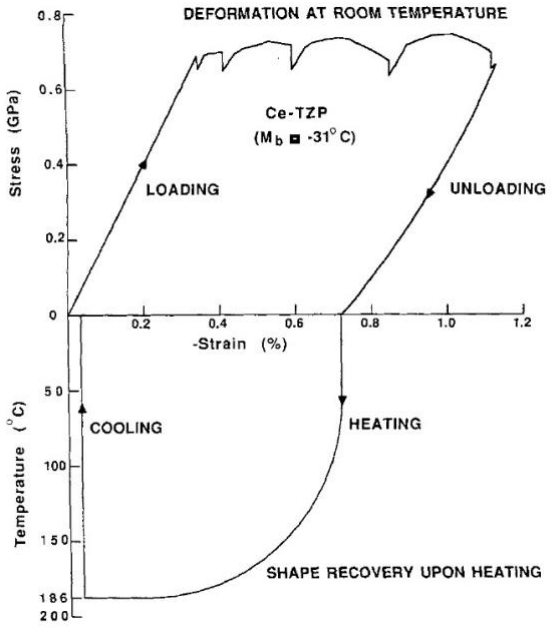

Figure 3 Stress and strain curve during uniaxial compression at room temperature and thermal-induced transformation at elevated temperature. Figure taken from reference [17].

As mentioned previously, the strain that is produced in the grains during transformation can lead to brittle fracture in polycrystalline ceramics. This was circumvented by producing micropillars with free surfaces that could accommodate the strain and also mitigate excess stress accumulation at grain boundaries often the cause for brittle fracture by Lai et al. [18] in yttria stabilised zirconia. This effect is shown in Figure 4.

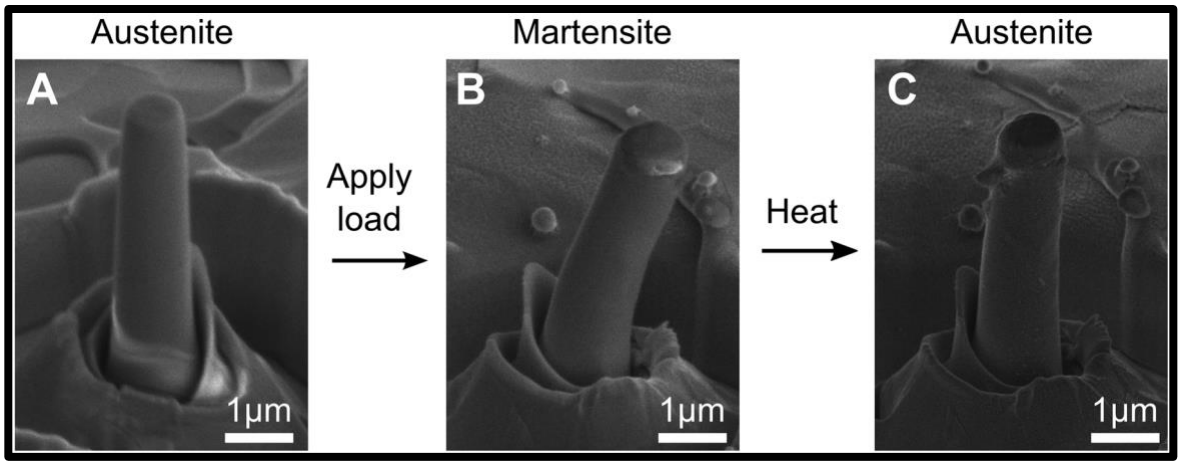

Figure 4 Deformation in pillar from austenite to martensite and back to austenite phase was repeated for 50 cycles on single pillar [18].

The micropillars (~ 1 μm diameter) of zirconia doped with either ceria (CZ) or yttria (YSZ) were observed to withstand strains as high as 7% for 50 cycles exhibiting the stress and thermal-induced SME [18]. Further investigations into YSZ and titania doped zirconia micropillars by Zeng et al. [19] revealed a relationship between crystal orientation and martensitic transformation ability: The critical stress level required for nucleation and growth of the monoclinic phase was observed to vary systematically for different orientations during stress-induced transformation. Orientation dependence was also investigated in 16% (mole) ceria doped zirconia particles by Du et al. [20] which showed that oligocrystalline and monocrystalline particles could withstand cyclic superelasticity (over 100 for monocrystalline), but polycrystalline particles underwent fracture before sustaining the critical stress.

A substantial part of the pioneering work in characterising the martensitic transformation behaviour in ZrO_2 used conventional processing techniques like pressing (hot or cold). But the studies involved with the processing of ceramics has also been evolving, which includes tape casting and 3D printing [21]–[23]. For high production volumes Du, et al. proposed spray drying

slurry of zirconia and ceria particles which exhibit superelasticity [20]. A step further to spray drying is modified sol-gel process which was used to produce highly monodisperse spherical ceria doped zirconia particles [24]. Superelasticity was characterised in the modified sol-gel process over 500 strain cycles [24]. Xueying, et al. showed stress and thermal-induced phase transformation in porous 14.4% (mole) ceria doped zirconia foams made using ice templating with 12% (vol.) solid loading [25]. Yu et al. [26] showed granular packing of shape memory or superelastic ceramics that can be used over multiple cycles and can be used in energy harnessing applications.

Such work reiterates the need for focusing on processing science by leveraging the morphology of the material [27]. It would be advantageous to control the material at the microscopic level in order to show the shape memory behaviour at the bulk scale, primarily by mitigating the brittle nature of zirconia. In polycrystalline ceramics Chiu, et al. showed stress concentration occurring at grain corner and edges of grain [28], [29]. Gremillard showed the addition of silica phase at grain boundaries reduces the possibility of low-temperature degradation (martensitic transformation in a moist atmosphere [15]) and delays crack propagation[30].

Section 1.2: Process – Additive manufacturing

Manufacturing can broadly be classified into, additive and subtractive manufacturing. Subtractive manufacturing involves producing individual parts from a block of material by processes like turning, milling, etc. and this constitutes the top-down approach. Ceramics are largely processed using conventional techniques like pressing, casting or subtractive manufacturing. The ceramic structures made using casting are further subjected to post-processing according to the shape needed. This limits the design flexibility that is required to produce complex geometries. AM offers advantages over other techniques and is explored to mitigate problems occurring in

conventional processing techniques for ceramics. AM involves building up parts layer by layer in sequence, curing or sintering a single layer at a time. This approach constitutes the bottom-up approach and by using this method, inter-linked parts can be fabricated as one single structure eliminating the need for assembly to be done at a later point.

A graphical representation of the two processes is shown in Figure 5 in which the difference in top-down and bottom-up approach seen in both subtractive and additive manufacturing, respectively, is seen.

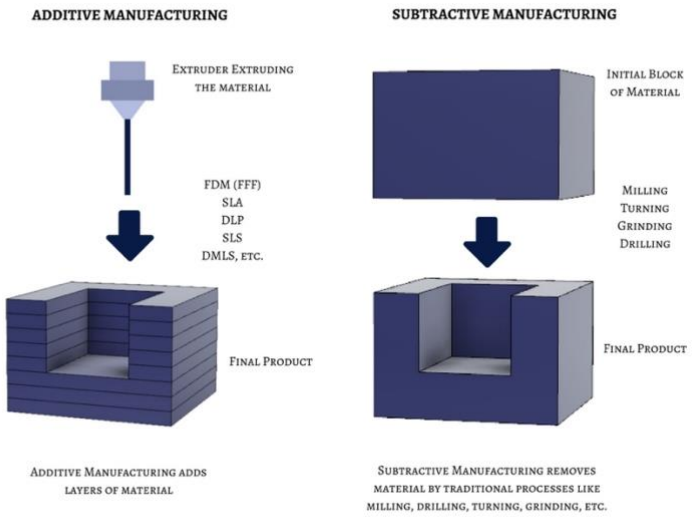

Figure 5 Comparison between additive and subtractive manufacturing [31].

It is vital for the increased adaptation of the 3D printing technology that most of the engineering materials can be integrated into this process. The 3D printing industry at present is primarily focused on plastic parts and some metal alloys. 3D printing of ceramics is still at the nascent stage and the limited use has production issues. To fully realise the potential of 3D printing, it is necessary to be able to print structures of desired industrial quality using functional materials. Technical ceramics like zirconia, alumina, silicon nitride, and silicon carbide have engineering

applications like refractory lining, dentistry, cutting tools, oxygen sensors, fuel cells and turbine blades which can be used to 3D print parts for the mentioned applications [32]–[36].

AM which solves limitations of traditional processing techniques was developed with the primary motivation to reduce time to market of new ceramic products [37]. Further to that, integrating shape memory behaviour in additively manufactured ceramic products would provide possible solutions for critical problems [38], [39]. There are many methods to cure or sinter the structure, especially for polymer-based raw materials which are used extensively in the industry to manufacture parts.

AM of ceramics can broadly be classified into powder-based and slurry-based techniques. In the case of the powder-based method, a high-power laser is used to selectively cure a single layer of ceramic powder which is followed by depositing a fresh new layer of uncured ceramic powder. To increases the efficiency, ceramic powder is mixed with polymer granules for effective curing. However, in the case of ceramics, sintering is an inevitable part in post-processing that actually ensures the development of ceramic properties at elevated temperatures due to the formation of a microstructure at the said temperature. Due to this, it becomes necessary to have a high-powered laser that could produce the desired sintering effect at the spot during curing. This may not be an economical way since the cost of a high-powered laser would significantly increase the cost of production. Contrary to this, in the case of slurry-based techniques, the slurry consists of polymer, solvent, photopolymerisation species that can be easily eliminated with low-temperature thermal processing. In the case of the slurry consisting of a high ceramic loading then with a homogenous distribution of the polymer and ceramic particles, parts can be fabricated with reasonably high accuracy and with the aid of two-stage thermal treatment dense ceramic parts can be fabricated.

This method is cost-effective since the UV light or laser required is low powered and the end product is quite effective. One such method is explained in the next section.

Stereolithography SLA micro SLA

In this method, the substrate is immersed in the slurry. The slurry, when exposed to either UV light or a laser, leads to cross-linking of the polymer in the slurry because of the photopolymerisation species. The curing occurs at the interface of the substrate and the slurry after which the substrate is raised by a certain increment. This increment is commonly lesser than equal to the slice thickness. The next slice is cured upon the interface formed between the slurry and the earlier cured surface. This process repeats until the entire part is fabricated. There are two types of light sources which are used in this method, either a laser or a UV light. In the experiments that were focused on characterising the cure depth (Appendix I), the light source apparatus consisted of a digital micromirror device (DMD) assembled in the printer (1024 by 768 pixels) and an ultraviolet lamp with 365 nm wavelength. The pixels are square in shape and each side measures 2.724 μm. An image reflected by a DMD is done by the array of pixels which reduces the distortion of the image. Hence, the laser sources of light are used for fabrication of macro parts and for micro parts, a DMD micromirror device having a resolution of < 3 microns is used to reflect the UV light. A better representation is provided of the two processes in Figure 6.

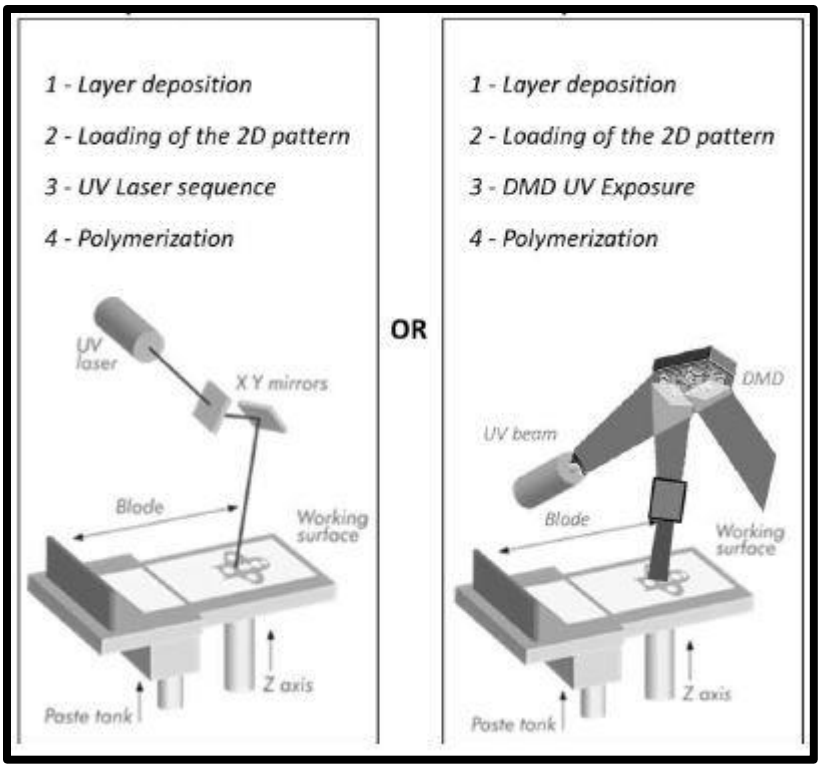

Figure 6 Picture on the left uses a laser to polymerise the slurry. The picture on the right in the figure above shows a DMD focusing UV light to cure the slurry [40].

Various other processes also come under the domain of AM but are not covered here for the lack of relevance they have with respect to the central theme of the thesis. The other processes are selective laser sintering (SLS)/ selective laser melting (SLM), fused deposition modelling (FDM), direct metal deposition (DMD), dough deposition modelling (DDM) and 3D printing (3DP) [41].

The 3D printing techniques for ceramics can broadly be classified into powder-based and slurry-based techniques.

Slurry based pseudo-3D printing technique

One of the negative photoresists used in stereolithography is Su-8. Developed by IBM in the year 1989 [42], Su-8 is used extensively in producing high aspect ratio structures in various engineering

applications. Su-8 is a negative photoresist and is used in the industry for producing high aspect ratio (HAR) structures using Ultraviolet light [43]. It also has a high amount of sensitivity to UV light and produces 3D models with high resolution. The photoresist also shows good thermal stability when exposed to large doses of UV light. A typical composition of Su-8 negative photoresist consists of the epoxy, solvent, a photoinitiator and a photo inhibitor. The process to fabricate structures is a comprehensive one in which curing time and temperature are varied depending upon the concentration and thickness of the Su-8 required [44]. The structures are cured by exposing a mask and selectively curing the exposed surface. The Su-8 is spin-coated followed by a two-stage prebake. Then it is exposed followed by a two-stage post bake which is also called a hard bake. After the post bake, the substrate is immersed in a developer to remove the uncured photoresist. The comprehensive procedure is graphically represented in Figure 7.

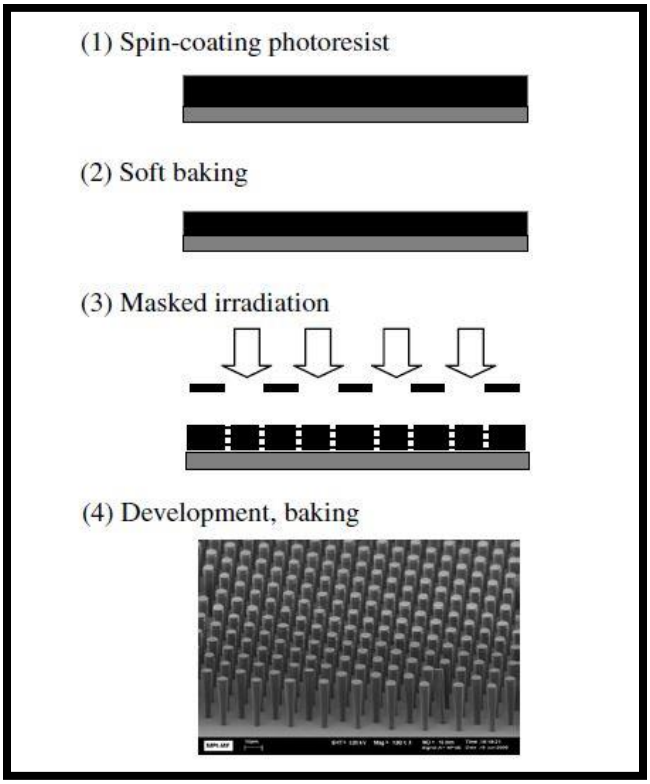

Figure 7 Graphical representation of Su-8 photopolymerisation process [32].

Stereolithography printers are largely used to fabricate polymer-based models. A combination of ceramics and a UV curable solution to extend the 3D printing from polymer to ceramics was attempted by Griffith with silica, alumina and silicon nitride [45]. In the work presented in this thesis, the volume percentage of zirconia and 12% (mole) ceria doped zirconia was 50% similar to gel casting of alumina developed as a means to mitigate problems from injection moulding and slip casting [46].

As the ceramic concentration increases above 40% (vol.) in the slurry, the viscosity is observed to increase by decades [47]. It is critical to have ceramic loading in slurry higher than 50% (vol.) to reduce cracking and produce structures with high density and low porosity. The increase in the viscosity often leads to light scattering due to the ceramic particles and a decrease in cure depth is inevitable for any given energy dosage. The light scattering leads to higher curing of the width of the ceramic structures as opposed to achieving higher cure depth.

In efforts to form bulk structures, the knowledge of the cure depth for a given dosage is necessary demanding control of light scattering. The observation made by Griffith et al. [45] has been experimentally shown by Gentry in that the energy dose required grows exponentially for increasing cure depth [48]. The exponential trend is demonstrated for suspensions containing silica, mullite, alumina and zircon.

Halloran has shown various techniques to characterise photopolymerisable slurry [49]. The curing process is largely exothermic, which is effectively analysed by differential scanning calorimetry (DSC) combined by the near IR spectroscopy [49].

The absorption effects of the suspension can be predicted theoretically by following the quasi Beer-Lambert relationship which involves parameters like sensitivity to UV light and critical

energy dose for both the width and the depth curing of the slurry [50]. The effect on the width and the depth also gets influenced by the light scattering and absorption of the slurry [51]. Griffith et al. also observed that the cure depth can be characterised by using the Beer-Lambert Law [45].

Chartier incorporated UV laser stereolithography to cure suspension of silica and polyester acrylate (PEAAM) and observed the influence of the rheology of the suspension on the cure depth and width [52]. In his findings, it is observed that for low ceramic loading (up to 10% (vol.) the rheology of the slurry does not influence the photopolymerisation process. As the volume percentage of ceramic increase, it becomes inevitable to take into account the particle-particle and particle-monomer linking with the separation of free radicals in the medium. This deaccelerates polymerisation rate of the resin and lowers the cure depth [52].

In the slurry-based pseudo-3D printing approach, cure depth for low ceramic loading slurry was characterised. This was to determine the approximate energy dosage required to cure the slurry.

The amount of slurry that gets cured is a function of energy dosage and the composition of the suspension [48], [50], [51], [53]. Since SU-8 is widely used for lithography, its processing parameters are well documented [44]. The depth of curing that can be obtained for a given dose of energy E is C_d taking into consideration that the resin shows Beer-Lambert dose dependence.

The energy dose (mJ/cm^2) required to cure the slurry is given by the intensity (I) (mW/cm^2) multiplied by the time (*t) (s)*.

$$E = I \times t$$

Equation 4

The amount of energy within the suspension at any given depth can be predicted using Equation 5. This prediction is for the resin, which follows the Beer-Lambert relationship and it can be understood that the energy dose attenuates logarithmically with depth (z) [48].

$$E(z) = E_0 \exp\left(\frac{-z}{S_d}\right) \quad (1)$$

Equation 5

Where E_0 is the energy dose at the surface and S_d is the resin sensitivity in the depth direction [48]. The slurry gets cured when the energy dosage is above or equal to the critical dose required for polymerisation (E_d). The cure depth of the slurry is given by the Beer-Lambert dose dependence

The depth of the slurry which gets cured by a given amount of energy dose can be predicted correctly by the Beer-Lambert.

$$C_d = S_d ln\left(\frac{E_0}{E_d}\right) \quad (2)$$

Equation 6

Equations 1, 2 and 3 have been taken from [48]. This information proved crucial during translation from the stereolithography setup to curing individual pellets using a UV lamp.

Since the stereolithography setup did not have a Z-axis movement, additional layers on top of the cured layer could not be produced. Characterisation of the cure depth was done using 16% (mole) ceria doped zirconia and the process in detail is listed in Section 7.1:.

The results from the cure depth characterised using the method mentioned in Section 7.1: was integrated along with the tape casting method to fabricate 12% (mole) ceria doped zirconia pillars. By using this modified AM technique referred to as pseudo-3D printing technique, an architected

mesostructure could be produced since pores which reduce the cross-section area can also act as stress concentrators [54]. Such work has been reported previously wherein Zhu, et al. employed finite element analysis using the Voronoi method and established that irregularly shaped foams have a higher tangential modulus than regular foams [55], [56]. Investigating the relationship between pores and material properties, S. Chung observed stress concentration occurs at the pore edges and the local stresses developed can cause early failure in the sample [57]. Similar observations were made by Simone, et al. that showed higher stress concentration around larger pores [58]. Simone, et al. [58] also noted that in aluminium foams, plastic deformation can occur even at a very low-stress level as seen by Kunze, et al. [59]. However, the subsequent stress-induced phase transformation as a function of stress that gets amplified around the pores in doped zirconia has not been explored.

Power-based additive AM technique

In powder-based AM techniques, a layer of powder is deposited and is selectively cured as per the slices using an energy source similar to stereolithography. Additional layers are deposited on top of each other and are selectively cured to form a 3D printed object. One of the key problem preventing the integration of AM in engineering applications is the strength of the part manufactured using AM [60], which is influenced by the microstructure [61]. Efforts to optimise the structural properties of parts manufactured using AM by Wilkes et al. [62] in which pre-processing or selectively heating of Al_2O_3-ZrO_2 before selective laser melting (SLM) curing produced a higher density structure. Yves-Christian et al. [63] also showed similar results by preheating Al_2O_3-ZrO_2 powder before curing them using SLM process in producing nano-sized microstructures with high flexural strength. Pre-processing would further strengthen the structures

and thereby aid in withstanding the critical stress required to initiate the martensitic transformation. This is in addition to the morphology or the shape of the particles of the material.

As mentioned earlier, besides the size of the structure, the shape of the particle also plays a vital role in achieving different stress levels while undergoing compression in the bulk. The shape of the particle influencing the microstructure of bulk granular materials and the mechanical properties has been an interesting subject of investigation [64]–[66]. Generally, the shape of the particles is characterised by measuring the roundness and sphericity [64], [67]–[69]. Several methods have been developed to characterise the sphericity and roundness of particles and subsequently relate them to the properties of the structures[66], [70]–[72]. Athanassiadis et al. [64] found that the contacts produced with shapes having corners and straight facets made using hard resins during compaction showed a higher scaling exponent of effective modulus as compared to smooth-edged shapes like spheres. Though the sphericity of spheres and cubes is similar [73], it is the facets that produce distinct contact types contributing to a higher scaling exponent of effective modulus [64].

Aside from granular systems, edges, facets and corners are known to play an important role in controlling stress concentrations in fully densified structures. Chiu [29] (reported by Becher et al.[12]) observed that stress concentration occurs on the corners and edges of the cuboidal shaped inclusion as well as grain corners [74] in ceramics, while similar observations have also been made in metallic systems [75]. The accumulation of various stresses at the edges and corners of cuboidal shaped inclusions and the concentration due to grain growth could provide the critical stress level required for nucleation in transformation [12]. Similar observations in sintered ceramics have been extensively studied in the past for the martensitic transformation, but the scope of these studies has been limited with respect to processing science [27].

Role of 3D printing in designing architected mesostructures

Though porosity plays an important role in stress concentration but designing the porosity in a systematic way and controlling it at the microscopic level is difficult and largely limited with the present state of the art in the 3D printing industry. This role has motivated the research community to invest resources over a long period of time in developing it. However, in the past few decades, AM has shown to be an effective alternative to conventional manufacturing techniques in producing parts and materials having microstructure with porosities that can be defined in terms of the pore fraction, shape, etc. The porosities can be produced with precision at various length scales and recent work has been focused on producing millimetre to centimetre sized porosity using AM [76].

In porous structures, the pores are of different kinds, open and closed pores, interconnected pores and this plays a crucial role in determining the properties of the material and the structure. The inspiration for this kind of work is largely taken from naturally occurring materials like wood, weed or cancellous bone which are hierarchically structured [77]. Such porous structures are extensively imitated to make products like implants or bone scaffolds [77]. However, it is not economical if feasible to make it using conventional processes like injection moulding and therefore, AM serves as a versatile alternative to manufacture such parts [77]. Commonly used techniques involve direct ink writing wherein small amounts of ink can be deposited to produce the desired shape [77]. Conventional techniques like direct foaming, sacrificial templating, partial sintering and using sacrificial fugitives focus on producing macro-sized pores but in tandem with 3D printing custom sized pores can be produced [77]. Garcia et al. produced complex scaffold materials with porosity ranging from 4 nm to 400 micrometres by combining sol-gel process consisting of surfactant that would provide nm-sized pores, biopolymer sacrificial templating to

achieve 30-80 micrometre pores and direct ink writing of a suitable past finally creating large 400-micrometre pores [77], [78]. The porosity produced using this approach was around 40%.

Also, powder-based 3D printing methods, layers of powder are spread layer by layer and each layer is selectively cured, which provides a higher degree of control in producing geometric shapes. This is besides the lower surface-volume ratio and larger pores that can be achieved because of the binders that can promote better bonding between particles inside the powder bed [79]. Keeping in mind such advancements, we believe that with the future progress in the field of AM it would be possible to produce materials and structure with more sophisticated microstructure. Here we have attempted to produced porosity of a certain fraction but with the infrastructure, the shape of the pore could not be controlled. Therefore, with the aid of FEA we have analysed stress optimisation as a result of different shapes of the pore.

Besides slurry and powder-based techniques there is another technique referred to as direct ink writing. This process is similar to extrusion based technique and is largely used in the case of meso- and micro-scales [80]. In this technique liquid-phase “ink” is dispensed through a nozzle and deposited layer by layer [80]. The rate of flow is controlled along a defined path in order to 3D print structures [80]. This technique is graphically represented in Figure 8.

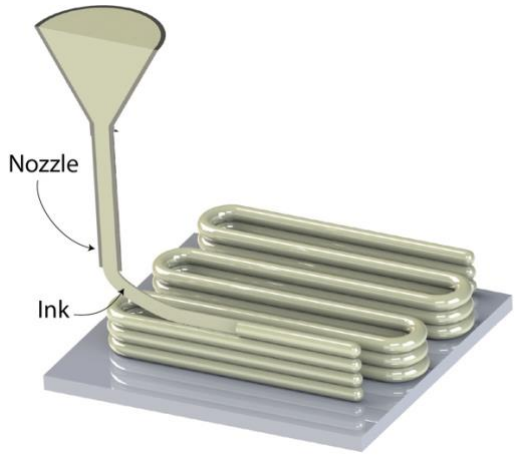

Figure 8 Direct ink writing process [80].

Section 1.3: Thesis outline and motivation

Thermal treatment of CZ powder and its subsequent stress-induced phase transformation.

Thermal treatment of the CZ particles showed changes in the morphology of the particles. Upon compression of this thermally treated powder a correlation was observed in the MC formed as a results of stress-induced phase transformation and the thermal treatment temperature. This behaviour was split between two regimes. The relation between the morphological changes and the MC is investigated in Chapter 3.

Thermal-induced martensitic transformation

The thermal-induced reverse phase transformation to recover the tetragonal phase in the pellets was investigated in Section 3.5:**.** The pellets were thermally treated at different peak temperature and the MC was calculated. Also, the dwell time at these peak temperatures were also varied to calculate the optimum peak temperature and dwell time combination for maximum tetragonal phase recovery.

Slurry based AM

Slurry based pseudo-3D printing techniques was used to fabricated P3P and MP3P pillars. Phase transformation on the surface was induced in these pillars using polishing and Vickers indentation to characterise the magnitude of transformation in both, large area as well as small confined areas. Further, the limitation of polycrystalline smart ceramic materials to undergo stress-induced phase transformation in the bulk can be solved by producing a network of pores in the bulk. The pores due to reduced cross-sectional area act as stress concentrators on the application of force and the structure as a whole have a high probability of producing a higher net stress-induced phase transformation. The approach and findings are discussed comprehensively in Chapter 4.

Characterisation of stress distribution around pores using FEA

With the present state of the art of 3D printing, producing accurate and precise microstructure with respect to porosity is a limitation. Here we have used CAD modelling and FEA to simulate the stress distribution around the pores. The stress levels would essentially aid in producing higher MC in the structure as a whole. By varying the shapes of the pores and the distance between them, we aim to focus on further increasing the optimised stress levels. With the help of this analysis, future work can be focused on producing architected pores that could produce higher stress-induced phase transformation as the 3D printing technology permits. This work is discussed in Chapter 5.

Chapter 2 Experimental methods.

12% (mole) ceria doped zirconia $Ce_{0.12}Zr_{0.88}O_2$ (CZ) is procured from Ganzhou Wanfeng Advanced Materials Co. Ltd. China. The agglomerations in the powder were removed by mixing with ethanol and heating the slurry to 150°C. The refined powder is then used for thermal treatment (discussed in Section 2.1:) and to make the slurry (discussed in Section 2.2:).

Section 2.1: Thermal treatment of CZ nanoparticles.

The CZ powder consists of particles that are monocrystalline of approximately 20 nm in diameter as determined by transmission electron microscopy (TEM). Smaller batches of the refined powder were then thermally treated in an alumina tube furnace at 300°C - 1300°C (with 100°C intervals) and 1550°C separately. The ramping rate used for thermal treatment 10°C/minute and the dwell time at each of the peak temperatures were 60 minutes. The furnace took approximately 5 – 8 hours to cool down to room temperature. Sample processed at liquid nitrogen temperature was wrapped in an aluminium foil and placed inside a flask filled with liquid nitrogen for 4 hours. In the case of in-situ XRD, CZ powder cooled using liquid nitrogen and diffraction pattern was obtained at 25°C, -100°C and -150°C which was the lowest stable temperature that can be achieved. One gram of refined CZ powder is then poured inside stainless-steel mould and then pressed at 250 MPa to make pellets.

Section 2.2: Slurry based pseudo-3D printing technique

The SU-8 negative photoresist is produced using EPON SU-8 resin (Momentive Ltd.), Tributylamine (TBA) (Meryer Chemical Technology Co., Ltd.) and PC-2506 (Polyset) as a photo inhibitor and ultraviolet polymerisation catalyst respectively. The resin and photopolymerisation species are then dissolved in cyclopentanone (CP) in a weight ratio of 103.15:0.14:2.58:100 (SU-

8 resin: TBA: PC-2506: CP). Slurry with a ceramic loading of 50% (vol.) is produced by mixing Su-8 negative photoresist with CZ using a magnetic stirrer setup. The slurry is then poured to fill the cavity of a washer placed on a quartz substrate (Figure 9 a). The substrate is then placed on a hotplate for the slurry to prebake at 65°C (solvent evaporation) for 30 minutes, followed by UV exposed for 123 minutes (UV curing of negative photoresist) and later post-baked at 65°C for 30 minutes (hard bake) (Figure 9 b).

Pseudo-3D printed (P3P) pillars

The pellets were later peeled off from the substrate and then stacked on top of each other with few drops of ethanol and acetone mixture between each pellet to promote adhesion. The ratio of acetone to ethanol was 1:100 in the mixture. Each pillar consists of pellets stacked on top of each other, as shown in Figure 10 (a) and pillar post-de-binding is shown in Figure 10 (b). Thermal treatment of the stacked pillar consisted of a two-stage process: (1) de-binding and (2) sintering at 1550°C; (See Figure 14 for temperature profile). Due to the manufacturing method of these pillars, 'pseudo-3D printed, P3P' is used here within to describe the samples fabricated using this method. More information about the dimensions of the pillar can be found in Section 7.2:.

An approach was adapted to provide the initial impetus required for stress-induced phase transformation. This included polishing the top surface using a silicon carbide polish paper (grit size - 400CW, 600CW, 1200CW and 2000CW) which leads to nucleation/formation of the monoclinic phase [81], [82]**.** This approach enabled martensitic transformation on the top surface of the pillar at low-stress levels upon compression, due to the significant generation of monoclinic phase during the polishing process.

Modified pseudo-3D printing (MP3P) pillars

In order to achieve higher loads in samples with the same composition and structure, single layer pellets were used, which avoids the stacking and void formation issues found with the P3P samples. The process used for P3P samples was improved by replacing the acetone and ethanol mixture with CZ powder to enhance the adhesion between cured layers (graphical representation in Figure 11). A pressing mould was used to assemble these stacks by alternate layers of the CZ pellet and CZ powder (shown in Figure 12**)**. Excess CZ powder filled up the gap between the mould walls and the pellets. The mould was then pressed using a hydraulic press at low stress to ensure the strengthening of the assembled pillar and promote adhesion. The pillar later undergoes a thermal treatment (Figure 14). The pillars prepared by this process (modified pseudo-3D printing, MP3P) are discussed in the context of higher stress (>100 MPa) as they were able to withstand significantly higher loads than the P3P pillars.

Powder compacted pellet (PCP)

Additionally, as-received CZ powder was used to make pellets using a powder compaction technique (i.e. powder compacted pellet, PCP) and then these samples were sintered using the same temperature profile (Figure 14) as that of the P3P pillars. This ensured similar grain growth and the morphology of the region in direct contact with the anvils during compression in P3P pillars and the PCP.

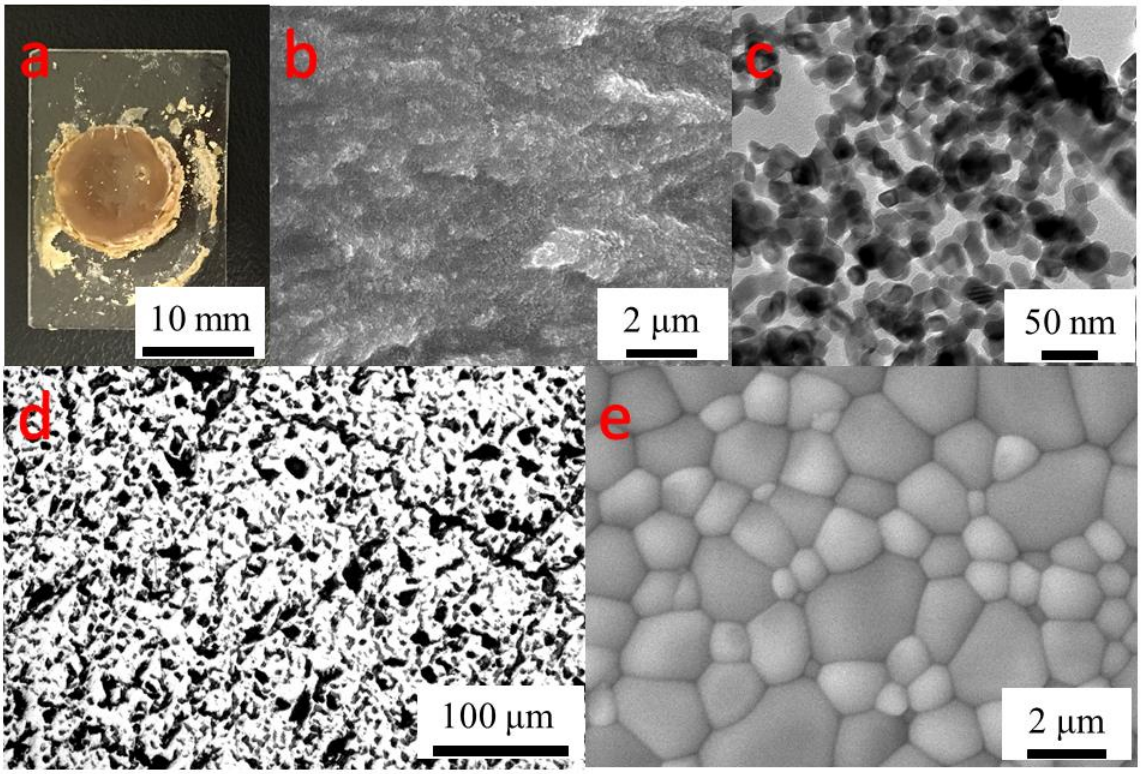

Figure 9 (a) Fabricated CZ pellet after curing, (b) SEM image showing the morphology of the cured pellet, (c) TEM image of the CZ particles, (d) optical image of the sintered CZ pellet showing the porosity and (e) SEM image showing the grain structure of the sintered pellet.

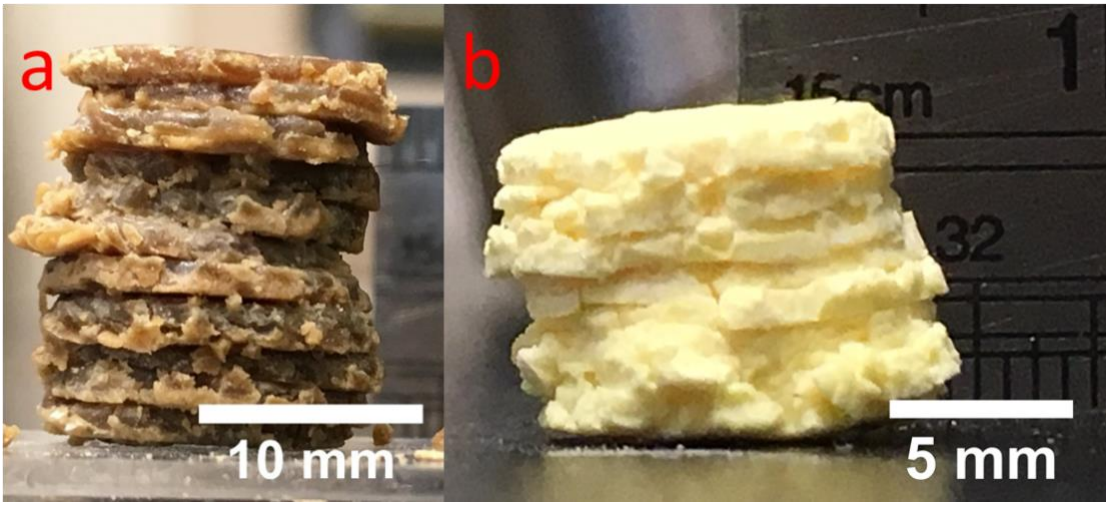

Figure 10 Pillar after stacking in (a) and after de-binding (b).

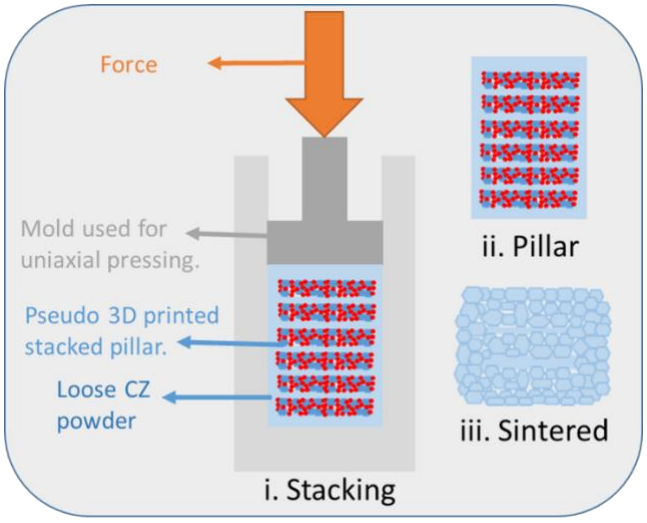

Figure 11 Modified pseudo-3D printing process includes stacking pellets with the aid of CZ powder between layers and around the stack (i), stacked pillar after pressing (ii), heat treatment two stages, debinding and sintering (iii).

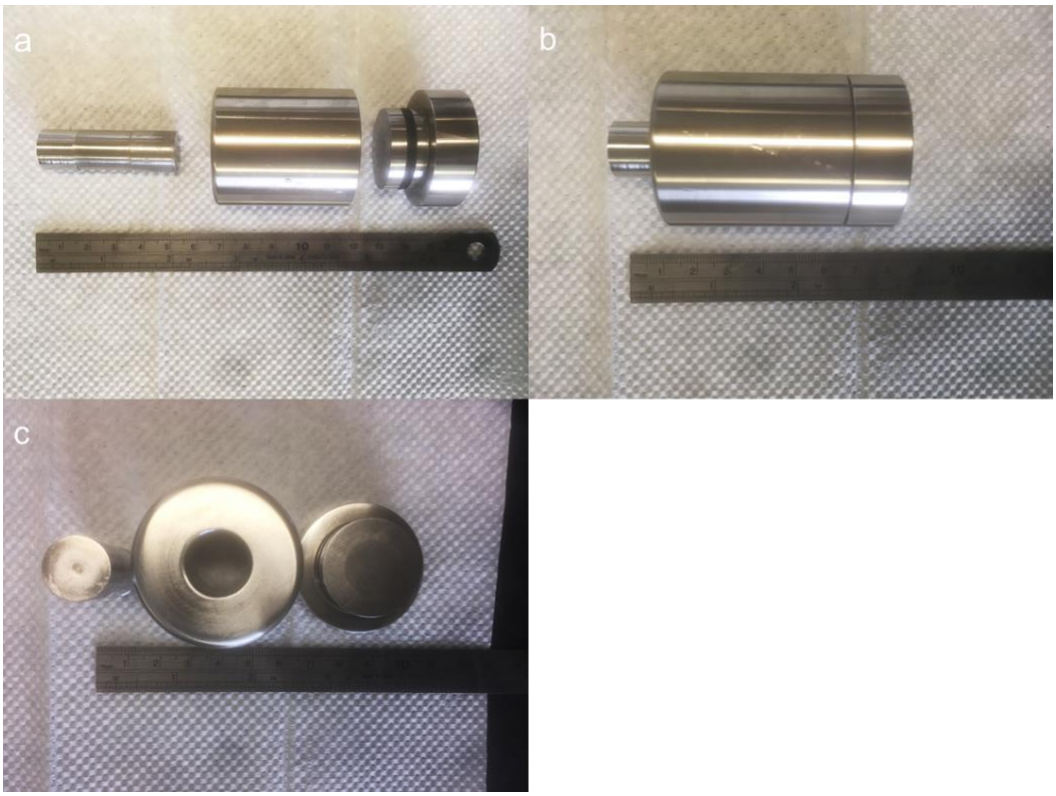

Figure 12 Stainless steel mould used in MP3P and PCP process.

Figure 13 Hand operated hydraulic pressing machine.

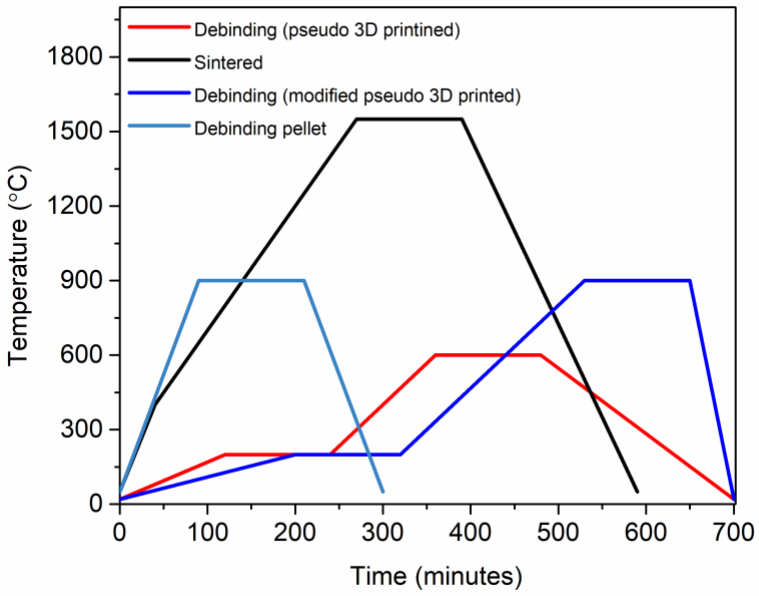

Figure 14 Heat treatment profile for both de-binding and sintering. The cooling down for both de-binding and sintering is machine-controlled.

Accordingly, the three CZ structures fabricated are summarised below:

- P3P

Pseudo-3D printed pillars (Figure 15 (1-a) and (1-b)) were made from CZ+SU-8 pellets adhered to each other using acetone and ethanol and then thermally treated in two separate processes (de-binding and sintering).

- MP3P

Modified Pseudo-3D Printed pillars (Figure 15 (2-a) and (2-b)) are fabricated by alternating CZ+SU-8 pellets and CZ powder for adhesion followed by stacking in a mould with additional CZ powder on the sides, top and bottom.

- PCP

CZ powder was compacted using a stainless-steel mould and a hydraulic press to make pellets (Figure 15 (3-a) and (3-b)) followed by thermal treatment.

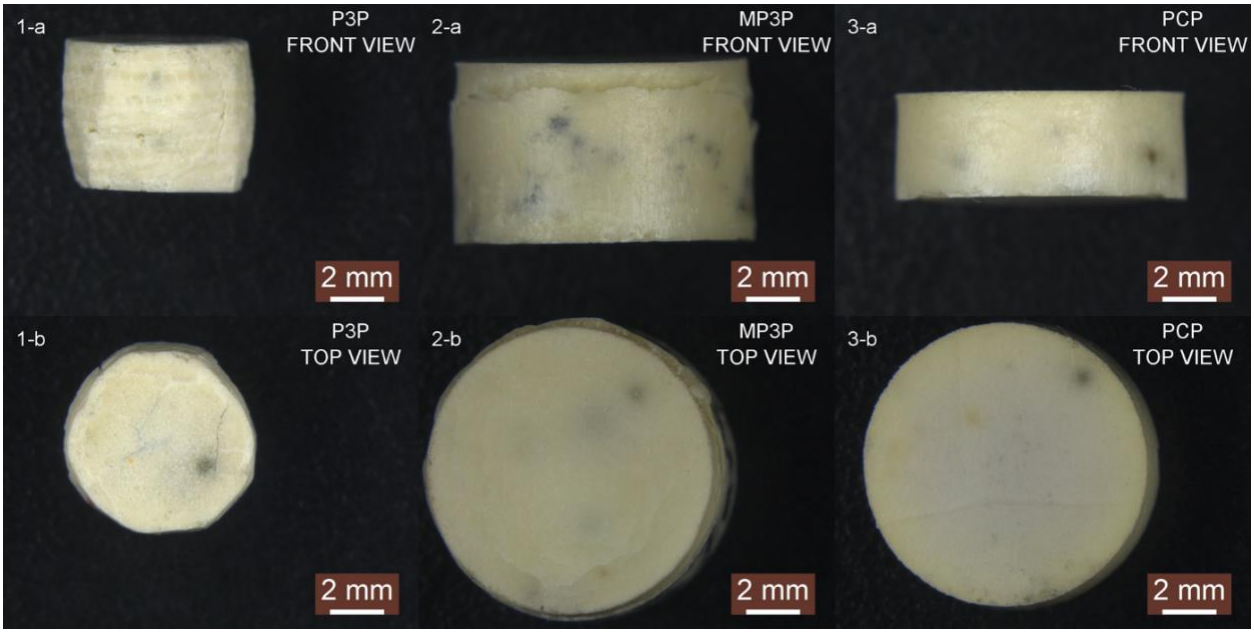

Figure 15 CZ pillars made using P3P, MP3P and PCP process.

Section 2.3: Phase analysis

XRD

Rigaku SmartLab diffractometer is used at 45 kV 200mA Cu K-alpha with a wavelength of 0.145 nm to produce the X-ray diffraction spectra using the Parallel Beam (PB) mode for bulk samples and Bragg-Brentano (BB) for powder samples.

By using the XRD spectra, the polishing and compression induced phase transformation is measured using the ratio of intensities of monoclinic and tetragonal peaks observed in the XRD patterns [83], [84].

$$x_m = \frac{I_m(111) + I_m(11\bar{1})}{I_m(111) + I_m(11\bar{1}) + I_t(111)}$$

Equation 7

Scherrer equation and W.H. plot method

X-ray diffraction was used to characterise the strain, particle size and phases in thermally treated powder and the subsequently compressed pellets. The Scherrer's equation [85] and Williamson-Hall (W.H.) [86], [87] plot methods were used to measure particle size and determine the presence of residual strain in CZ. Both methods use the full width at half maximum (FWHM, B_{total}) of the peaks and the position of the peak given by angle (θ). The FWHM of XRD peaks consists of two components, particle size and strain [88] shown in Equation 8.

$$B_{total} = B_{strain} + B_{size}$$

Equation 8

The influence of the particle size and the strain on the FWHM and further on the morphology was investigated by calculating the size and strain according to the W.H. plot method. Due to small particle size, some peaks are not clearly defined in the XRD spectra at lower thermal treatment temperatures and the tetragonal peak T (101) transforms into monoclinic peaks, so the unclear

peaks were not used for W.H. plot analysis. Rather, peaks T (110), T (202), T (004) and T (220) were analysed using their FWHM and θ positions. Particle size and strain present in the mentioned 4 tetragonal peaks for all the temperatures was measured by plotting Bcosθ as a function of sinθ. A linear regression analysis was used to measure the slope and intercept, which represented the strain component and the particle size for thermally treated powders and uniaxially pressed pellets respectively as per the W.H. plot method.

The particle size measured using the W.H. plot method showed no clear trend and at most of the thermal treatment temperatures, the size is between 0 to 100 nm. But the data processed was noisy; therefore in order to get a more accurate value of the particle size, the subsequent work was focused on T (101) which has the strongest intensity. Peak T(101) deconvolutes into two monoclinic peaks and the subsequent intensities are used to calculate the MC as per phase analysis method proposed by Garvie, et al. [83]. The particle size calculated and thereby shown in Figure 18 (a) are calculated from the T(101) XRD peaks by using the Scherrer formula [85] shown in Equation 9.

$$D_{(101)_t} = \frac{k\lambda}{Bcos\theta}$$

Equation 9

Where $D_{(101)t}$ is the particle size in nm calculated using tetragonal peak (101), *k* is 0.94, λ is 0.154 nm, B is full width at half maximum in radians and θ is taken as 30.1°, the position of the tetragonal peak (101) [89], [90] (taken in radians for particle size calculation).

Strain present in T (101) was calculated using the modified Scherrer's equation shown in Equation 10 using XRD spectra.

$$\varepsilon = \frac{Bcos\theta}{4sin\theta}$$

Equation 10

Raman spectroscopy

Raman spectroscopy technique was used to obtain Raman spectra in the regions inside the indents and around the indents. Based on the spectra, the stress-induced phase transformation was analysed in and around the indents. The indents are analysed using Witec Confocal Raman Imaging system to produce the Raman Spectra from the indents. Stress-induced phase transformation using Vickers indentation is confined to the area in and around the indent, which is quite difficult to detect using X-ray diffraction. Raman spectroscopy is therefore used to detect phase transformation in small areas. The concentration of monoclinic content from Raman spectra has been calculated using the ratio of the integral intensities [91].

$$\boldsymbol{x_m = \frac{I_m}{I_m + I_t} = \frac{I_m(171) + I_m(186)}{I_m(171) + I_m(186) + I_t(143) + I_t(257)}}$$

Equation 11

Section 2.4: Microstructure characterisation

Porosity characterisation

The UV cured pellets after sintering at 1550°C were mounted in epoxy. The samples were then polished using silicon carbide abrasive paper (grit size - 400CW, 600CW, 1200CW and 2000CW) and abrasive slurry. The polished samples were used to characterise the porous mesostructure. A pore fraction of 0.3078 for the pellets sintered at 1550°C was calculated using the method described in ASTM E 562 [54]. The pore distribution can be seen in Figure 9 (d).

Microscopy techniques

Characterisation using transmission electron microscopy (TEM)

CZ powder particles were suspended in ethanol and placed in ultrasonication chamber for 10-15 minutes. Few drops of the agitated mixture were dropped on the TEM copper grid. The powder were thermally treated at 300°C, 600°C, 900°C, 1100°C, 1300°C and 1550°C. These samples were then analysed using TEM (Jeol 1200). The images were then analysed using ImageJ software. The ratio of the axis for particles observed in TEM images determined the sphericity. Microstructural studies of ceramics refer to the ratio of major to the minor axis as aspect ratio instead of sphericity [8].

Characterisation using atomic force microscopy (AFM)

Morphological characterisation was performed using AFM (Bruker NanoScope 8). As-received CZ from the supplier was compressed followed by thermal treatment at 300°C, 600°C, 900°C, 1100°C, and 1550°C to produce relatively smooth and flat surfaces for AFM imaging. Several AFM images of 1 μm^2 and 2 μm^2 were analysed to determine the sharpness and Z range using Gwyddion Analysis software.

Characterisation using scanning electron microscopy (SEM)

SEM high resolution images were taken using Tescan VEGA 3 and Leica DM 400 optical microscope. The samples were mounted on a stub using a double sided carbon adhesive discs. In order to make the samples conductive they were sputtered with gold and a conductive silver paint was used to establish conduction between the carbon pad and the top surface of the sample.

Section 2.5: Mechanical Testing

Vickers indentation

Mitutoyo Vickers indenter with a load of 2 kilograms (4 seconds loading 15 seconds dwell time and 4 seconds unloading time) was used to make a series of indents in unpolished ceria doped zirconia pillars. Sintered pellets were mounted in epoxy and then polished as per the procedure mentioned in the surface morphology section before indentation. These pellets were then used to produce indents.

Nanoindentation

The polished samples were used for characterising the mechanical properties. Hysitron triboindenter was used for nanoindentation and constant single loading (p) was performed on the sample as a function of penetration depth (h) (Figure 16). The tip of the indenter was Berkovich and calibration was done using fused quartz. Accordingly, the hardness and the elastic modulus were measured to be 14.3 GPa and 185.56 GPa, respectively. The measured values are in good agreement with the hardness and modulus reported in the literature [92], [93].

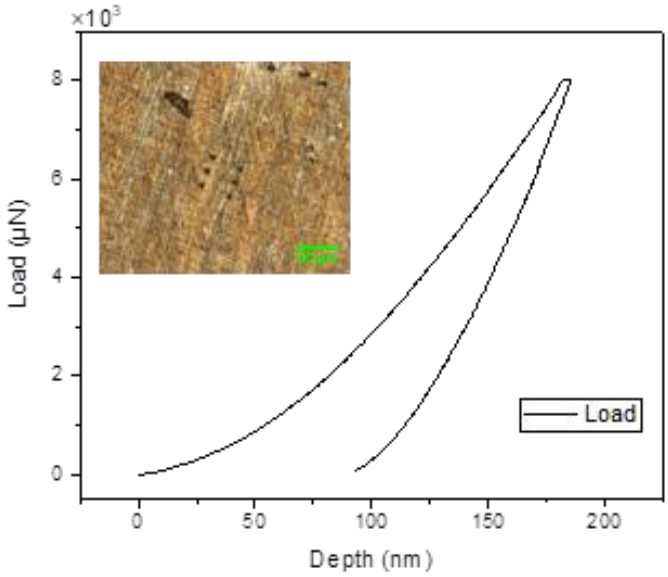

Figure 16 Load versus depth (P-H) curve obtained during nanoindentation of CZ pellet. Figure inset is an image of indents made to measure the hardness and modulus during nanoindentation.

Compression

The P3P pillars were compressed at various loads using Instron universal testing machine and accordingly, the applied stress was measured. The dimensions of the pillars and the stress measured in the pillars are provided in the appendix.

The PCP pellets were mechanically compressed using a hydraulic pressing machine, as shown in Figure 13**.** The hydraulic press uses a hand lever mechanism to compress samples held between two anvils and the load is measured by the analogue gauge mounted on the press. Based on the load measured during compression and the area of the top surface subjected to the loading, the stress sustained by the pillars was calculated and is included in the appendix.

Section 2.6: Considerations for CAD and FEA

SolidWorks 2010 was used for Computer-Aided Design (CAD) modelling and ANSYS Workbench was used for the Finite Element Analysis (FEA) simulation during the compression process. Accordingly, a CAD model with the pore size and distribution characterised from the mesostructure, as seen in Figure 9 (d) was developed using SolidWorks for the P3P samples as shown in Figure 17.

Few considerations were made in modelling porosity in the CAD model similar to that observed in the optical microscopy images of the sintered pellets. From the images, the pore size distribution, the pore fraction and general shape of the pore were also determined as mentioned above. ImageJ image processing software was used to measure the pore dimensions from the optical images. Subsequently, the details were incorporated into the CAD model with the following considerations:

1. The pores were made spherical in shape based on the general shape of a large amount of the pores as observed in the images.
2. A wide distribution was observed in the pore size in the range of 5 – 30 microns. Accordingly, pores with 10, 15 and 20 microns in diameter were incorporated in the model.
3. The distribution of the pores in the CAD model was primarily done on the following basis,
    a. The porosity fraction in the pellets and the CAD model should be the same as calculated by the method mentioned above in the surface morphology section.
    b. The pore size and the distribution should correlate with the resolution of both the modelling and the simulation software, ensuring accuracy in determining the stress level.

Based on the above considerations, several configurations of the pore distributions in the CAD model were tried that would accurately determine the stress distribution. The FEA and the associated findings are discussed in detail in Chapter 7. In the FEA and the related simulations, the force applied to the CAD model is calculated on the basis of the applied stress measured during uniaxial compression of the P3P pillars. The force used in the FEA simulations is noted in the Appendix. The CAD model and the stress distribution around the pores (post-simulation) is shown in Figure 17. Since the penetration depth of XRD is approximately 30 microns, the CAD model represents the area analysed using XRD.

The location of the applied load and the fixed support that was applied during the simulation is also shown in Figure 17 (a). The FEA simulation (Figure 17 (b)) was done to understand the stress distribution in the pillars by applying an equivalent force to the P3P pillars during the compression process. A generic material was used from the ANSYS package as the default material for the simulation and the mesh type was coarse. The Young's modulus and Poisson's ratio of this material and zirconia are similar which ensured that deformation was within the elastic regime of zirconia making it a suitable alternative for the FEA simulation, due to a lack of ceria-doped zirconia properties in the ANSYS library. Taking into consideration these constraints, the simulation was only used to analyse the stress evolution and optimisation at the pore interfaces and its further propagation into the bulk of the sample.

The von Mises stress distribution was used to analyse the stress levels developed around the pores since the material used for simulation is ductile and von Mises is used to determine the yield criterion in ductile materials. The criterion is based on the consideration that yielding begins at the point where the elastic distortion energy reaches a critical value. However, prior to reaching the yield point the material is assumed to be elastic. Ceramics exhibit elastic behaviour and upon

reaching the elastic limit undergo a brittle fracture. Therefore, it was concluded that it was appropriate to use von-Mises stress criterion to analyse the maximum stress and stress distribution around the pores.

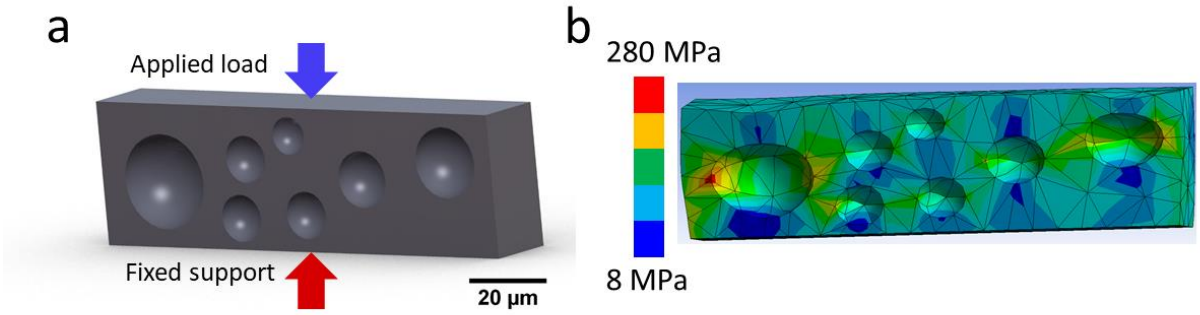

Figure 17 (a) CAD model and (b) stress distribution simulated using FEA.

Further to this, a similar CAD model was made to represent the microstructure of samples produced using MP3P samples and CAD model in the case of no pores (discussed in Chapter 5). These CAD models were then simulated using ANSYS and the stress distribution was analysed and is discussed in Chapter 5

The chapter also discusses simulation based on CAD models with varied pore shapes and distance between the pores. The propagation of the maximum stress in the bulk is analysed using those simulations. In these simulations, the constraints used are similar to the simulations used for P3P and MP3P pillars. However, due to the limitations with the resolution of the simulation software, the size of the CAD model was made bigger and in proportion, the size of the pores was increased.

Considerations used to ensure uniformity in the simulations of the CAD models,

1. The size of the CAD model was kept the same for all the different shapes used.
2. Also, the distance between the two pores was kept the same.

3. Further, the position of the two pores was also kept the same.
4. The size of the pore was also kept almost the same.

The above-mentioned considerations ensured that the porosity fraction in these CAD models irrespective of the shape of the pore was the same. The simulations and the results are discussed in Section 5.3: and Section 5.4:.

In summary, two separate methods were developed to produce structures for characterising both stress and temperature-induced phase transformation. The two methods developed can be closely associated with powder-based and slurry based additive manufacturing techniques.

The as-received CZ powder is monocrystalline, which was used to make pellets. A limited monoclinic phase can be produced by pressing the power to make pellets; thus, efforts were required to optimise the stress-induced phase transformation. The CZ powder was thermally treated at various temperatures and then pressed to make pellets. Thermal treatment would have an influence on the morphology of the CZ particles, which in turn would influence the subsequent stress-induced phase transformation. The unconstrained surfaces of CZ structures play a critical role in accommodating the displaced surfaces upon stress-induced phase transformation. Prior to additive manufacturing, such efforts had little importance; however, with the advent of this technology pre-treatment of the powder is vital.

In the case of slurry-based additive manufacturing technique, post thermal treatment, the polymer would burn off leading to the creation of pores or a network of pores. The microstructure formed after sintering is polycrystalline that by definition have constrained grain surfaces, triple junctions and grain boundaries. Such characteristics of the microstructure exhibit limitation in accommodating the strain produced during phase transformation. But the presence of pores would

ensure that the surfaces surrounding the pores have unconstrained surfaces and lesser triple junctions. The grain boundary limitations are lesser in case of porous polycrystalline structures as compared to the dense polycrystalline structure but higher than single crystals.

The characterisation of the phase transformation was done using qualitative as well as quantitative methods. Stress distribution around pores was analysed using CAD and FEA. The analysis gave a further understanding of the stress distribution in the microstructure observed in P3P or MP3P pillars when subjected to mechanical compression. Few other designs of porosity distributions in the micro/mesostructure were designed in CAD and simulated in FEA to suggest ways in optimising stress-induced phase transformation.

Chapter 3 Effect of thermal treatment on the CZ nanoparticles and its subsequent relation with MC post-stress-induced martensitic transformation.

Some parts of the work presented in this chapter has been reported in Raut et al. “Stress-induced phase transformation in shape memory ceramic nanoparticles”, J. Appl. Phys. 215109 (2019).

The chapter investigates the effect of thermal treatment on as received CZ powder particles and its subsequent relationship with the MC produced after compression of the thermally treated powder. Experimental details are included in Chapter 2.

The particle size of the ceramic powder increases with an increase in processing temperature, as shown in Figure 18 (a). The particle size of the pellets is smaller than the powder. This is possibly due to the stress applied during compaction, which leads to the breaking of the weak edges and therefore a possible variation in the size is observed.

Further characterisation of the particle size is done using TEM images and the measured sizes are shown in Figure 18 by identifying ten particles in each TEM images and several such TEM images are analysed. The area of the identified particles was measured, thereafter the particle size was derived by assuming that each particle is a sphere. The particle size calculated thereby would represent the diameter of the particle. The calculated particles size is shown in Figure 18 (a) and shows a similar trend as observed to that of particle size calculated using Scherrer’s equation for T (101). There is no significant change observed in the trend of particle size identified using the two approaches. The difference in the particle size calculated by TEM analysis and XRD is in the

most likely due to the assumption that each particle is a sphere and the limited depth of penetration of X-rays.

Strain measured using the W.H. plot method for the four tetragonal peaks is shown in Figure 18 (b). It is observed that between -200°C to 700°C, the strain in annealed powder and compressed powders is flat. The error bars are the standard deviation of FWHM values measured for T (110), T (202), T (004) and T (220) peaks at the respective temperatures for both thermally treated powders and uniaxially compressed pellet. Above 700°C, the values show a clear trend of reducing strain as the temperature increases. This is likely due to the onset of surface diffusion and mobility in the powder, which leads to release of strain as the particle size increases. The breaking of the weak edges during pressing would release strain from the particles due to an invariable change in residual stress in the four tetragonal peaks.

To further measure the strain present in T (101) the modified Scherrer's equation was used and is shown in Figure 18 (c). The strain calculated in T (101) using Scherrer's equation shows no change in strain between -200°C to 700°C.

Above 700°C, the strain appears to reduce in thermally treated powder. A similar influence of temperature on strain is observed in the analysis using W.H. plot method Figure 18 (b). The compressed samples witness a higher strain which could be due to the compressive forces generated during pressing.

The W.H. plot method shows that the strain in the compressed pellet is lower than thermally treated powder whereas Scherrer's equation shows that the strain is higher in the compressed pellet. Though the change in residual stress would reduce the overall strain represented by the four

tetragonal peaks in compressed pellet but the amount of strain in T (101) lattices would be higher due to the compression and subsequent doconvolution in the two monoclinic peaks.

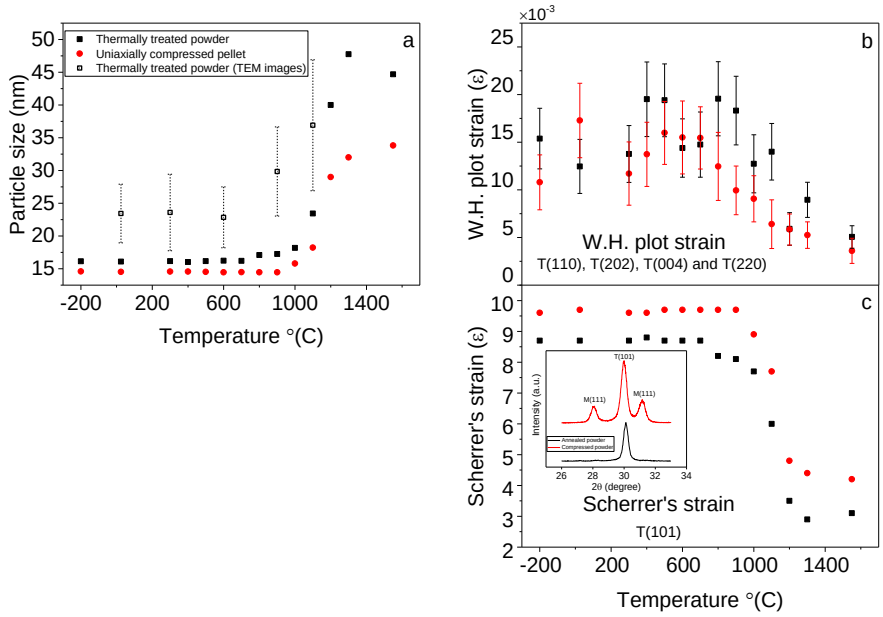

Figure 18 Particle size calculated using Scherrer's equation by using T (101) peak and from TEM images (a), strain calculated using the W.H. plot method (b), strain calculated using modified Scherrer's equation (c). Graph inset graph (c) shows XRD patterns of CZ processed at 1100°C with the tetragonal and monoclinic peaks used to measure the monoclinic content.

Residual stress was calculated based on the strain calculated in tetragonal peak T (101). Using stereographic projections showed in Figure 19 the position for T (101) was located. Based on the stereographic projections in Figure 20 the theoretical elastic modulus value of tetragonal zirconia in T (101) orientation was determined and accordingly residual stress was calculated based on the Equation 12

$$Residual\ stress\ (\sigma) = Modulus\ of\ Elasticity\ (E) \times Strain\ (\varepsilon)$$

Equation 12

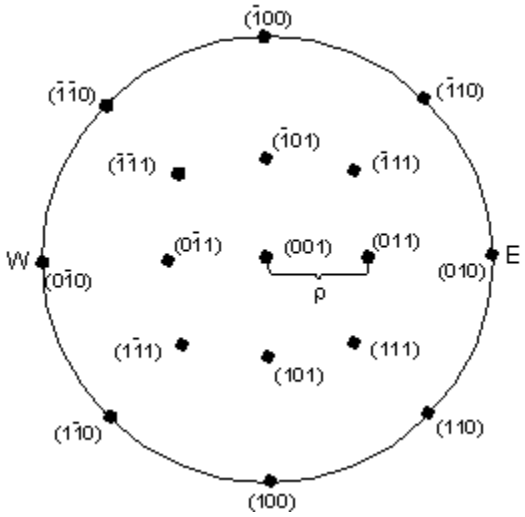

Figure 19 Stereographic projection of isometric crystal. Image taken from reference [94].

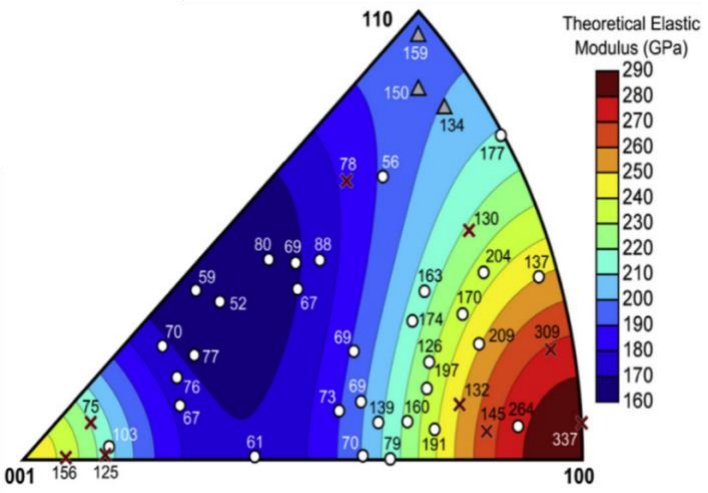

Figure 20 Stereographic projection of tetragonal zirconia. Image taken from reference [19].

The theoretical modulus for tetragonal zirconia as observed in Figure 20 based on the stereographic projection from Figure 19 is 175 GPa and the strain was taken from the Scherrer's equation as shown in Figure 18 (c). Accordingly, as per Equation 12 the residual stress was calculated for the samples thermally treated and then subsequently compressed to make pellets Figure 21.

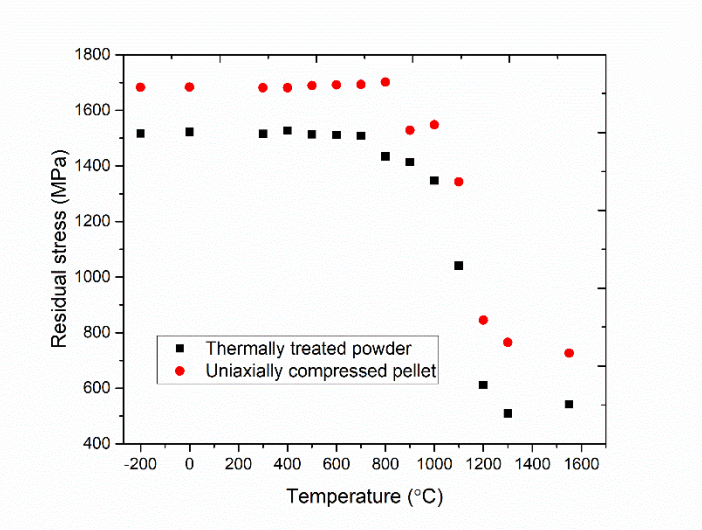

Figure 21 Residual stress calculated in thermally treated and uniaxially compressed powder.

The residual stress is observed to reduce as a function of the treatment temperature in both powder and pellet. The trend is similar to the trend observed for strain calculated using Scherrer's equation in Figure 18. The residual stresses calculated by this method are higher by a magnitude. The residual stresses are calculated by based on the Scherrer equation in the tetragonal phase. These stresses are microscopic stresses that are quite likely developed in the particles. On this note, it can be said that the applied stress of 250 MPa applied while making pellets is quite misleading and the actual stresses developed at the granular levels are optimised and higher by a magnitude.

Section 3.1: Characterising particle size and shape evolution

AFM was used to characterise the aggregate changes in the morphology of the pellet. The pellets are made by compressing refined CZ powder followed by thermal treatment at 300°C, 600°C, 900°C, 1100°C and 1550°C. A general sense of the changing morphology and the density of stress concentrators is evident in AFM images shown in Figure 22. At 300°C, the height variation is limited, and the unevenness is due to the inherent size variation as received from the supplier. At 900°C, the height variation increases as seen in Figure 22. (b) whereas the particle size also increases as observed from the XRD data in Figure 22. (a). At 1550°C, the particle surface is smooth and there is no height variation or stress concentrators as seen in Figure 22. (f).

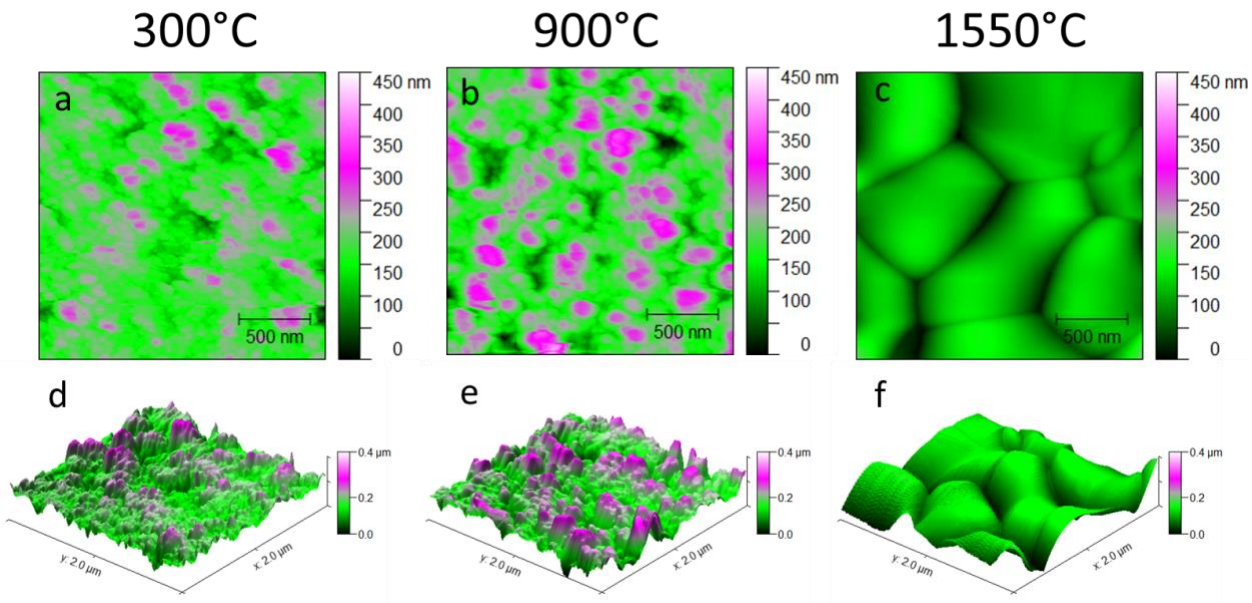

Figure 22 (a) 300°C, (b) 900°C and (c) 1550°C are AFM images used to analyse the morphological evolution in CZ as a function of temperature and (d), (e) and (f) are 3D images from the AFM data that show increase in roughness at 900°C and smooth curvature at 1550°C.

The morphology of the CZ ceramic particles was also characterised using TEM. The refined CZ powder particles closely resemble a sphere of around 20 nm in diameter and is seen in Figure 23 (a). The CZ particles observed in Figure 23 (b) and (c) are thermally treated at 300°C and 600°C but do not reveal any significant changes in the morphology. The changes in the morphology reveal the formation of a straight edges in the form of facets in CZ particles and can be seen in Figure 23 (d). It can be observed in the TEM images Figure 23 (d) that at 900°C, the particle size increases. Figure 23 (e) particles are thermally treated at 1100°C and most of them show straight edges and facets. Subsequent heating increases the particle size and it appears that at several particle to particle interfaces the material will fuse to form a neck like structure, attributed as “necking” and subsequently formation of large particles or grains, evolution of which is seen in Figure 23 (f) and (g) i.e. 1300°C and 1550°C. Figure 23 (h) is a high-resolution image of a CZ particle and the single spots using Fast Fourier Transform (FFT) in figure inset Figure 23 (h) aided in characterising the as-received powders as monocrystalline. The particle size measured from the TEM images is shown in Figure 18 (a).

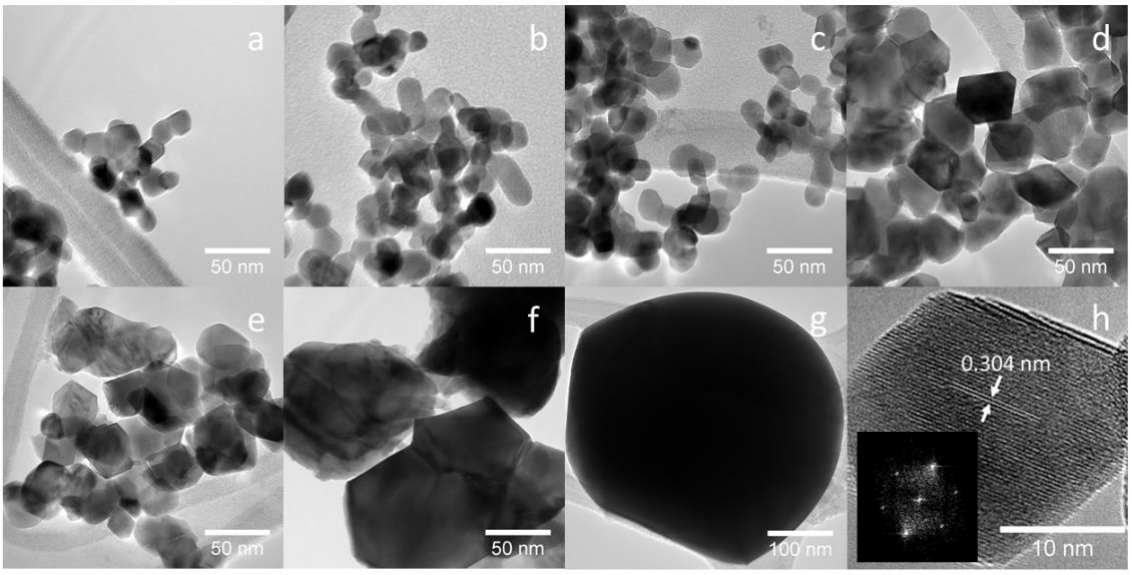

Figure 23 CZ powder thermally treated at (a) no thermal treatment, (b) 300°C, (c) 600°C, (d) 900°C, (e) 1100°C, (f) 1300°C and (g) 1550°C. HRTEM image and its FFT (inset) from a single CZ particle shown in (h) [95].

Section 3.2: Monoclinic content in CZ pellets

Using equation Equation 7, the MC for both the annealed powder and the compressed pellet was calculated using the intensities of the tetragonal and monoclinic peaks.

Due to the thermal-induced phase transformation, the residual levels of the monoclinic phase in the CZ powder were transformed to the tetragonal phase and is seen in Figure 24.

Taking into considerations the limited amount of the monoclinic phase, it was assumed that on the application of stress the subsequent MC produced due to the stress-induced phase transformation would also be limited. Contrary to this assumption, an opposite trend is observed between the thermally treated powder and compressed pellet. "Regime I", highlighted in Figure 24 shows an incremental change in MC in pellets as a function of temperature used to treat the CZ powder. A noticeable increase in MC is observed after 700°C and is highlighted in Figure 24.

The findings of Regime I can be explained in the context of the findings reported by Chiu [29] (reported by Becher et al. [12]) and by Garvie et al. [96]. The findings of Becher et al. [12] show a relation between the grain size and the amount of MC produced after thermal-induced phase transformation in the case of sintered CZ mechanically compressed pellets. The relation is linear, i.e. as the grain size increased, the amount of MC that was calculated was also observed to increase. The transformation was induced using an thermodynamic driving force (immersion in liquid nitrogen). The increase in the MC was observed due to the tensile forces produced as a result of thermal expansion anisotropy and the strain mismatch at the grain corners leading to optimised thermodynamic driving force for transformation in grains with larger size as compared to the grains with smaller sizes. The findings can appropriately be explained in the hypothesis proposed by the authors for sintered polycrystalline with constrained grains due to which the effect of grain size and geometric stress concentration on the MC produced is not investigated separately.

Similar to the findings cited above from the literature, the increase in the MC can be related to the increase in the grain size, as observed in Figure 23 and Figure 24. However, the limited increase in the grain size observed between 0°C to 900°C and the increase in MC in the same regime irrespective of it suggests the contribution of particle shape which should be acknowledged.

The MC at 1200°C and 1300°C is observed to reduce and it increases again at 1550°C. The regions above 1100°C is shown as “Regime II” in Figure 24. This phenomenon was explained as particles, or a group of particles (agglomerations) would form neck like structures between each other at the point of contact. The growth mechanism for the bridge-like structures between the agglomerations can be understood in the context of thermodynamics that govern the energy-driven mass transport i.e. necking and sintering.

Taking into consideration that load applied was constant to make the pellets from pre-treated CZ powder, the drop in MC can be explained in the context of the load being distributed over an increased area. Boutz et al. observed in thermal treatment of zirconia that below 1000°C, the growth of the grain is slow and above this temperature, it grows rapidly [90]. Comprehending the findings of Boutz et al. in the context of this study, it would be logical to interpret that the quick growth be delayed in this case taking into consideration the shorter dwell time (1 hours) and longer (2 – 15 hours) in the case of Boutz et al. Post stress-induced phase transformation the MC formed is quite likely to stay contained inside the particle as observed by Chen et al.[97], [98].

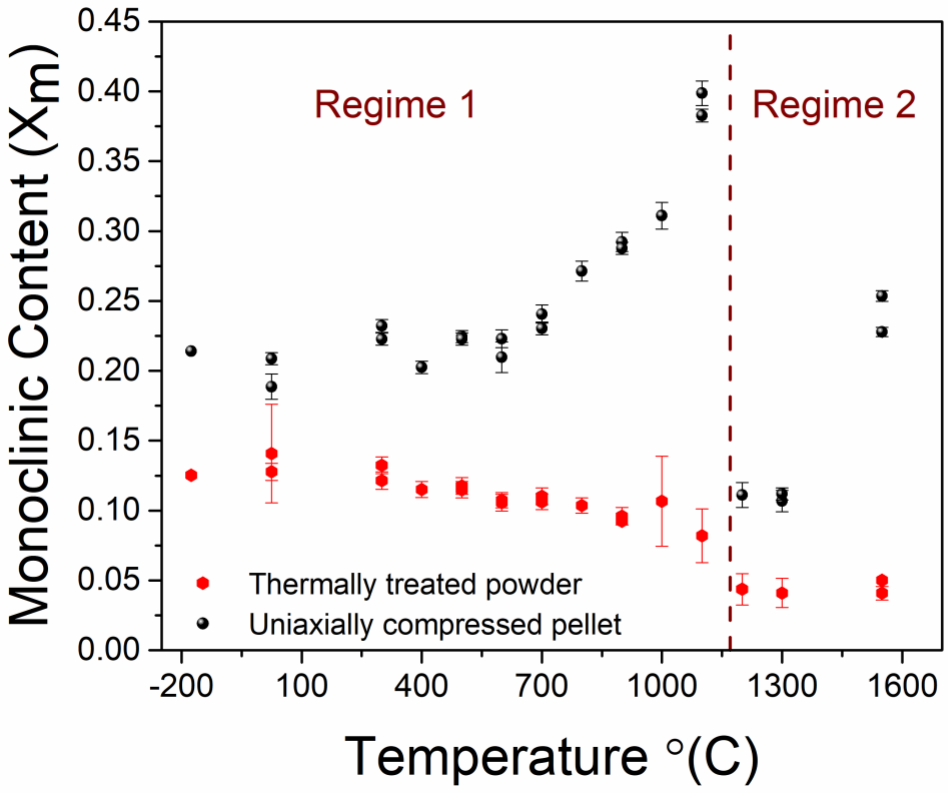

Figure 24 The phase analysis equation was used to calculate the MC in both thermally treated powder and subsequently compressed pellets and is shown as a function of temperature. The error bars represent the absolute error calculated from the relative error as per the error propagation

method. An example of the calculation of error bars is shown in the appendix. Regime I and II have been separately shown comprising of (quasi-spherical edges + straight-faceted edges) and sintering + particle growth) geometry in the particle shape [95].

Section 3.3: Effect of liquid nitrogen on MC

To investigate thermal-induced phase transformation using liquid nitrogen immersion technique as received CZ powder was immersed in LN_2. CZ powder thermally treated at liquid nitrogen temperature showed a very small change in the MC. Subsequently, in situ, XRD was employed to observe the change in the phases if any and validate the previous findings of the as-received CZ powder and the XRD spectra is shown in Figure 25. Becher et al.[12] observed grain-sized dependence on martensitic start temperature using liquid nitrogen in CZ. But the CZ used in this work is nano-sized and for sub-micron sized grain of ZrO_2 (2% (mole) Y_2O_3) Becher et al. didn't observe any transformation both for liquid nitrogen and helium. Correspondingly, the XRD spectra at -100°C and -150°C for CZ powder failed to show an increase in the monoclinic peaks that are used to calculate the MC as shown in Figure 25. This finding can be explained in the observations reported by Heuer et al.[99] for PSZ, *t*-ZrO_2 precipitates that had a diameter of 40 nm are observed to be coherent and very resistant to transformation, based on which it can said that to nucleate the monoclinic phase in the CZ powder, temperature below -267.15 °C would be required.

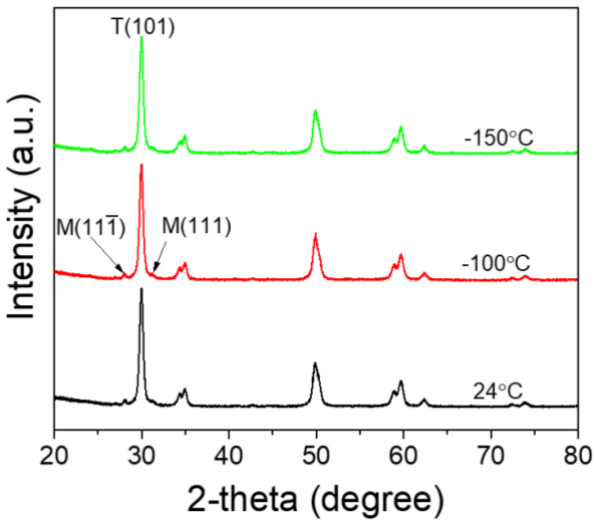

Figure 25 Diffraction pattern of as received CZ powder obtained using in-situ XRD at room temperature, -100°C and -150°C [95].

Section 3.4: Surface morphology characterisation

The change in the morphology at the microscale was characterised by measuring the Z range, inclination angle and radius of curvature of the stress concentrators from the AFM images. The samples used for AFM are made using technique explained in Section 2.1:.

Variation in height of features shown as Z range in Figure 26 (a) was measured from the captured AFM images. At lower temperatures of 300°C and 600°C, the Z range average is similar, but the variation reduces at 600°C. The variation in Z height at 300°C is due to inherent size variation as received from the supplier which can be established by the lack of growth of particle size as observed in Figure 22 (a). As observed in Figure 22 (a) at 900°C and 1100°C the particle size starts to increase and the variation in the height implies alterations in morphology due to heat treatment as can be seen in Figure 26 (a).

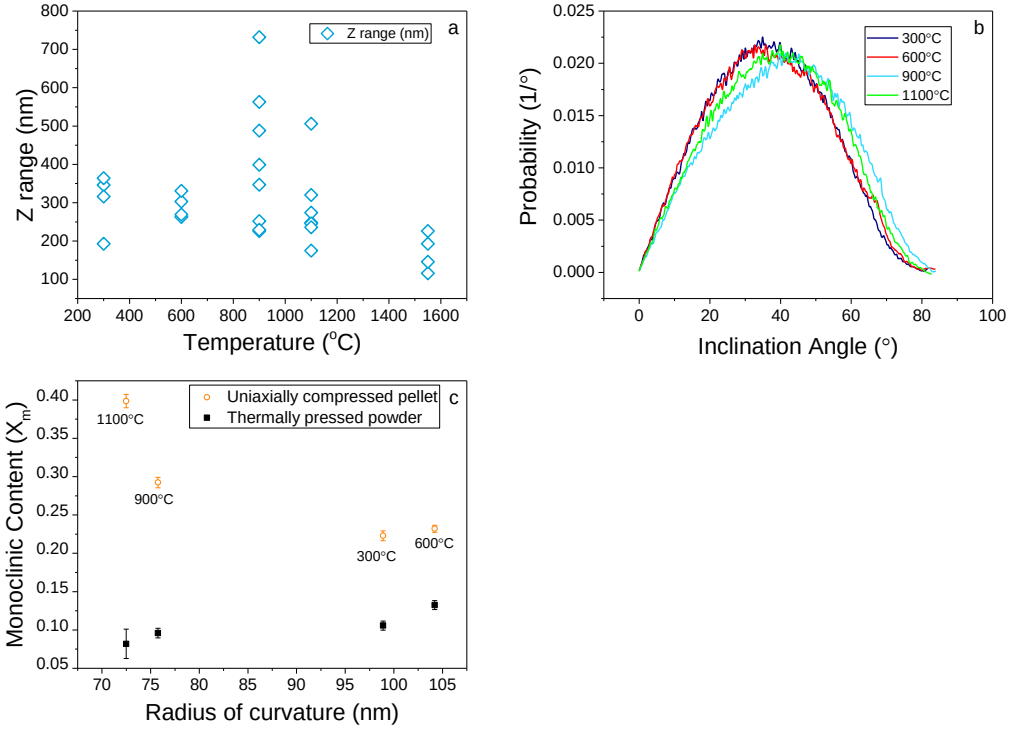

Figure 26 (a) shows the variation in height of the grains observed using AFM in annealed pellets (b) inclination angle of the steep features observed in samples used for AFM and (c) the change in monoclinic content as a function of the radius of curvature of steep features observed in the AFM.

The inclination angle is the steepness of the sharp features measured from AFM images. Several AFM images were used to measure the inclination angle of the features and the average of multiples peaks for each temperature is shown in Figure 26 (b).

A similar approach to characterise the inclination angle [100] has been employed by Hang et al. [101]. The inclination angle is the angle of the sharp features which would act as stress concentrators as per the hypothesis. Consequently, an increase in inclination angle implies an increasing sharpness of the features. In Figure 26 (b) it is observed that the curves for 300°C and

600°C overlap implying no change in the inclination angle. The curves for 900°C and 1100°C shift towards higher inclination angle. Averaged curves for the four temperatures show an overall rightward shift implying that the features get steeper as a function of temperature.

The radius of curvature of the features was measured to further understand the changing morphology as a function of temperature. The width of features from the cross-sectional view of the AFM images at each temperature was used to measure the radius and an average was calculated. Several such measurements were made to determine the trend. The MC calculated in uniaxially compressed pellets observed in Figure 24 for 300°C, 600°C, 900°C and 1100°C as a function of the radius of curvature is shown in Figure 26 (c).

A small change in MC is observed for samples at 300°C and 600°C though the radius appears to reduce. At 900°C, the radius is reduced, but the MC shows an increase. Similar is the case for 1100°C wherein the radius reduced further, but the MC is higher than 900°C.

In regime 1, as the processing temperature goes higher the morphology changes in terms of reduction in radius and higher inclination angle. These two conclusions support the argument of increasing sharpness of the features as a function of temperature. The density of such features is also observed to increase at 900°C as observed in AFM images in Figure 22 (b and e) and Z range variation in Figure 26 (a). The temperatures at which these features get sharper shows a higher MC yield and that shows strong evidence to prove the hypothesis at the microscale.

Though AFM data show at the microscale the contribution of stress concentrators, the particle size calculated from Scherrer's equation is much smaller. It is quite unclear about the effect of temperature on the shape and size of the particles at the nanoscale.

The change in morphology of the particle is evident as a function of temperature and it is comprehended in the context of its sphericity, number of straight edges and facet length from the TEM images. The shape changes mentioned in the caption of Figure 24 and seen in TEM images in Figure 23 were used to measure the sphericity. The sphericity of a sphere is 1 whereas in the case of a cube is 0.87, i.e. measured using the ratio of surface area of a sphere having the same volume as a particle to surface area of the particle [69], [95]. Alternatively, the sphericity measured using the ratio of minor to major axis in the case of sphere as well as a cube, based on the 2D images which would represent a circle and a square would be 1. In the case of similar sphericity for a sphere measured with the two methods but with smooth surfaces, under uniaxial compression the surface would show minimal stress concentration. Contrary to this, a straight faceted edge of a cube would produce multiple sites of reduced area and experience stress concentration upon uniaxial compression [64]. Sphericity can be quantified using two separate approaches therefore it is necessary to explain the faceting in particles and establish a relationship with the effect of stress concentration on MC. The sphericity shown in Figure 27 is the ratio between major and minor axis superimposed on the 2D TEM images [95].

It is evident from the TEM images that thermal treatment would change the morphology of the particles, increase faceting, but in the absence of the particle size growth, the aspect ratio would stay the same. Further thermal treatment would increase the size along with the faceting of particles becoming more pronounced and fusion of neighbouring particles would reduce the sphericity. Also, based on the observations in Figure 18 (a) and Figure 23, increase in particle size due to possible solid-state particle fusion is already established. From the several measurements taken to identify the sphericity, the ratio, as shown in Figure 27, is observed to reduce as the thermal processing temperature increases. Also, it is observed that with the decrease in sphericity the MC increase.

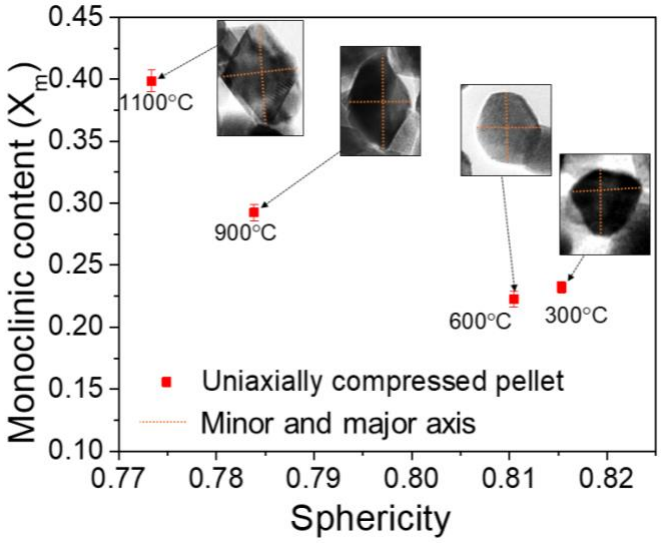

Figure 27 The change in monoclinic content as a function of sphericity. Dotted lines on TEM images inset figure depict major and minor axis used to calculate the sphericity [95].

The process of faceting was described by Heffelfinger et al. [102] as decomposition of an existing surface between two or more surfaces. The incremental heat treatment used on the CZ material in this study suggests the phenomenon of faceting can be well explained in the context of thermodynamics. In the event of thermodynamically unstable surfaces, Herring observed besides the equilibrium crystal surface (ECS), faceting will evolve into hill and valley structures due to decomposition [102], [103]. Mullins explained the growth of facets that depends upon the power law based on the mass transport mechanism [104]. Further to faceting, according to Heffelfinger, growth leads to coarsening and this is propelled by the driving force to increase the width of the facet with time is surface energy [102].

In order to make the argument of stress concentration from edges and facets more concrete, instances of the occurrence of these entities were counted. Sharp or straight edges were counted like observed at 900°C - Figure 23 (d), part of which is shown in Figure 28 (a) as opposed to 300°C - Figure 23 (b) shown in Figure 28 (a). Multiple TEM images were analysed to identify such

occurrences and an average is observed to increase as a function of temperature seen in Figure 28 (a).

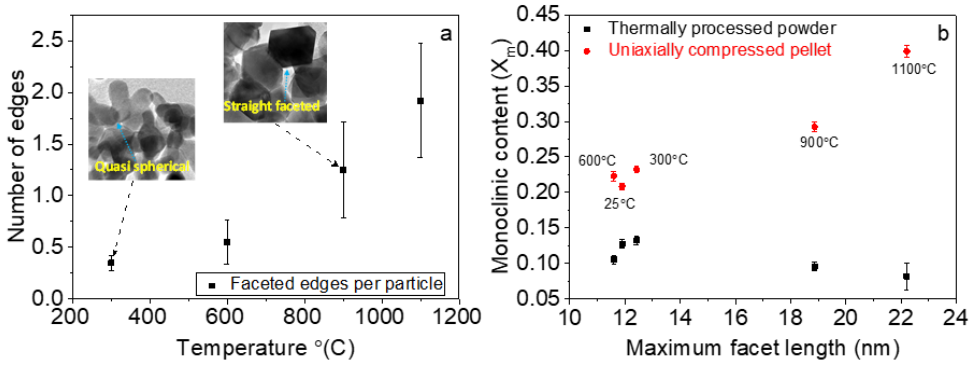

Figure 28 The number of edges with straight facets per particle increases as a function of temperature in (a) and measurements taken from particles observed in TEM images show an increasing trend in monoclinic content as a function of maximum facet length in (b). Images inset in (a) are from Figure 1 and show the change in faceting at lower and higher temperatures [95].

The length of each facet was also measured for several particles and is compared with the monoclinic content in Figure 28 (b). Similar to the number of edges, the facet length is observed to increase as a function of temperature. Increasing length of the particles indicate growth of sharp edges at the nanoscale and they would act as stress concentrators on the application of stress. Increase in the length of sharp edges of the particles would increase the intensity of the stress concentration due to the gradual evolution from curved smooth surfaces to sharp faceted edges. This intensity would further increase with the increase in the length as a function of thermal treatment temperature.

With the systematic thermal treatment in regime I it was observed that the CZ particle surface can be manipulated. This manipulated surface can thereafter play a crucial role to optimise mechanical properties or stress-induced phase transformation in the case of this study.

Section 3.5: Thermal-induced reverse phase transformation.

This chapter is focused on thermally treating the compressed pellets from Chapter 3 and analysing the total tetragonal phase recovered. The pellets were thermally treated at different temperatures and the dwell time at these peak temperature were varied as well.

The pellets made using CZ powder thermally treated at 1000°C and 1100°C, were subjected to thermal treatment at different temperatures and for different dwell times at peak temperature, as shown in Figure 29. 1000°C and 1100°C were chosen as pre-treatment temperatures since they showed the highest MC upon compression as observed in Figure 24. XRD spectra was obtained from the pellets after compression and after thermal treatment. Compression increased the MC in the pellets due to stress-induced phase transformation. A systematic effort was made to reduce the MC using thermal treatment leading to tetragonal phase recovery.

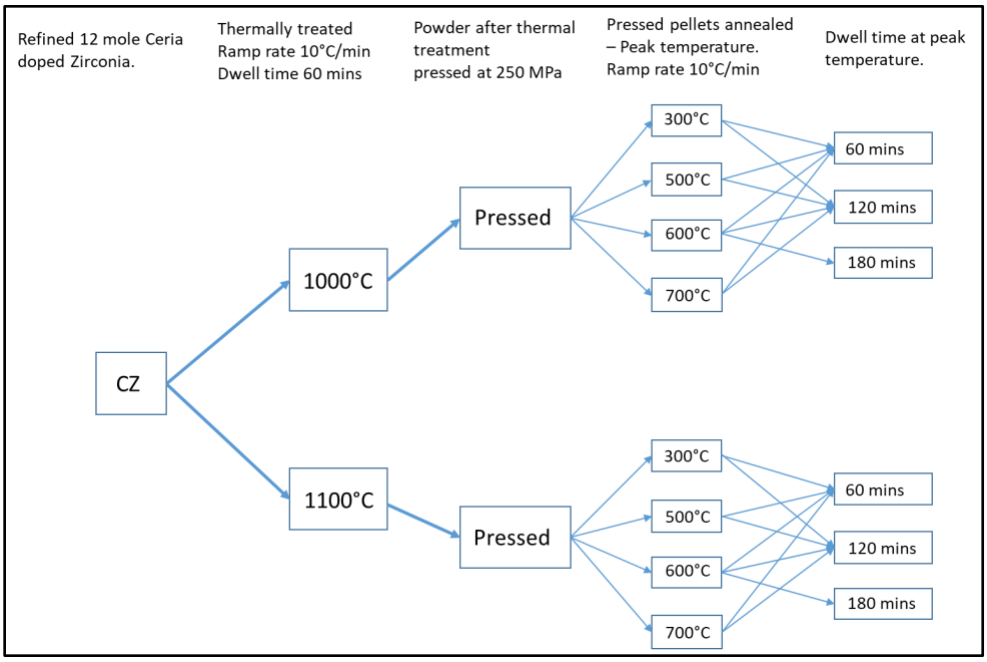

Figure 29 Thermal treatment temperature and time of CZ pellets made using thermally treated powder at 1000°C and 1100°C.

MC was calculated using Equation 7. All the pellets were made using the same batch of CZ powder post thermal treatment which ensured similar levels of the monoclinic phase (MC for reference can be taken from Figure 24) before pressing the powder into the pellets. As observed in the Figure 30, MC in the pellets after pressing is ~0.3 (all solid markers), which shows that the stress-induced phase transformation has been uniform. Pellets thermally treated at 300°C shows a very small reduction in MC. As the temperature increases the MC is observed to reduce. The maximum tetragonal phase recovery is observed to be at 700°C.

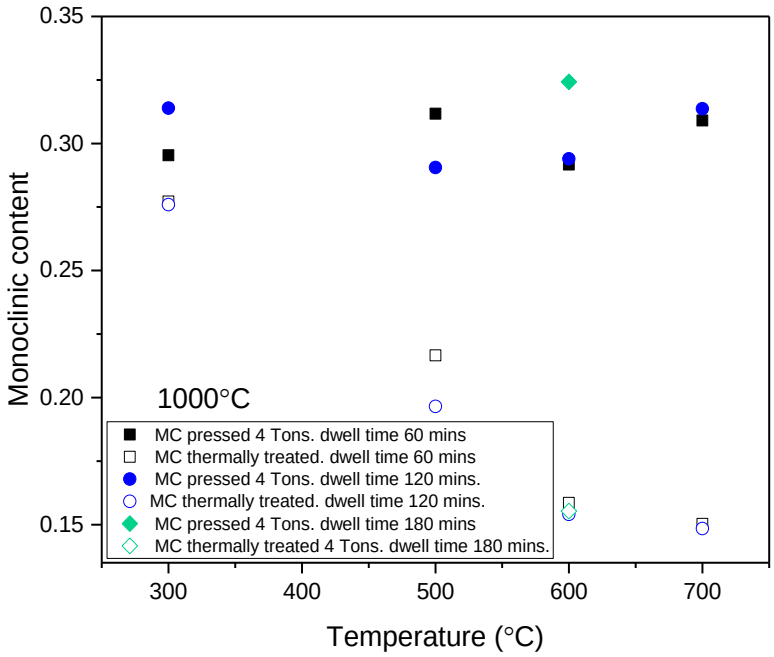

Figure 30 MC calculated in pellets made using CZ thermally treated at 1000°C after compression and after thermal treatment. Solid markers show MC after pressing and hollow markers with the corresponding shape show MC post thermal treatment.

To further understand the change in MC, difference in MC in pellets between the compression and thermal treatment as a function of thermal treatment temperature is shown in Figure 31. A linear increase is observed in the difference in MC. A higher difference is observed in the pellets thermally treated for 120 minutes as compared to 60 minutes at 300°C. As the thermal treatment temperature increases the difference between the two dwell times do not show much difference. But more tetragonal phase recovery is observed with 180 minutes dwell time at 600°C. From the observations, it is quite evident that the tetragonal phase recovery is the highest at 700°C though it gradually increases right from 300°C. Also, the temperature is observed to be crucial in phase recovery as opposed to the amount of time for which the sample is held at the temperature.

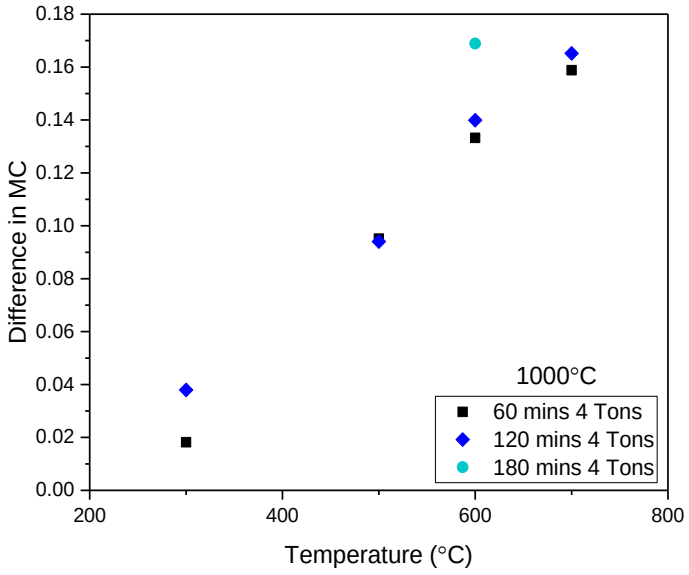

Figure 31 Difference between MC after compression and after thermal treatment in pellets made using CZ powder thermally treated at 1000°C.

CZ thermally treated at 1100°C was used to make pellets with two separates loads, 4 tons (250 MPa) and 5 tons (approximately 312.5 MPa). 5 tons load produced a higher amount of monoclinic content. The average MC yield in pellets pressed using 4 tons of load is 0.34 and with 5 tons is 0.37 as observed in Figure 32. At 300°C, the drop appears to be gradual and it keeps increasing as the thermal treatment temperature increases. The difference between the MC recovered from the 5 and 4 tons batch appears to be reducing and converges at 700°C.

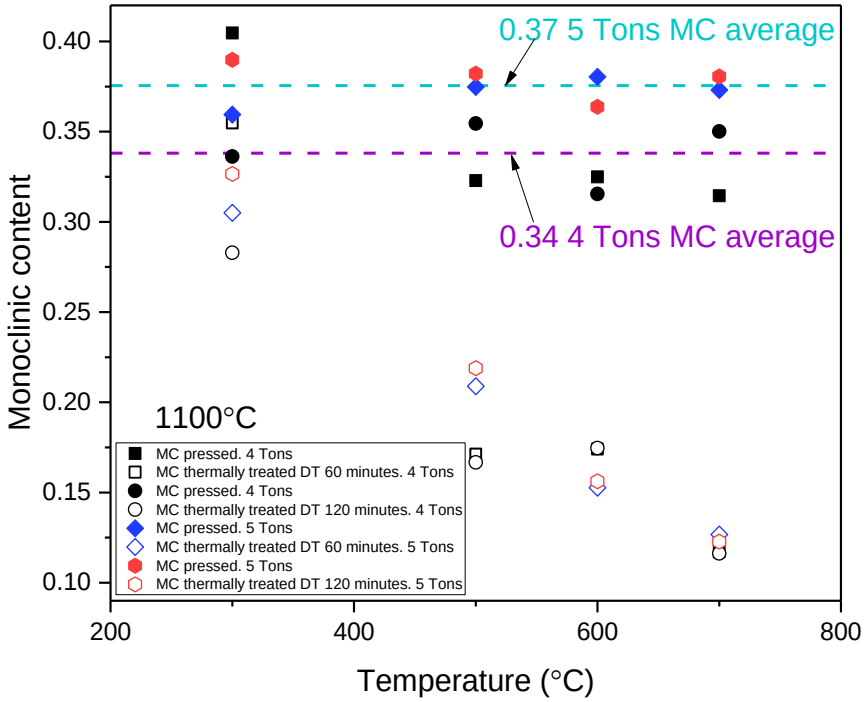

Figure 32 MC calculated in pellets made using CZ thermally treated at 1100°C after compression at 4 tons (250 MPa) and 5 tons and after thermal treatment. Solid markers show MC after pressing and hollow markers with the corresponding shape show MC post thermal treatment. Dwell time (DT).

The difference in the MC after and before thermal treatment is calculated and shown in Figure 33. The difference increases as a function of thermal treatment temperature. The maximum amount of tetragonal phase recovery is observed at 700°C. The difference in MC for pellets pressed at 5 tons is higher because of the higher MC at the start. Despite the tetragonal phase recovery to be the maximum as observed in Figure 33 yet the MC levels reached appear to converge in Figure 32 at 700°C.

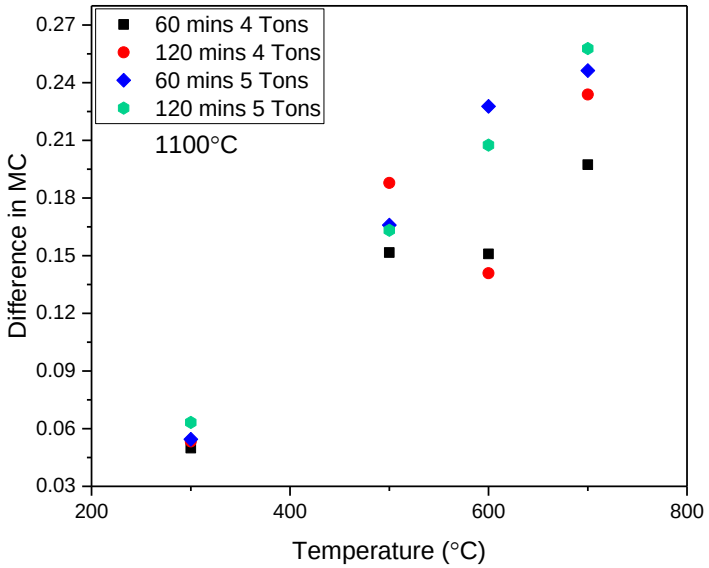

Figure 33 Difference between MC after compression at 4 tons (250 MPa) and 5 tons and after thermal treatment in pellets made using CZ powder thermally treated at 1000°C.

This suggests that the highest tetragonal phase recovery can happen at 700°C irrespective of the starting MC. It is not ideal to thermally treat the pellets in granular packing above 700°C since in the previous study [95] it is observed that above 700°C the particle size increases. The findings suggest that with relatively higher MC at the start, 500°C may not be the most optimised temperature to recover the tetragonal phase. Thermally treating the pellets at 700°C would possibly aid in recovering the highest tetragonal phase due to thermal-induced phase transformation.

Further to this, preliminary evidence suggests both, higher temperature would aid in maximising recovery of the tetragonal phase and in the case of increasing the dwell time at peak temperature optimised recovery of the tetragonal phase can also occur. As mentioned before, the interface between the tetragonal phase and the monoclinic phase is a glissile surface and would require a finite amount of chemical force to initiate the reverse phase transformation. It is evident that at

300°C, the force (chemical) threshold to initiate the reverse phase transformation is surpassed. With the increase in peak temperature the tetragonal phase recovered or the difference in MC increases as well higher. However, it is also sensible to argue that maintaining a certain force (peak temperature) for a longer duration (dwell time) would lead to higher reverse phase transformation. Since if this force has lowered the chemical free energy to rearrange the deformed crystal structure back to the tetragonal phase it should be able to achieved a higher magnitude of rearrangement. In the findings it is evident that with higher temperature optimised tetragonal phase recovery is possible but to find the relation between each peak temperature and dwell time with the tetragonal phase recovered would require further investigation.

Chapter 4 Characterisation of stress-induced phase transformation in pseudo-3D printed CZ structures.

In this chapter, the effect of polishing and Vickers indentation techniques in producing stress-induced phase transformation in P3P pillars was investigated. Abrasive polishing is used as an auxiliary process to generate the initial monoclinic phase. The polishing or abrasive grinding is done using a silicon carbide paper. The process of abrasive polishing involves polishing the ceramic structure against the silicon carbide paper in a pattern that depicts the figure 8 with a steady stream of water directed towards the polishing zone. The flow of water ensured that the chipped ceramic pieces were washed away from the interface between the ceramic body and the silicon carbide paper. Also, in the case of abrasive polishing, a heat-affected zone is created at interface between the grinding stone or paper and the specimen. Taking into consideration the thermal-induced reverse phase transformation that is observed in CZ, it is possible that the forward stress-induced phase transformation occurred during polishing would be reversed back. Such findings were reported by Swain et al. [81]. So, in the case of maintaining a steady stream of water the temperature would be lower than the austenite start temperature. Due to the human effort involved in pressing the sample, very little control can be achieved in maintaining a uniform magnitude of force during polishing. The Vickers indentation technique applied load to a localised area in a controlled manner, which resulted in stress-induced phase transformation in and around the area of applied stress i.e. the indent. XRD and Raman spectroscopy techniques were used to characterise the phases in the samples. With these approaches, preliminary evidence was gathered

on producing stress-induced phase transformation in a large and localised area using polishing and with indentation techniques respectively.

The pillars and pellets made using the pseudo-3D printing or P3P process mentioned in Chapter 2 were used for this investigation. Additionally, the pellets were mounted in epoxy for Vickers indentation followed by Raman spectroscopy.

Section 4.1: Stress-induced phase transformation (Abrasive polishing)

In the case of the polycrystalline shape memory ceramics, the critical stress required to nucleate the monoclinic phase is often above 1 GPa [14]. However, the stress required to grow an existing monoclinic phase is considerably lower.

Phase analysis using XRD

For reference, in Figure 34, XRD patterns for pure ZrO_2 and as received CZ are shown. Zirconia occurs in the monoclinic phase and CZ in the tetragonal phase with traces of the monoclinic phase at room temperature. The pillars made using CZ powder are sintered at 1550°C which transforms the residual monoclinic phase to the tetragonal phase. Based on the XRD spectra of CZ in Figure 34 the residual monoclinic phase is ~ 0.1 calculated using Equation 7.

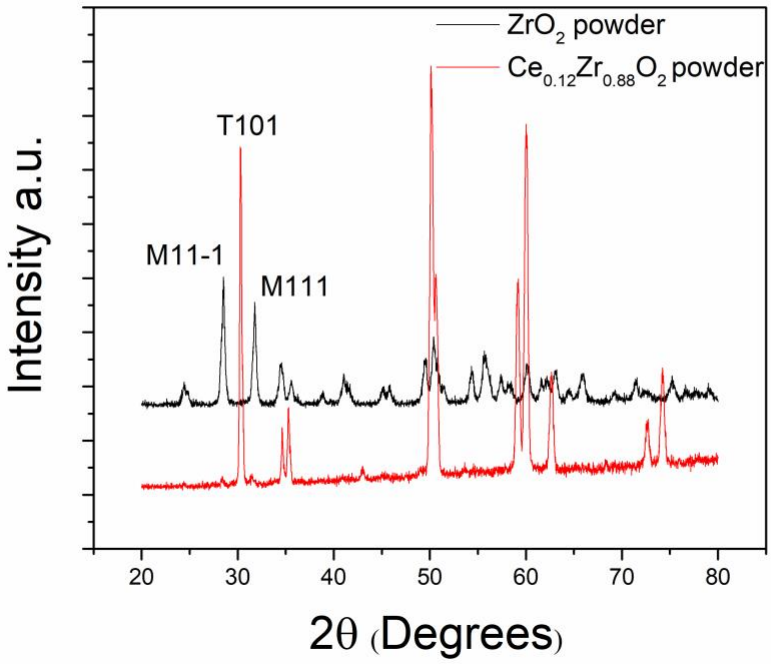

Figure 34 XRD pattern of pure zirconia and CZ powder.

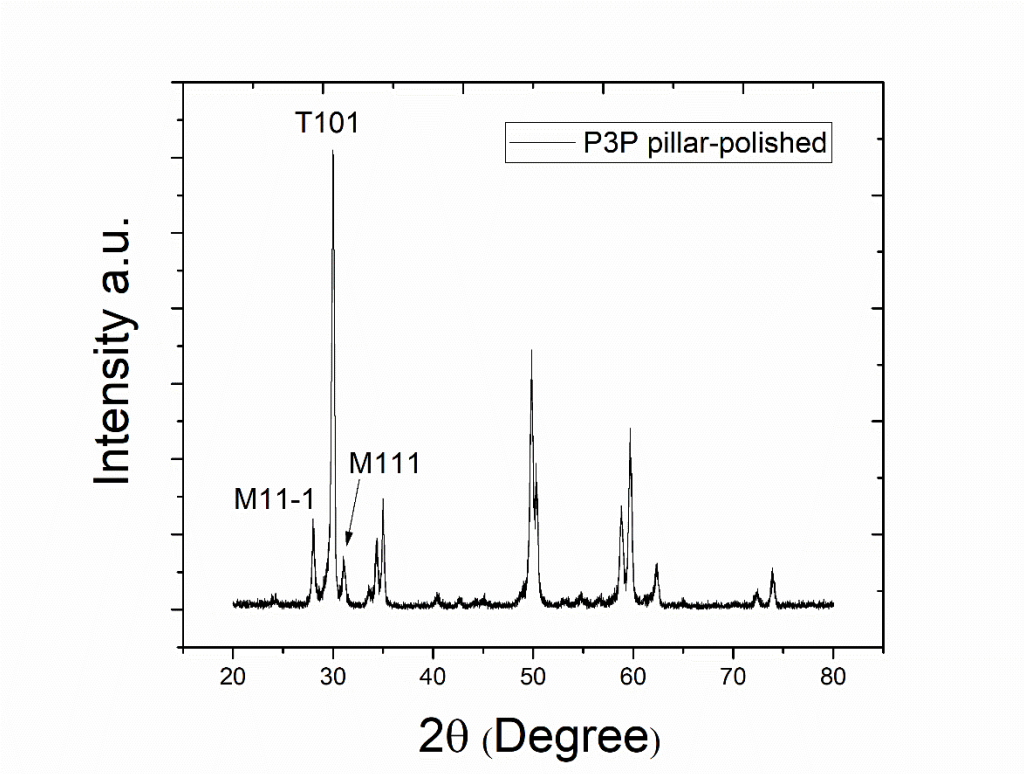

Figure 35 XRD pattern of a polished pillar showing increase in the monoclinic content after polishing induced transformation.

In Figure 35, XRD pattern obtained from a polished pillar show an increase in the intensity of the tetragonal peaks and the MC is calculated to be 0.241 using equation Equation 7. XRD patterns from sintered pillars before polishing could not be obtained since the surface is rough and the spectra obtained is very noisy with no clear indication of the intensity of the tetragonal and monoclinic peaks. The pillar used in Figure 35 was thermally treated at 500°C to recover the tetragonal phase using thermal-induced phase transformation. The XRD spectra obtained from the polished pillar after thermal treatment, in Figure 36, shows that monoclinic peak M111 has transformed extensively back to the tetragonal phase and the intensity is similar to the levels seen in Figure 34. Using equation Equation 7, the MC fraction is calculated to be 0.08 and post thermal

treatment the monoclinic phase is observed to be similar to what was observed in CZ powder i.e. 0.1.

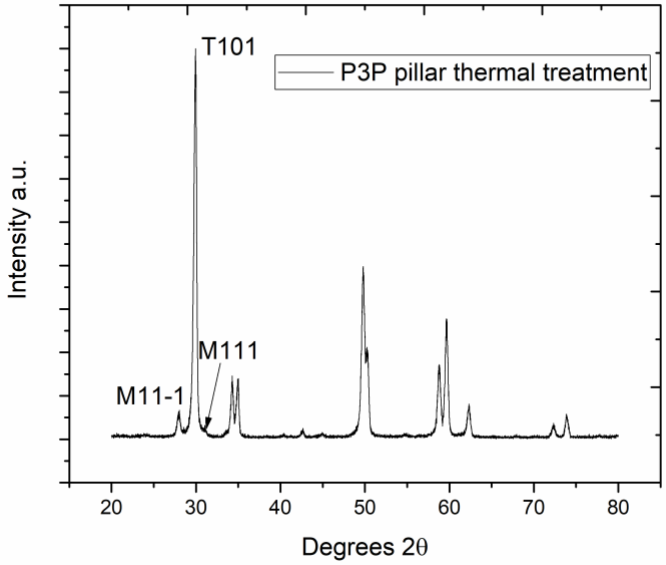

Figure 36 XRD pattern of polished CZ pillar post-thermal treatment at 500°C. The pillars show reduced levels of monoclinic phase due to thermal-induced phase transformation.

Section 4.2: Stress-induced phase transformation using Vickers Indentation

Conventionally, Vickers indentation technique is used as an effective tool to measure the hardness of a material. The hardness measured from the sintered CZ samples is approximately 13 GPa; however, we have employed this technique here to apply stress in localised regions and observe the stress-induced phase transformation and its propagation around the area. Subsequently, a series of indents are made on unpolished sintered CZ mounted in epoxy. Figure 37 is an optical image

of indents produced using 2 kg load with a 4-second loading and unloading time with 15 seconds of dwell time at peak load.

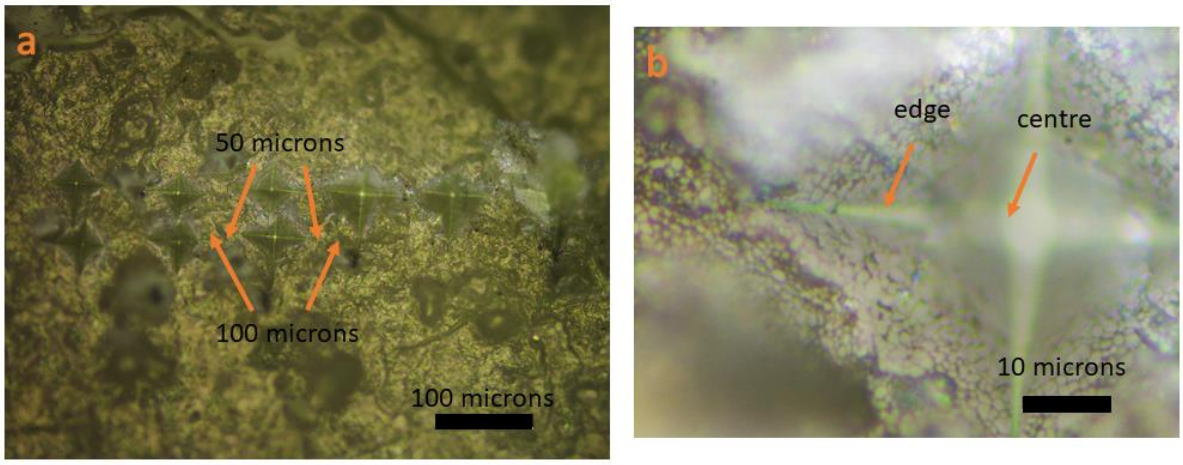

Figure 37 Vickers indentation made on the sample using 2 Kg load.

Phase analysis using Raman Spectroscopy

XRD is a powerful technique for phase characterisation in the material, but it is difficult to characterise the same in a very small area like in the case of an indent. For this Raman spectroscopy was used and the subsequent phase characterisation was done in and around the indents.

Raman spectra of pure ZrO_2, which is present in the monoclinic phase as received from the supplier is shown in Figure 38. Three peaks M171, M186 and M379, with strong and moderate intensities, will be used to analyse the change in the intensity after indentation [105].

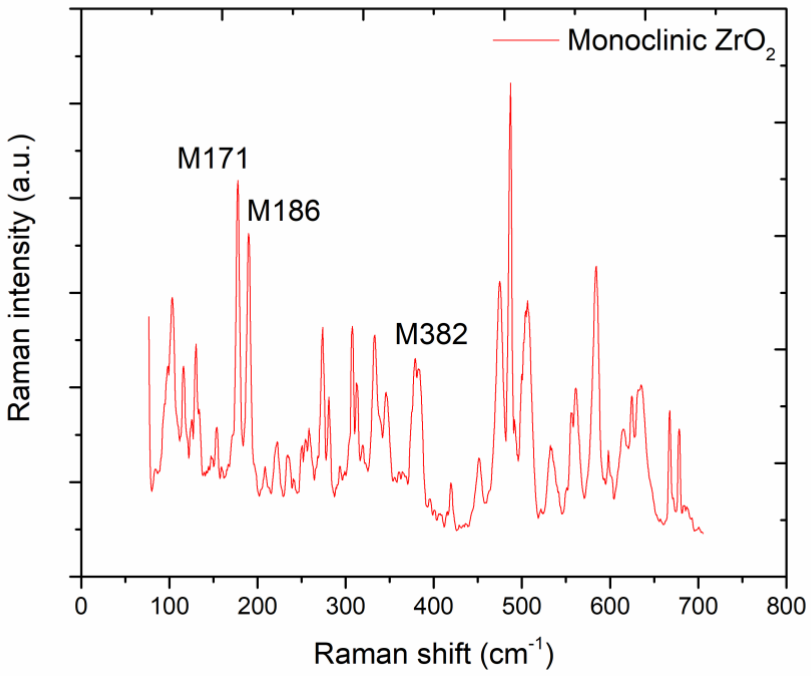

Figure 38 Raman Spectra of ZrO_2.

In Figure 39, Raman spectra acquired at different locations around the indent to detect change in phase is shown. Spectra is acquired once at 50 microns and at 100 microns on the opposite sides of the indent on the X-axis and also inside the indent and on the edge of the indent (shown in Figure 37 (a) and (b)). At frequency shift of 171 and 186, an increase in the intensity is observed inside the indent, on the edges and 50 microns away from the indent on the opposite sides of the indent. These peaks are monoclinic peaks, as observed in Figure 39 and the positions of these peaks is in good agreement with the literature [106]–[108]. There is a slight increase in the intensity of the peak at Raman shift 382 seen in Figure 39 which matches with the peak in zirconia spectra at the same intensity seen in Figure 39.

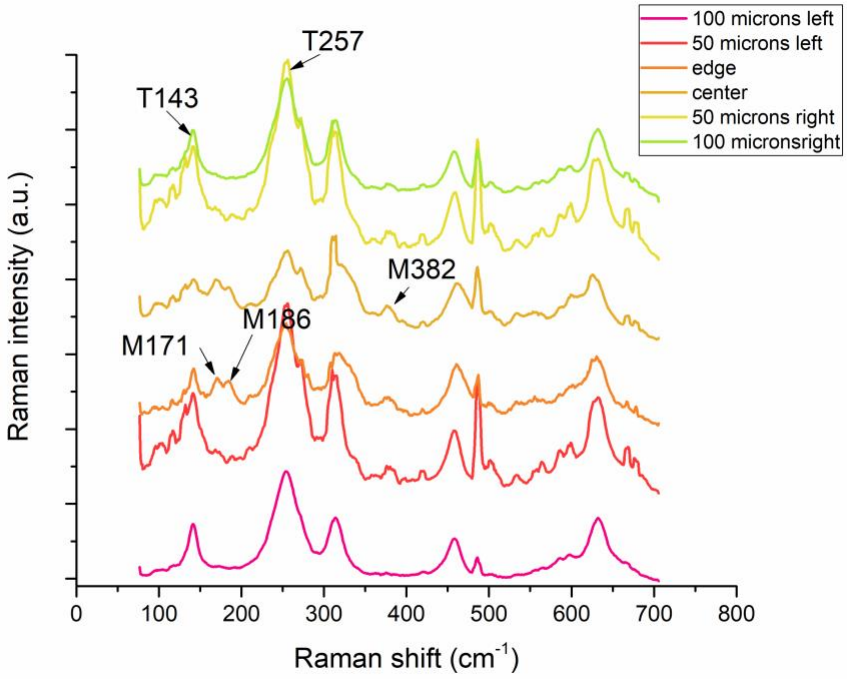

Figure 39 Raman spectra taken at equal distances on the left and right of the indents, at the edge of the indent and at the bottom of the indent.

Both XRD spectra and Raman spectroscopy show that the CZ structures produced using pseudo-3D printing technique exhibit phase transformation on applications of stress. The transformation induced using abrasive polishing over a large area is characterised using the XRD technique and the tetragonal phase is recovered by thermally treating the sample at 500°C. The abrasive polishing technique is investigated further in Section 4.4: and Section 4.5:.

Vickers indentation produced a localised stress-induced phase transformation, and this was largely confined to the indented area. It can be observed from Figure 39 that peaks 171 and 186, which match up quite well with monoclinic peak in Figure 38 are evident inside the edge and the centre of the indent. Traces of these peaks can be seen in spectra taken 50 microns away from the indent, but they are not as strong as seen in the indent. 100 microns away from the indent these peaks do

not show up in the spectra. Besides, peak 382 shows small increase appears to change its shape away from the indent and becomes stronger inside the indent. Since the load that can be produced using the machine was limited to 2 kg a higher amount of transformation could not be produced. Hence only qualitative stress-induced transformation can be shown using Vickers indentation and Raman spectroscopy.

In this section, stress-induced phase transformation in P3P, MP3P and PCP CZ structures using uniaxial compression techniques were investigated. Initially, the P3P pillars post-polishing were compressed and the subsequent change in MC is quantified as a function of applied stress. Further, the investigation was focused on compressing the MP3P pillars that can withstand higher stresses owing to the modified process and verifying the stress-induced phase transformation in them. The PCP structures were fabricated to compress at relatively higher stresses as compared to the P3P and MP3P structures, specifically at stresses developed around the pores characterised using FEA. The FEA characterisation done on the processed pillars will be discussed in the following chapter. The MC calculation was done using equation Equation 7.

Section 4.3: Stress-induced phase transformation in P3P pillars

The sintering of the ceramic structures made using P3P, MP3P and PCP processes at 1550°C ensured reversal of the residual monoclinic phase to the tetragonal phase due to thermal-induced phase transformation. The MC in CZ PCP after sintering at 1550°C is ~0.01. With such small levels of monoclinic phase present in the samples, very high stress referred to as critical stress level is required for nucleation of the monoclinic phase. P. Reyes-Morel, et al. observed that in the absence of a monoclinic nucleus, the nucleation and propagation of a monoclinic plates requires very high stress [109].

As highlighted before, the brittle nature of the ceramic material limits the stress sustaining capacity of the structure, leading to fracture prior to achieving or surpassing the critical stress required to initiate the nucleation of the monoclinic phase [20]. To circumvent the problem of pre-mature fracture, an auxiliary step of abrasion and polishing was introduced prior to mechanical loading. The polishing aided in achieving the critical stress required to initiate the nucleation of the monoclinic phase. The polished pillars were then compressed to facilitate further stress-induced phase transformation. The MC pre- and post-compression was calculated thereafter and is shown as a function of applied compressive stress in Figure 40 (a). Below 25 MPa, the increase in MC is minimal as shown in Figure 40 (b). However, the preceding MC induced due to polishing is higher which implies that the magnitude of stress applied during polishing is higher than the applied stress and the latter is not sufficient for the growth of the MC. In order to clearly distinguish MC fraction post polishing and compression, XRD spectra from polished P3P samples were taken twice and is shown in Figure 41. The MC levels observed after polishing were similar for both samples and after applying stress of 9 MPa an increase in the MC was clearly evident. The increase in the MC calculated in the pillars after the compression increases with the increase of applied compressive stress as shown in Figure 40 (b). It is worth noting that the propagation of an existing monoclinic nucleus could be ascribed to the glissile interface between the martensite and the parent phase which was reported by Wayman [110]. However, in reality the friction encountered at the tetragonal and monoclinic interface would require a certain amount of force to overcome [109] which would be lower than the critical stress required to nucleate monoclinic phase in an untransformed grain.

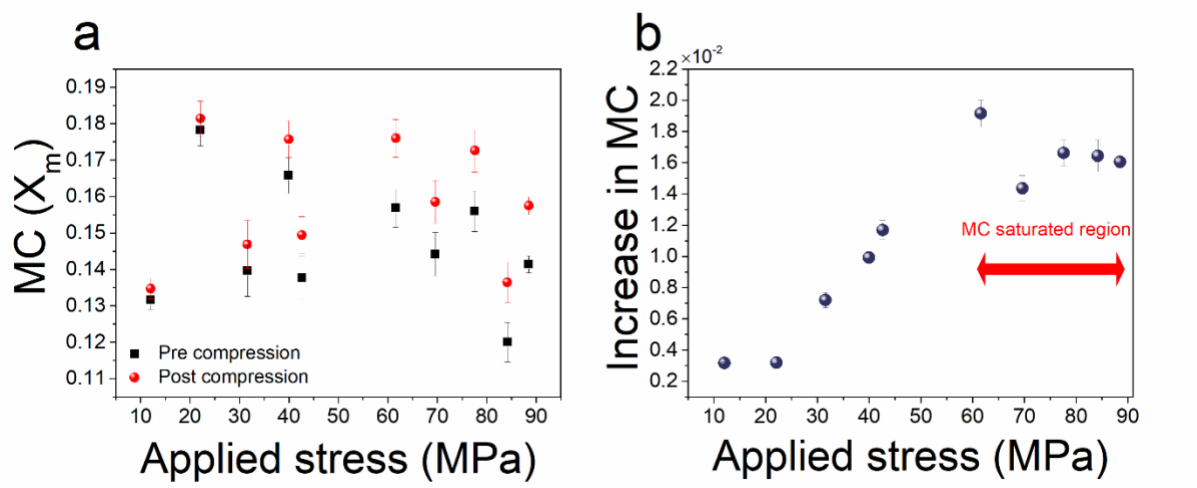

Figure 40 The change in MC before and after compression in polished pillars is shown along with figure inset with a shaded background of the MC in the pillars after polishing and after compression and XRD pattern with the peaks used for phase analysis.

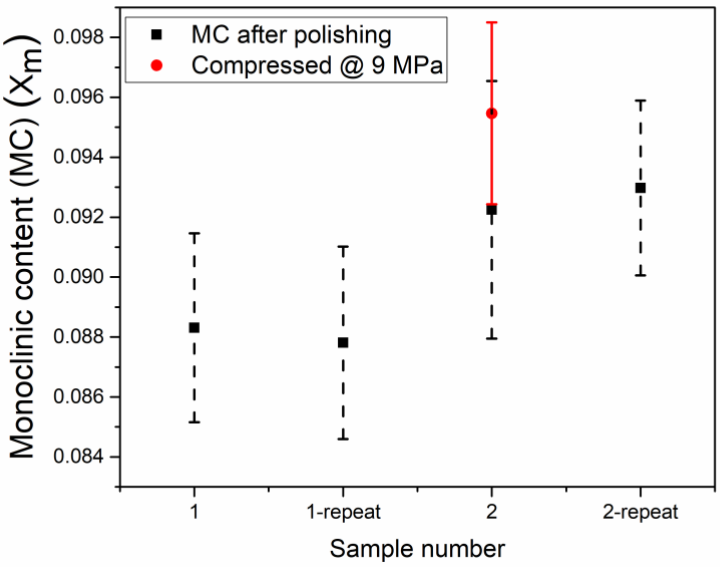

Figure 41 The MC calculated from the XRD spectra of two separate P3P samples is shown in the figure. The measurements for polished pillars are repeated twice. In the case of compression, an increase in the MC is clearly seen for sample 2 compressed at 9 MPa.

The increase in the monoclinic phase is observed to have a linear trend above 25 MPa as a function of applied compressive stress, irrespective of the initial MC produced by polishing. However, the growth of the existing monoclinic phase is observed to be dependent on the applied stress and may have very limited dependence on the initial MC induced using polishing. The increase in the MC is observed to follow a linear trend as a function of applied stress until ~60-70 MPa wherein the MC saturates.

A similar plateau-like formation was shown by Skovgaard et al. in which saturation of the monoclinic phase in tetragonal zirconia nanocrystals after ball milling was observed [111]. Yu et al. also observed saturation in granular shape memory ceramic packings wherein it was seen that at average axial stresses of 500-600 MPa, a maximum transformation level is achieved [26]. The unsintered granular packings showed a total transformation of 75% with 40% being the addition to the residual MC in as-processed powder [26]. This saturation was attributed to the shielding exhibited by the region that undergoes initial stress-induced phase transformation; this prevents the further transformation of the tetragonal phase upon further loading [26]. The apparent plateau in MC above 60 MPa (Figure 40) limits the further growth of the monoclinic phase. Though the P3P pillars were sintered polycrystalline structures, the saturation of the MC could be due to the existing transformed region serving as a barrier and preventing the further transformation of the untransformed tetragonal phase. Upon further compression, the untransformed tetragonal phase is shielded from the stress by the previously transformed region as was observed by Yu et al. [26].

Section 4.4: Stress-induced martensitic transformation in MP3P pillars

The stress-induced phase transformation in P3P pillars discussed in Section 4.3: showed the growth and propagation of an existing monoclinic phase. To further strengthen the pillar for sustaining higher stress, the pseudo-3D printing process was modified. The pillars made using the

modified pseudo-3D printing process were observed to sustain higher stress levels, as seen in Figure 42. The MC generated after compression also showed noticeable increase, as compared to the stress regime observed in the case of P3P pillars where no increase was observed. The increase in MC is approximately 1% which suggests that around 120 MPa stress levels, nucleation can be observed. Few more pillars were compressed at higher stress levels and the amount of MC is observed to increase as a function of stress. Besides, pillars compressed at 125 MPa and 225 MPa were cyclically loaded 5 times at the same stress levels to observe the growth of the monoclinic phase. An increase is observed in the MC levels as compared to the initial MC post first compression. Figure inset Figure 42 shows maximum stress in FEA as a function of applied stress which will be discussed in detail in Section 5.2:.

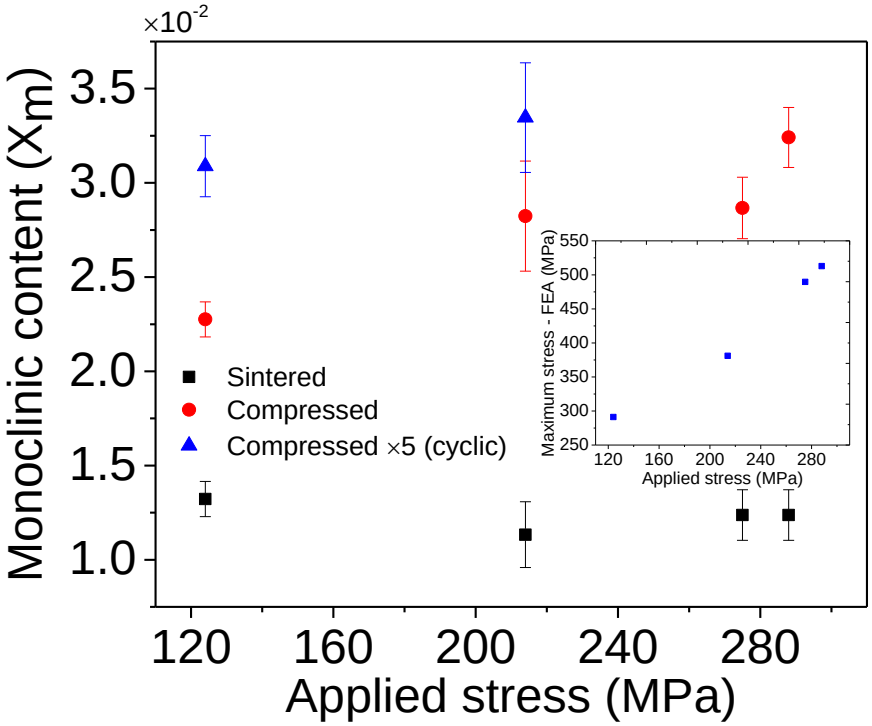

Figure 42 (a) MC observed in pillars made using the modified pseudo-3D printing process after sintering, after compression and after cyclic compression and figure inset shows maximum stress observed in FEA as a function of applied stress.

Section 4.5: Stress-induced phase transformation at the stress levels around pores.

In the MP3P pillars, the stress regime showed that nucleation and subsequent growth of the monoclinic phase increased as a function of applied stress. The growth was observed in the case of cyclic compression as well. The findings provide concrete evidence of nucleation and further growth upon cyclic compression in this regime. PCP made using the process discussed in Chapter 2 were subjected to the same thermal treatment as compared to the modified pseudo-3D printed pillars. The pellets were then compressed at stress levels shown in figure inset Figure 43 (extracted

from FEA discussed in Chapter 5) and XRD spectra from the pellets were obtained after sintering and after each compression cycle. Figure 43 shows the difference in MC between consecutive cycles and it is observed that the maximum difference is between MC after first compression and after sintering. The difference reduces as the compression cycles increase. The findings suggest that the first compression cycle nucleates the ceramic body, and upon further compression, the monoclinic phase grows in the nucleated grains. Pellets cyclically compressed at 600 MPa, were compressed further at higher stress levels to understand the growth mechanism and the subsequent increase in monoclinic phase. No significant change was observed when compressed at 650 MPa. At 700 MPa a slight increase is observed, but at 750 MPa it does not increase further. The pellet failed post 750 MPa and no further compression could be done. A very low amount of increase in MC at higher stresses suggest saturation in the monoclinic phase fraction.

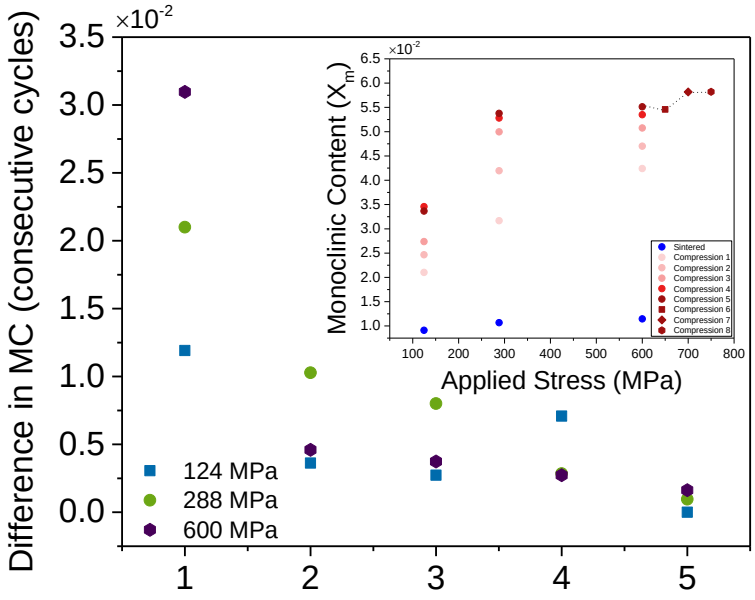

Figure 43 The difference in MC between consecutive cycles is observed to be reducing after each compression at a given stress level and figure inset shows MC after each compression. Post cyclic

compression at 600 MPa, the body was compressed at higher stresses to observed additional nucleation.

Post compression, the stress levels that are observed in the microstructure varies from the interface between the pillar and the anvils and as it further propagates in the bulk. It would be maximum in the region around the interface. But, in the case of the non-uniform distribution of voids, due to reduced cross-sectional area stress concentration regions would appear in and around the void region. Such microstructure would show amplification of stress levels as compared to the stress at the top surface. The area around the pores would shows varied stress levels that would reduce as the stress propagates away from the void into the bulk but would increase in the case of overlap with the stresses from the neighbouring pores. FEA (discussed in detail in next chapter) suggested that the amplification is by 2-3 times as compared to the stress levels observed on the top surface.

Chapter 5 Characterisation of stress distribution in porous mesostructure using Finite Element Analysis.

In this chapter, we have used CAD and FEA as tools to simulate the stress distribution in the microstructure observed in the P3P and MP3P pillars as a function of the applied stress. The simulation factored in the microstructure and its effect in optimising the stress levels observed due to the porosity mapped in accordance to what was observed in the porous polycrystalline sintered ceramic structures. The applied stress is equivalent to the stress applied to the P3P and MP3P pillars during uniaxial compression.

Section 5.1: Analysis of stress distribution in P3P pillars.

Based on the microstructure seen in Figure 9 (d), a computer aided design (CAD) model was made using SolidWorks and is shown in Figure 44 (A) for P3P pillars. The compression experiment was simulated in ANSYS software. The CAD model represented the region that would fall within the depth of penetration of X-rays and would facilitate easy comparison between the model and the X-ray diffraction. The CAD model is meshed and can be seen in Figure 44 (B). Equivalent force to the stress observed in pseudo-3D printing while compression is calculated for the CAD model (Section 7.1:). The equivalent force was then applied to the CAD model along with other constraints and simulated in FEA software to analyse the maximum stress levels developed around the pores, example of such a simulation can be seen in Figure 44 (C). Figure 44 (D) shows graphically the constraints applied to the CAD model during simulation. The maximum stress is observed only at a few nodes and as the stress propagates in the bulk the stress levels reduce. In the event of stress layers from separate pores converging, the possibility of stress amplification is

observed, and the stress levels may not recede as it would be in the case of bulk with no pores. This is further investigated in the latter part of the chapter.

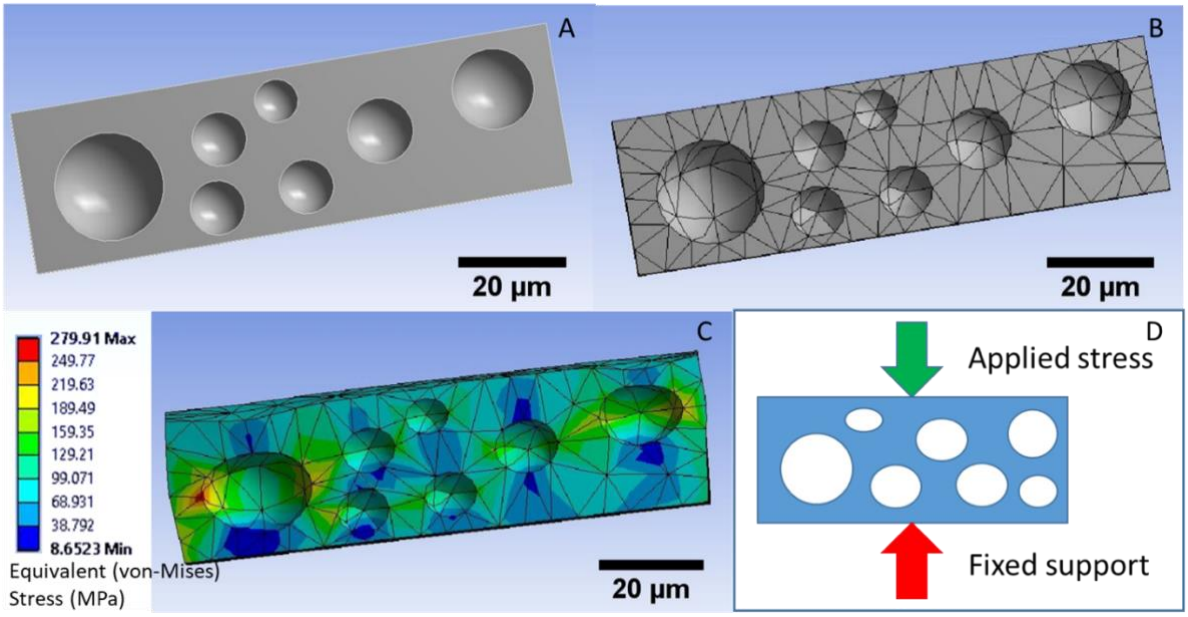

Figure 44 (A) CAD model used for FEA, (B) CAD model with mesh (C) stress distribution around the pores and (D) graphical representation of stress distribution around the pores according to the constraints applied during simulation.

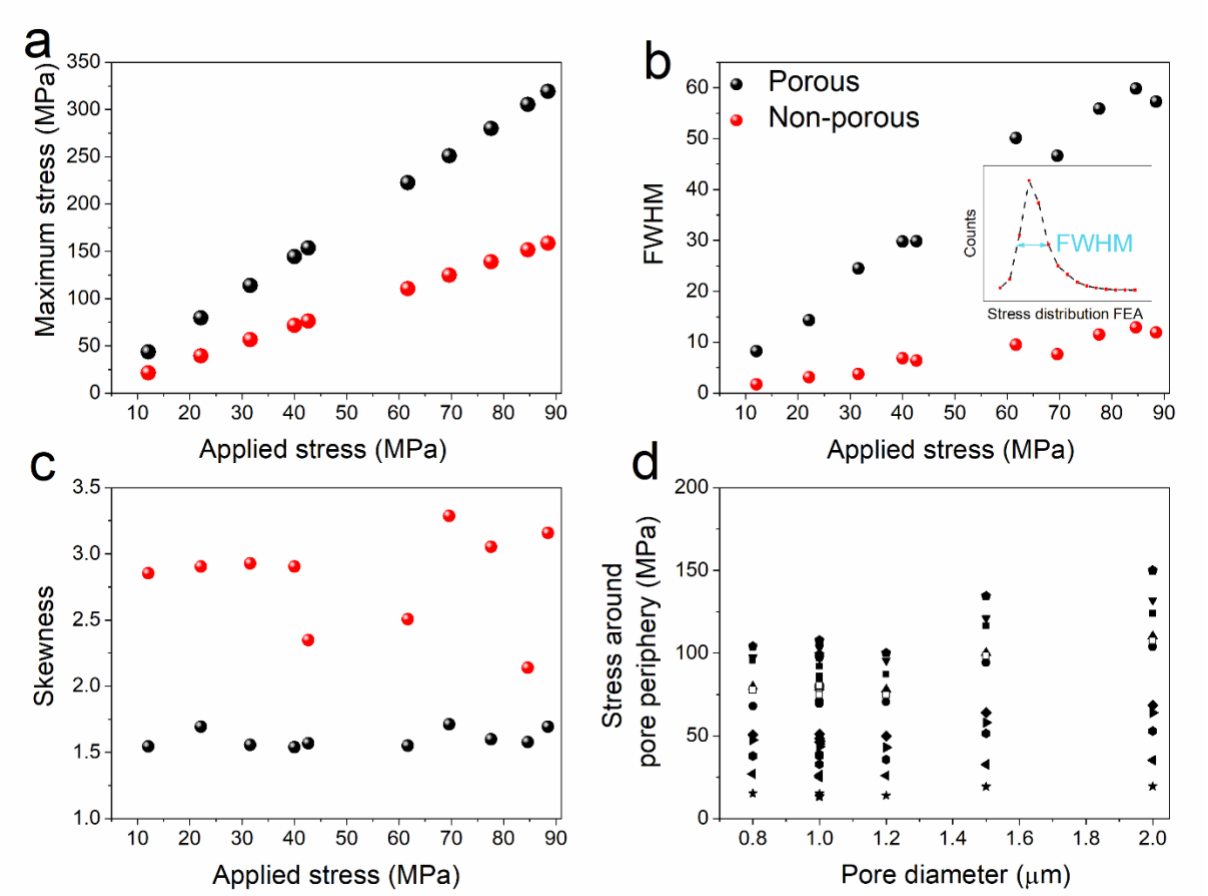

Figure 45 (a) Maximum stress, (b) FWHM and (c) skewness obtained by the CAD-FEA model as a function of applied compressive stress; (d) stress levels observed around the pores in the CAD-FEA simulation.

FEA was employed to analyse the stress distribution around the pores. For comparison, a CAD model Figure 46 with no pores (i.e. non-porous) and the same dimensions as the CAD model shown in Figure 17 (a), was also designed. The peak stress observed by FEA for both porous and non-porous CAD models is shown in Figure 45 (a) as a function of applied stress during compression. Both the porous and non-porous CAD models exhibit a linear trend as a function of

the applied stress; however, the slope is greater for the porous model as compared to the non-porous model.

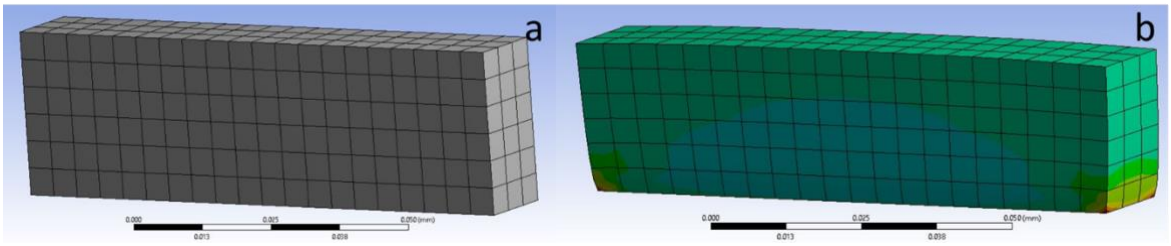

Figure 46 CAD model with no pores used for FEA in the (a) and (b) lower stress regime.

The maximum stress observed in the FEA simulation is higher than the applied stress in P3P pillars during the compression and these stress levels are localised around the pores. As expected, a gradient exists whereby the stress levels recede as the distance away from the pore increases. Also, the occurrence of the maximum stress is only observed at a few nodes in the bulk of the material. The stress levels thereby could be of the critical level and facilitate stress-induced phase transformation. Thus, the porous structure can help in achieving such sites for the nucleation of the monoclinic phase at several areas around the pores, which is impossible in a non-porous structure due to the absence of these geometric enhancements.

From the FEA analysis, stress distribution curves were acquired and FWHM of the distribution curves were calculated. The FWHM for both porous and non-porous CAD models, as shown in Figure 45 (b), was used to further analyse the stress distribution and its related variation. The FWHM of the porous model is observed to be higher than the non-porous model. As a function of the applied stress, the FWHM of the non-porous model does not show a significant change, whereas porous model shows an increasing FWHM. This is primarily due to geometric effects around the periphery of the pores resulting in a higher stress variation. In doped zirconia, crystal

orientation dependence was observed in stress-induced martensitic transformation and thus the critical stress was observed to vary for different crystal orientations [19]. The varying stress levels observed around the pores in the FEA simulation show a high probability of nucleating the monoclinic phase in the grains provided the orientation favours the phase transformation. Further to this, the grains encompassing the pore that experience varying stress levels would have a facet or facets that is exposed to the pore and therefore would have unconstrained free surfaces. Due to this, such grains would show a high possibility of accommodating the shear strain produced in the grains whilst undergoing stress-induced martensitic transformation that underlies the shape memory effect as compared to polycrystalline dense structures. However, such considerations require further investigation.

The shape of the stress distribution curve was further analysed by measuring the skewness of the curve. Figure 45 (c) shows the porous samples with a bias towards the negative skew as compared to non-porous CAD models. The skewness obtained from the porous CAD models is observed to be uniform as a function of applied stress as compared to the non-porous CAD models. The uniform shift towards higher stress due to the presence of pores suggests an increase in the probability of the nucleation of the monoclinic phase and the growth of the phase in the structure.

The independent effect of pores in stress optimisation was analysed by measuring the stress distribution around the pores and are plotted as a function of the pore size in Figure 45 (d). Ten sites were probed to measure the stress levels, the first site at a distance of 0.1 microns from the pore and the rest at equal distance from each other in the measured area shown in the Figure 48. The maximum stress was observed around the pore with the largest diameter; consequently the largest variation in stress levels was obtained in the pore with the largest diameter. Though the average from all the ten pillars (shown as a hollow marker in Figure 45 (d)) shows a slight increase

as a function of diameter however the difference is not significant compared to the highest and lowest stress level that can be observed. Each marker represents an average of ten readings per pore which is shown as a function of the pore size. The variation does not show a significant change in the stress levels around the pore. Therefore, it can be inferred that despite the variation in stress levels produced around the pores, the average difference in the stress levels irrespective of the pore size may not be significant. Similar such finding was reported by Davis et al. [112] and Jaeger et al. [113], where it was stated that there is no dependence of stress concentration on the pore size. Though the average difference may not be significant, the peak stress levels observed near the pore is confined to a limited number of nodes. The severe localisation of maximum stresses would limit any phase transformation to the immediate vicinity of these regions. Thus, the transformed region would have a shielding effect, thereby limiting further stress-induced phase transformation and is in good agreement with the experimental observations from the P3P samples.

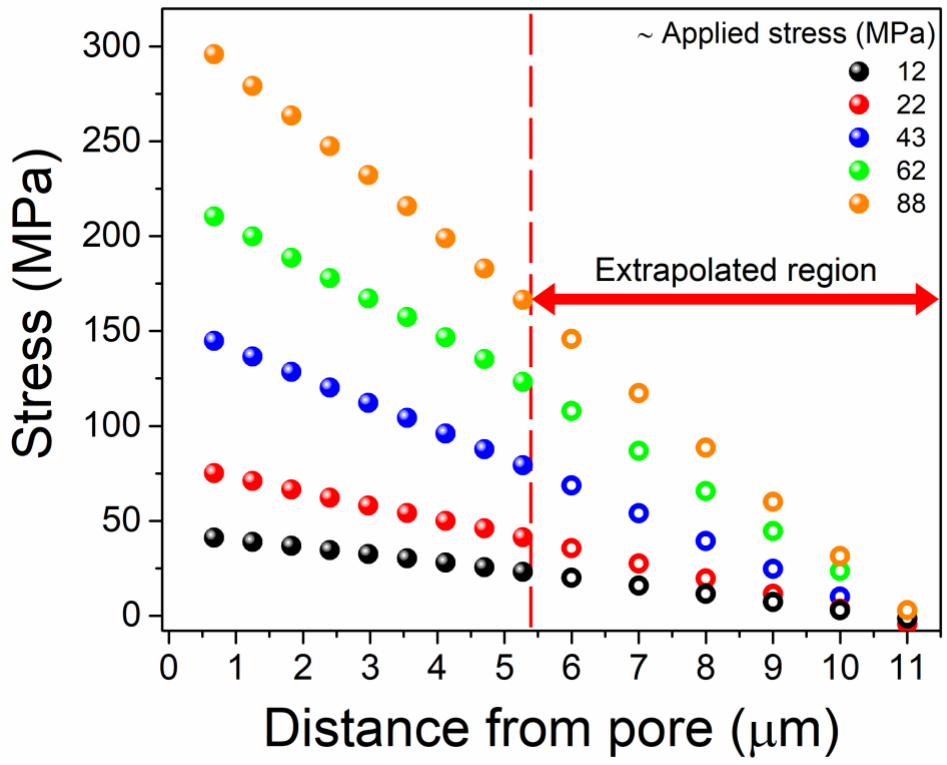

Figure 47 Measured and extrapolated stress levels in the localised region as a function of distance from the pore.

The FEA simulation revealed a localised stress concentration at the periphery of the pore with the largest diameter, which subsides as the stress propagates away from the pore. The stress propagation in the bulk from the localised area was measured and is shown in Figure 47. The measured area around the pore is shown in Figure 48. As it can be seen in Figure 47, the stress shows a reducing trend as the distance from pore increases. At lower applied stress the reduction in stress levels (moving away from the pore surface) is gradual compared to the higher applied stresses where the decrease (i.e. negative slope of the lines) in stress levels is significantly higher. The increasing stress gradient suggests a limit to the ability of supercritical stresses to propagate

into the bulk of the material and away from the pore surfaces. This would naturally limit the prospect of stress-induced phase transformation of the untransformed CZ material.

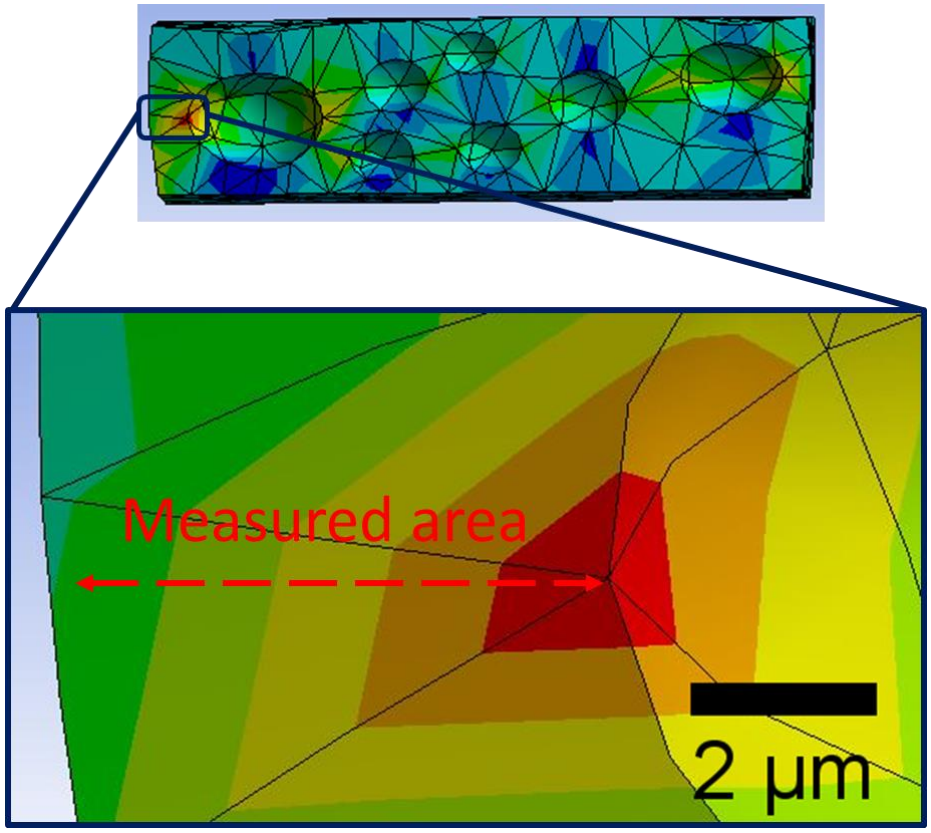

Figure 48 CAD model used to measure localised stress around the pore. Zoomed in figure shows the measured area.

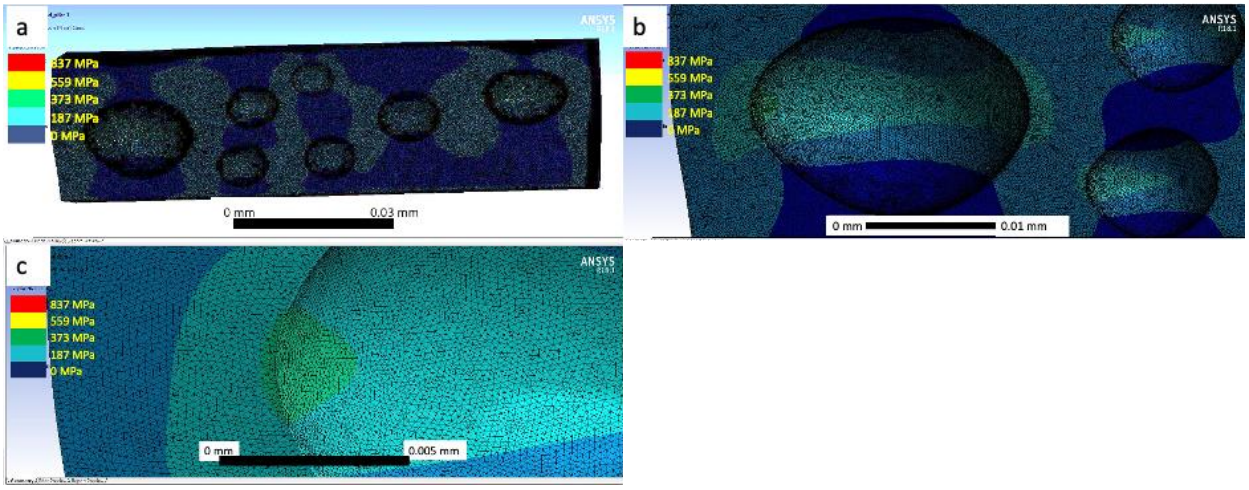

Figure 49 CAD model with fine mesh. Element size is 100 nm.

As observed in Figure 44 (C), the maximum stress concentration zone is around the pore with large diameter. The highest stress zone is observed in a few elements. However, this stress concentration zone is also at the node of these elements. This develops an ambiguity with regards to the source of the stress concentration zone. Also, as observed in Figure 9 (e) the grain size is ~2-4 microns and the elements size of similar size in the CAD model. In order to eliminate the ambiguity, the mesh size was reduced further which would give a uniform stress distribution by ensuring that each grain comprises of several small elements thereby reducing the possibility of excess stress accumulation at element nodes. The images in Figure 49 show the CAD model with mesh size of 100 nm at different levels of magnification.

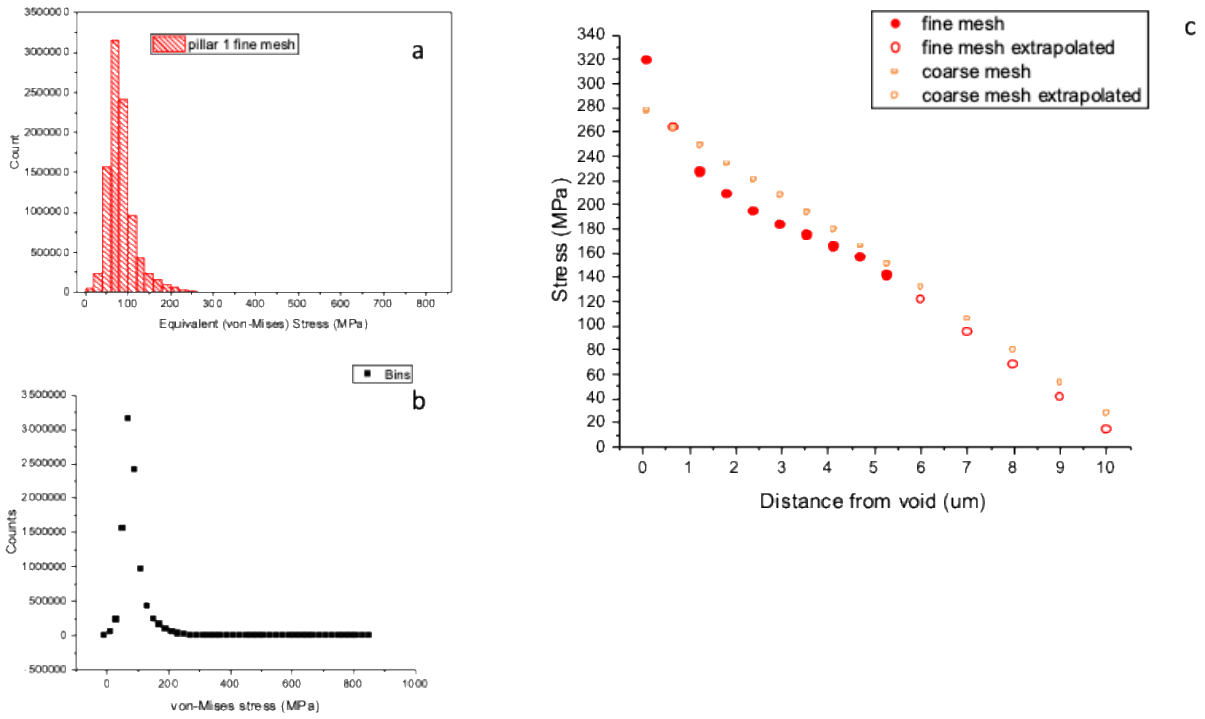

Figure 50 (a) Histogram shows stress distribution in the CAD model with fine mesh, (b) shows normal distribution curve and (c) shows the stress propagation away from the maximum stress zone developed near the large void. The force applied in the simulation is equivalent to the pillar which sustained applied stress of 76.6 MPa.

The stress distribution observed in the CAD model post FEA analysis is shown in Figure 50. The histogram in Figure 50 (a) shows the range of the stresses observed in the elements. The maximum stress observed is ~800 MPa, however it is confined to only a few elements. The normal distribution curve is shown in Figure 50 (b). In Figure 50 (c), the stress propagation from the void is characterised and compared with the CAD model having coarse mesh. The trend observed is

similar i.e. the stress is observed to reduce as the distance from the void increases. It is also observed that the maximum stress observed in the fine mesh is higher as compared to the coarse mesh. However, it is lower than the maximum stress observed in the stress distribution histogram. Further, the reduction in stress levels is observed to be higher than in the case of coarse mesh. This has resulted in a difference in the trend line of coarse and fine mesh which is at a distance of ~ 1 to 4 microns. The fine mesh refines the stress distribution and therefore the stress propagation is observed accurately. Such analysis with finer mesh would refine the results and accurately show the stress optimisation that can be achieved around the pore upon application of stress.

Section 5.2: Analysis of stress distribution in MP3P pillars.

CAD model in Figure 51 (a) represents the distribution of pores and the dense layer on the sides, top and bottom formed due to the CZ powder placed around the pellets during stacking. The top region is 30 microns to match with the depth of penetration of X-rays. Figure 51 (b) shows the model post meshing. Figure 51 (c) shows the stress distribution post-simulation of the pillars that sustain 124 MPa as observed in Figure 42.

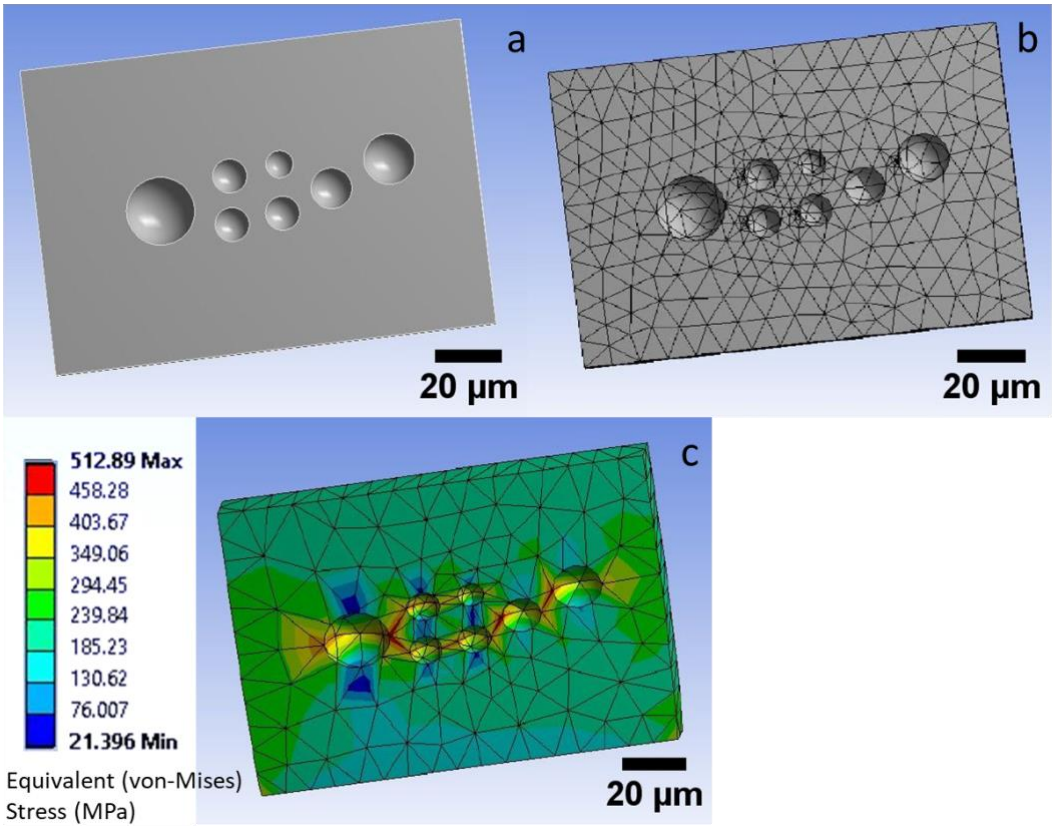

Figure 51 (a) CAD model of the pillars made using modified process used for FEA, (b) CAD model with mesh and (c) stress distribution around the pores.

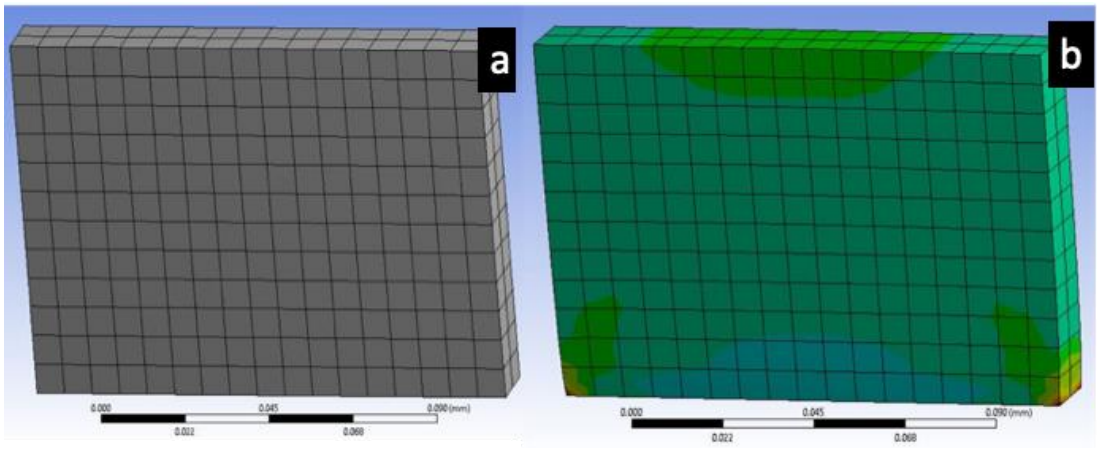

Figure 52 (a) meshed CAD models with no pores used for FEA and (b) the stress distribution in the microstructure in the MP3P samples.

For comparison, a dense CAD model with no pores of the same dimension as that of the CAD model representing the MP3P pillars is shown in Figure 52. Similar to the P3P pillars, in MP3P pillars also the stress concentration is observed around the pores. The maximum stress concentration zone can be seen around the pore with the largest diameter. However, the stress concentration zone is observed to be dense (Figure 51 c) on the right of the pore with the largest diameter as compared to the P3P pillars wherein the zone is on the left of the pore (Figure 44 c). The zone is observed to link two separate stress concentration zones formed from separate pores. The stress optimisation formed due to such proximity is investigated further in the latter part of this chapter.

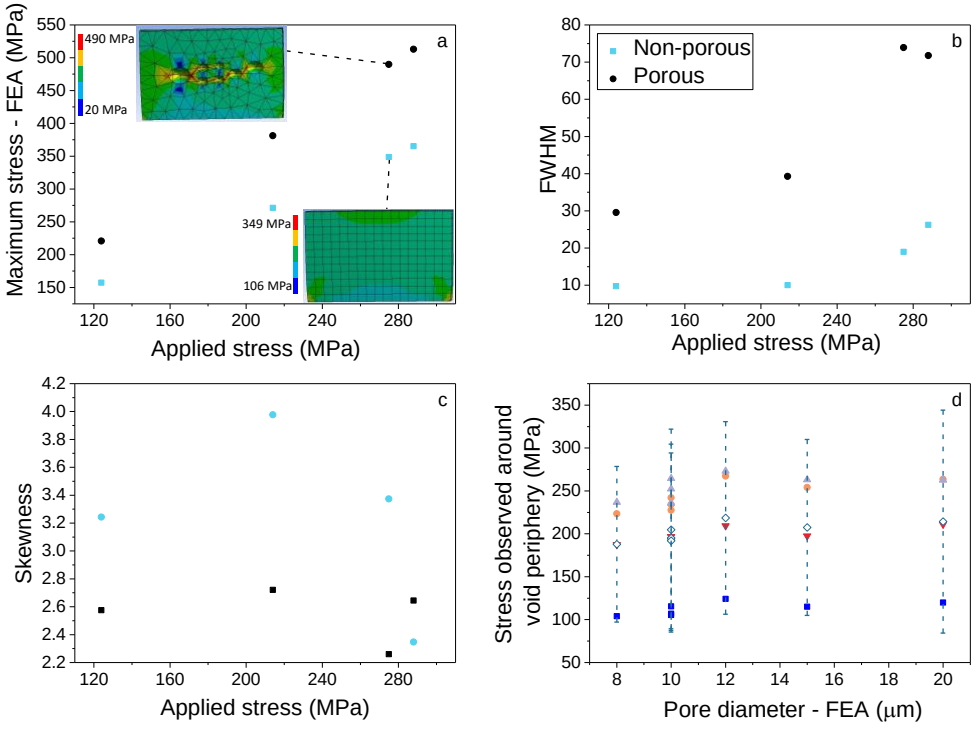

Figure 53 (a) shows the maximum stress (b) FWHM, (c) skewness and (d) stress levels measured around the voids during FEA simulation depicting compression of pillars made using modified pseudo-3D printing process.

Similar to the lower stress regime, maximum stress, FWHM and skewness are derived from FEA analysis of both porous and non-porous CAD models of dimensions, as shown in Figure 53. Porous models show higher stress levels as compared to non-porous models, as seen in Figure 53 (a). FWHM also shows higher variation in stress levels in porous structures as compared to non-porous structures and is shown in Figure 53 (b). Similarly, skewness also shows an inclination towards negative skew in porous models as compared to non-porous models, as shown in Figure 53 (c). Stress levels around the voids show no significant difference in the average in different sizes of the voids and are shown as a hollow marker and dashed error bar in Figure 53 (d). Averages of 10 readings per pillar for respective void size also didn't reveal any significant change in stress levels observed around the void shown as coloured markers in Figure 53 (d). Similar localisation of stress was observed around the void with the largest diameter as that of the lower stress regime, but measurements were not taken since it is quite likely that similar saturation of stresses would be observed.

Section 5.3: Stress optimisation based on pore fraction.

In the case of both P3P and MP3P pillars, the porosity observed is due to the thermal treatment that includes the burning off of the polymer resulting in creation of pores. However, in the case of optimising stress-induced phase transformation by using pores as stress concentrators, it is desirable to have much higher control with respect to pore distribution and pore shape as well. Ideally, in the case of increasing the pore fraction, the sites that would show optimised stress levels would be more than in the case of structures with low porosity. This implies that the possibility of higher stress-induced phase transformation can be achieved in the entire structure as the porosity increases provided the optimised stress levels are capable of nucleating the monoclinic phase in and around the pores. However, with the present 3D printing infrastructure it is difficult to control

the porosity in structure to such a large extent. Therefore, with the aid of FEA, the stress distribution around the pores can be simulated and thereafter the concentration and its propagation can be analysed. Here we investigated two separate CAD models, one with single pore and the other with two pores.

By using the two pores approach, we intend to produce interconnected stress concentration zone and analyse the stress distribution in such a zone. Such a zone was created in FEA of CAD models representing the microstructure of MP3P samples in Figure 51 (c).

By applying constraints similar to observed in Figure 44 (d), the stress formation and its further propagation as a function around the pore in both the models was analysed.

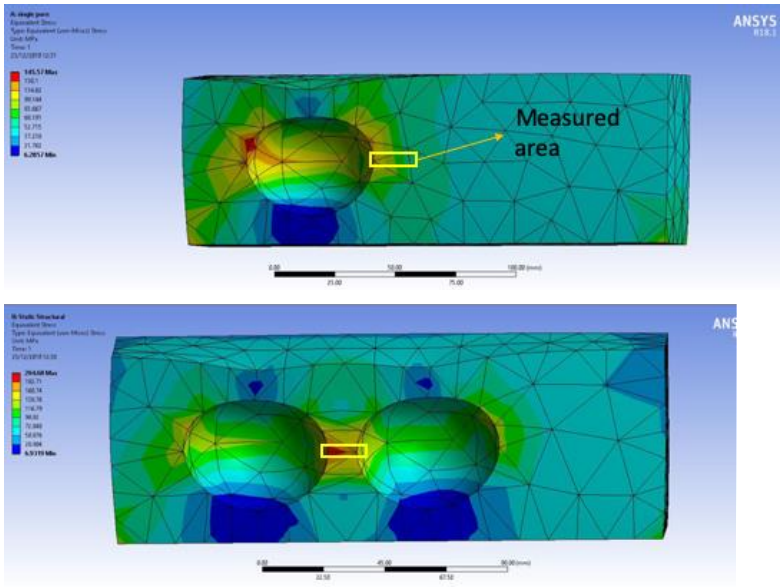

Figure 54 CAD model with one and two pores used for the FEA simulations. The area in the yellow rectangle was probed for the stress levels.

In Figure 54, the CAD model with single pores and two pores used for the FEA simulations is shown. Various levels of forces were applied to simulate the stress formation around the pore and its further propagation.

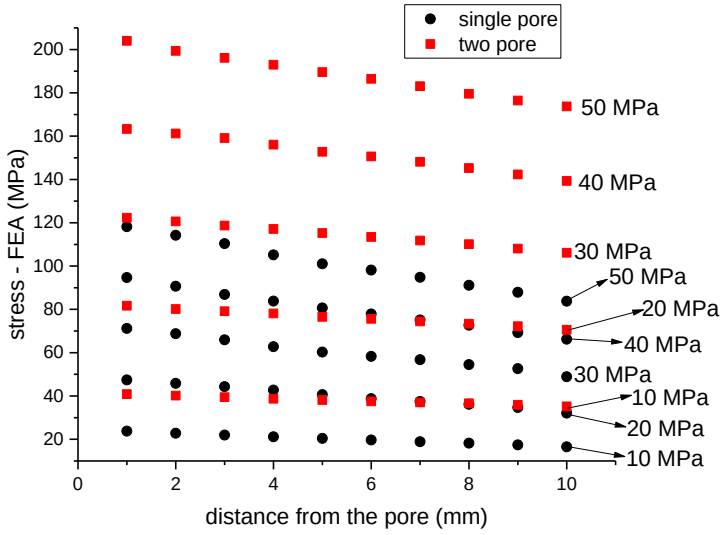

Figure 55 Stress observed around the pore in FEA simulation of single and two-pore CAD model.

The stress levels observed in the measured area are plotted as a function of the distance from the pore and is shown in Figure 55. The applied stress levels were from 10 to 50 MPa, with intervals of 10. It was observed that the maximum stress was observed near the pore and it subsided as the distance from the pore increased similar to the observations seen in the previous section. However, the slope of the stress measurements taken from the single pore was observed to be higher as compared to the slope observed in the model with two pores. Due to this the optimised stress level were observed to sustain till much further distances away from the pore in the model with two pores as compared to the single pore. This implies that with such stress distribution more grains can possibly sustain critical stress levels and can nucleate the monoclinic phase provided the anisotropy favours such transformation and the structure as a whole can generate a higher monoclinic content. The reducing distance between pores increases the density of the pores in a given area thereby increasing porosity but reducing the modulus of the structure as a whole. This could be a drawback in the case of producing structures with a very high elastic modulus.

Section 5.4: Stress optimisation based on pore shape.

As mentioned earlier, the other alternative to optimise stress levels in the bulk is by varying the shape of the pore in the bulk. In the earlier work (described in detail in Chapter 3) the role of facets and sharp edges in CZ particles were observed to play a crucial role in producing higher MC. Therefore, a systematic approach in increasing the number of facets and sharp edges in the pores was investigated. The different shapes of the pores investigated besides sphere were square, rhombus and cylindrical pores. These shapes were designed and embedded in CAD model and applied with force to analyse the stress developed around the pore. The size of the CAD model is kept the same for all the different pore shapes. The position of the pore is kept the same in all the cases for both single and two-pore configurations. The size of the pore is also kept the same thereby maintaining the same pore fraction for all the configurations.

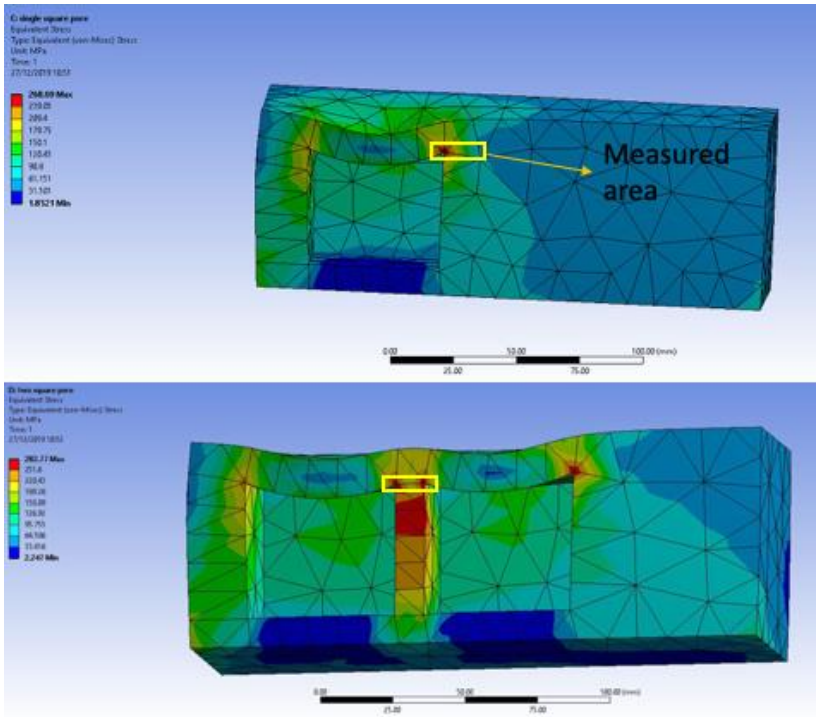

Figure 56 Stress distribution observed using FEA in a single and two-pore square-shaped configuration.

In the case of square-shaped pores, the stress distribution around the pore is shown in Figure 56. It is observed that the maximum stress in the case of single pore is observed at the intersection of a vertical and horizontal edge. The maximum stress propagation in the bulk was probed for a distance of 10 mm and is shown in Figure 57. It is observed that as the distance from the maximum stress concentration zone increases the stress is observed to reduce gradually. In the case of two-pore configuration, the maximum stress observed is similar as compared to the single pore configuration.

However, as the distance from the single pore in the measured area increases the stress reduces up to a 5 mm and the trend is observed to reverse exhibiting higher stress levels in the vicinity of the second pore. The stress levels are similar to the maximum stress observed at the intersection of the

two edges. Also, below the measured area (in the vertical column) the region between the two pores is observed to show severe stress concentration zone wherein the stress levels are not observed to reduce (probed stress levels in the measured area Figure 56).

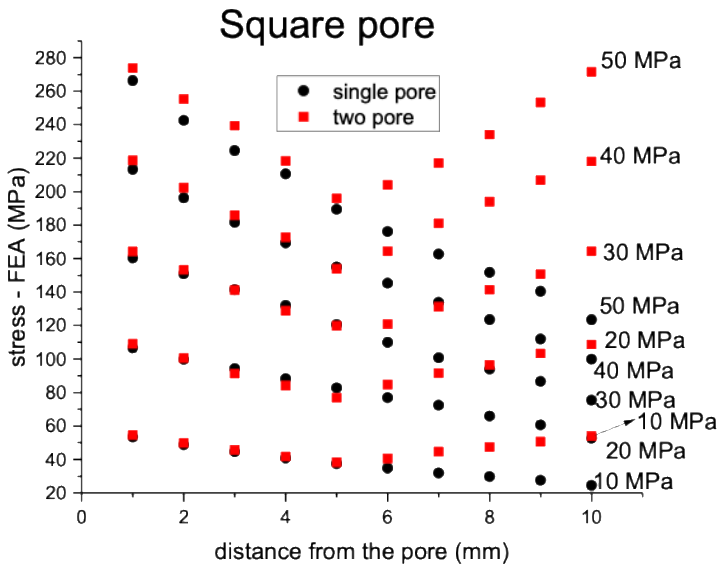

Figure 57 Stress measured around the square-shaped pore as the maximum stress propagates in the bulk.

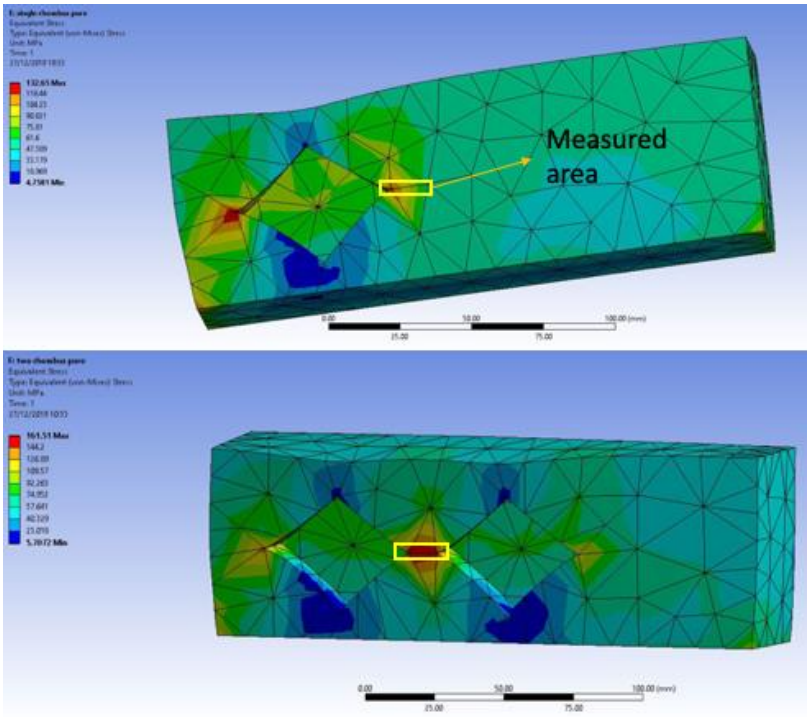

Figure 58 Stress distribution observed using FEA in rhombus-shaped single and two-pore configurations.

The shape of the pore was modified further by tilting the geometry of the pore at an angle of 45 degree to form the shape of a rhombus. This retained the number of sharp edges and corners, but the perpendicular force is acting on a tilted cross-section of the pore which was different in the case of a square pore. Due to this tilt, the cross-section forms a vertex due to the intersection between the two edges as compared to the square pore wherein it is a flat edge. In the case of rhombus, though the vertex now shows a reduced cross-section under applied stress, but the stress concentration does not appear in this region. The stress concentration region is highlighted as measured area in Figure 58. This region sustained the maximum stress and the stress propagated in the bulk is measured as a function of the distance from the pore and is shown in Figure 59. The stress levels gradually reduce as the distance from the pore increases. However, in the case of two-

pore configuration, it is observed that the maximum stress zone is retained and no reduction in stress levels is observed in the probed area as the distance from the pore increases.

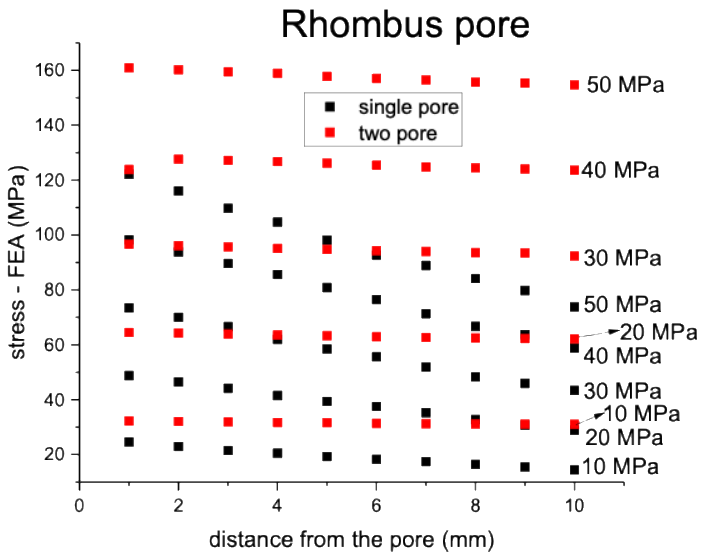

Figure 59 Stress measured around the rhombus-shaped pore as the maximum stress propagates in the bulk.

The square-shaped pores were modified a bit further and instead a curvature was introduced in the shape of the pore in order to make the pores cylindrical in shape. It was observed that the maximum stress was developed in the same area as that of the square-shaped pore and is observed in Figure 60. Further, the propagation of this maximum stress is observed to follow similar trend that of gradual reduction as the distance from the pore increases.

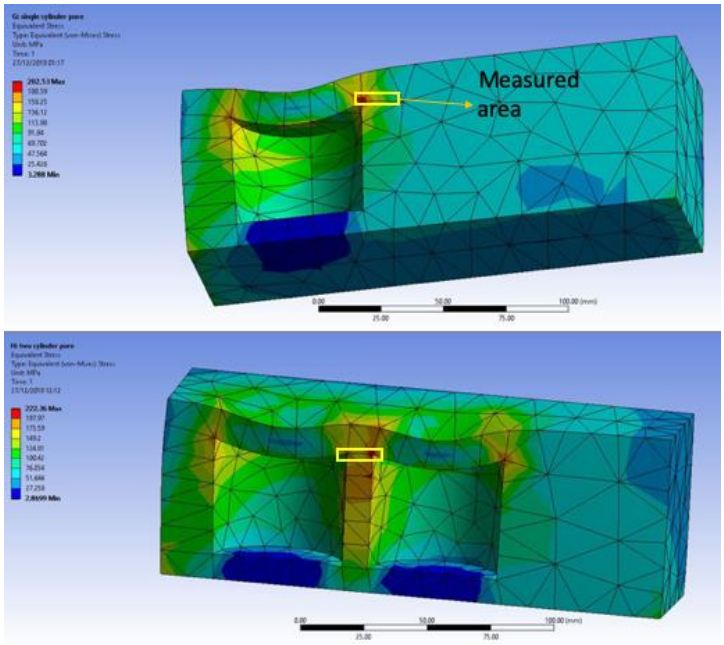

Figure 60 Stress distribution observed using FEA in cylindrical shaped single and two-pore configurations.

The stress levels probed tend to reduce up to a distance of 5 mm from the region where maximum stress is observed and the trend is later reversed, shown in Figure 61. The stress levels further increase and exhibit levels similar to the maximum stress which is at a similar location of the pore on the right as compared to the pore on the left. The trend in stress distribution observed in the case of cylindrical pores is similar to that of stress distribution observed in the case of square-shaped pores.

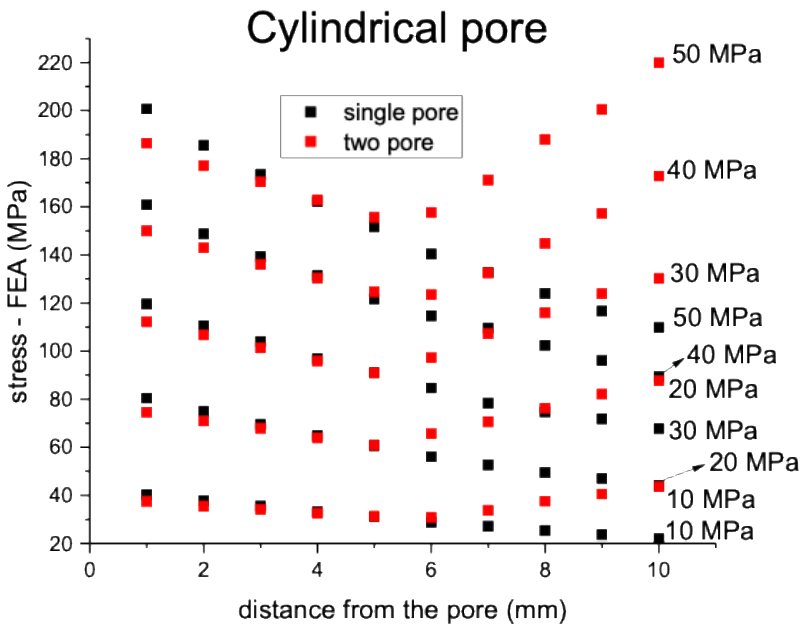

Figure 61 Stress measured around the cylindrical-shaped pore as the maximum stress propagates in the bulk.

Different zones of stress concentration were observed in the single and two-pore configurations. The maximum stress observed in each of the configuration for a specific applied stress is shown in Figure 62. It is observed that changing the pore shape from sphere results in higher formation of stress levels around the pore.

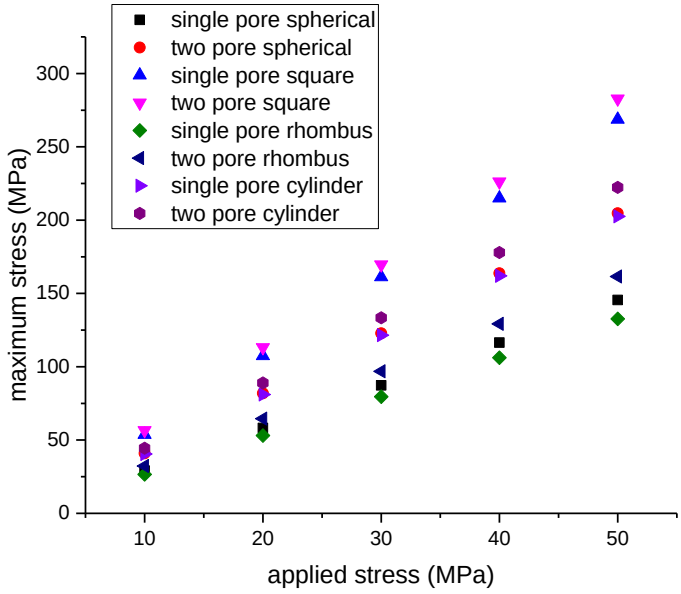

Figure 62 Maximum stress observed in CAD model with varying pore shapes.

The CAD model with two pores is observed to show maximum stress to be higher as compared to the CAD model with a single pore. Also, it is observed in Figure 54 that the location of stress concentration in single pore model is towards the edge on the left of the pore whereas in the case of two-pore it is between the two pores. The maximum stress concentration zone between the two pores also show higher stress as compared to the single pore. This is quite likely due to the lack of a material medium for stress propagation and in the case of an edge or a pore the stress tends to amplify. In the case of square-shaped pore, the stress concentration is observed at the intersection of the two edges of the pore in the case of single pore CAD model. This concentration is observed to propagate further in the case of two square-shaped pores CAD model as discussed in the above sections. However, the area between the two pores tend to form a shape that of a vertical column and exhibit higher density of stress concentration zone which is beyond/below the measured area. In the case of cylindrical pores, the stress concentration and the stress propagation are similar to

square-shaped pores despite of cylindrical curvature present inside the pore. But the stress concentration zone observed in the columnar structure between the square-shaped pores is not observed in the case of cylindrical pores. The stress concentration zone in the case of rhombus-shaped pore is observed on the left side of the pore i.e. towards the edge. Though the measured area also shows nodes exhibiting maximum stress, but the density of stress concentration is higher in the area near the edge. In the case of two pores rhombus-shaped CAD model, the area of the stress concentration zone is observed to increase between the two pores. The maximum stress concentration zone on the left of the left pore in the two pore model (see Figure 58) is observed to reduce as compared to the same zone in the case of single pore CAD model.

Chapter 6 Summary and concluding thoughts.

12% (mole) ceria doped zirconia is used in engineering applications and excitingly, it also shows the shape memory effect owing to the underlying martensitic transformation. However, the ability to utilize this effect is arrested due to the brittle nature of the material as it undergoes fracture before the structure undergoes the martensitic transformation. This largely can be attributed to the stress accumulation at the grain boundaries and triple junctions in the polycrystalline microstructure when the structure undergoes compression leading to the fracture. The microstructure is developed due to the thermal treatment and the associated solid-state diffusion which is an inevitable process in the processing of ceramic structures. As mentioned in the literature in the earlier chapters, this limitation was circumvented by using micro-structures that could aid in the dissipation of the energy through the unconstrained large faces of the grains upon compression.

AM that shows the potential to fabricate complex geometries and may be used as a process to produce complex ceramic structures. Largely, the AM process is bifurcated into powder-based and slurry based AM processes. By using both techniques, ceramic structures that can exhibit the stress-induced phase transformation can be fabricated.

In this study 12% (mole) ceria doped zirconia was investigated for its stress and temperature-induced phase transformation, which underlies the shape memory effect. One of the objectives in this work was to maximise the stress-induced phase transformation by leveraging the microstructure/mesostructure. This was primarily done by using techniques from the AM domain with a view to mitigate the inherent limitations of this material.

The effect of morphology of CZ particles on stress-induced phase transformation.

The particles of the as received CZ powder were monocrystalline and thermally treating it led to thermal-induced phase transformation reducing its ability to undergo martensitic transformation. However, this was accompanied by a change in the morphology of the particle. Primarily by using techniques like W.H. plot method and the Scherrer equation, the change in strain and the particle size was characterised in the powder and the compressed pellet. It was observed that with the increase in thermal treatment temperature the particle size also increases but the strain is observed to decrease. The growth of the particle size would play a vital role in the release of the residual strain. A similar trend was observed in the case of pellets as well. However, the strain in peak T(101) was observed to be higher in the case of pellets as compared to the powder; this is in contrast to the other peaks. This is quite likely due to the deconvolution of the tetragonal peak into two monoclinic peaks. Further to this, the residual stress calculated shows that the stress generated at the granular level is much higher than the stress applied for compaction.

The change in the morphology was characterised using both AFM and TEM images which showed the evolution of particle surface from quasi-spherical edges to straight faceted edges. In the case of AFM, the increase in the unevenness is remarkably higher at 900°C as compared to 300°C, but at 1550°C it is observed to be smooth and with large grains. Though AFM clearly showed that the change in morphology was evident but the change in every single particle was only seen clearly in the TEM images. The first regime showed a negative correlation between stress-induced and thermal-induced transformation. The monoclinic content is gradually increasing from 300°C to 1200°C (Regime I) beyond which (>1200°C, Regime II), the growth of monoclinic content is limited. At liquid nitrogen temperature, CZ is known to undergo phase transformation but the powder after being exposed to liquid nitrogen temperature showed MC similar to the as-received CZ powder thereby showing resistance to phase transformation.

The morphology characterisation using AFM techniques showed that the variation in the Z range increases as the temperature increases and the drop is observed above 1200°C. The inclination angle of the peaks is observed to increase, i.e. the steepness increases as the thermal treatment temperature increases. Further to this, the radius of curvature also show that the features tend to get sharper. The morphology characterisation was further done using TEM images to corroborate with the evidence gathered from the AFM images. In the TEM images it was observed that the increasing straight edges, corners and facet length of the particles in Regime I strongly supported the presumption that sharp features evolve as a function of temperature. Further to this the sphericity that would influence the compaction is also observed to reduce as the thermal treatment temperature increases. In the case of facets, the density of sharp features on the surface of CZ nanoparticles increases with higher thermal treatment temperature. This confirms the fact that irrespective of AFM or TEM, i.e. in the bulk scale or at the nanoscale, the formation of sharp facets and the evolution of sphericity due to thermal treatment is evident and their contribution as stress concentrators aids in the growth of monoclinic content during stress-induced phase transformation.

Slurry based additive manufacturing

The idea of stress concentrator was further investigated in bulk sintered ceramic structures through the use of pores. Ideally, the structures fabricated using conventional processing techniques are dense and polycrystalline. The polycrystallinity issues concerning excess stress accumulation at grain boundaries can be solved using oligocrystalline or single-crystal structures but the feasibility of producing such structures for bulk applications is not economical if feasible. Pores are reported to act as stress concentrators aiding in optimising stress observed in the microstructure. Therefore the pores were investigated as a way forward in integrating shape memory ceramics for bulk applications.

The slurry-based technique showed that the polymer and other aids could homogenously hold the ceramic particles in a certain shape thereby retaining the structure as a whole. The slurry thus produced using a combination of generic SU-8 and ceramic powder was used to cure basic structures in order to characterise the cure depth as a function of energy dosage. This information was then further used to design the process flow of fabricating ceramic pillars. Taking into consideration the limitation of the stereolithography setup in the Z-direction, only single layer structures could be fabricated. Therefore, a pseudo-3D printing process was developed that used a combination of stereolithography and tape casting process. Each pellet fabricated composes of homogenously distributed ceramic particles and it depicts a single layer as in the case of AM. Several such single-layered pellets were stacked on top of each other to form structures using either P3P or MP3P process.

Initially, surface techniques were used to characterise the phase transformation in CZ. Polishing was used to produce stress-induced phase transformation and it was further characterised using XRD. The strongest peaks T (101) and monoclinic peaks associated with M (111) and M (11-1) showed variation before and after polishing in sintered pillars. To reverse the stress-induced phase transformation using thermal treatment, 500°C was used as thermal treatment temperature on the pillars and a significant drop was observed in the intensity of the monoclinic peaks. To produce localised stress-induced phase transformation, Vickers indenter was used to produce indents and Raman spectroscopy was used to characterise the change in the phases in and around the indents. The spectra obtained from the centre and edge of the indent, 100 and 200 microns on the left and right of the indent showed change and increase in the intensity of the monoclinic peaks confirming phase transformation. The objective of this study was to qualitatively conclude the effect of localised stress and aggressive polishing in inducing stress-induced phase transformation.

The MC produced after polishing was observed to increase during compression. This growth shows a linear increase at the lower applied stress levels but saturates at, the higher applied stress levels. A saturation level around 80 - 90 MPa was observed and compressing the P3P pillars above these stress levels resulted in the fracture of the pillars. The growth of the monoclinic phase in the sub-critical stress regime was observed to increase above 25 MPa but apparently on further compression it saturates above 75 MPa. The difference between MC after polishing and post-compression is also observed to increase as a function of stress.

In the case of MP3P pillars, the pillars could withstand much higher applied stresses and at these levels, nucleation/formation of the monoclinic phase was observed. The formation of the monoclinic phase in this process was without an auxiliary process and it increased further with cyclic loading.

CZ pellets showed nucleation and substantial increase at the same stress levels estimated around the pores from FEA simulation. The cyclic loading revealed saturation of the MC and further compression at higher stresses showed no significant increase, resulting in plateauing of MC, suggesting no fresh nucleation.

Characterisation of stress distribution using FEA

Compression of the P3P, MP3P and PCP pillars showed the limits of stress that can be achieved/sustained in the pillars and the corresponding nucleation/growth of the monoclinic phase. However, the stress distribution around the pores which effectively would play a crucial role in the possible formation/growth of the monoclinic phase in the bulk wasn’t clear. This was analysed using FEA by designing CAD models that would represent the porosity and the shape of the pores observed in the microstructure of the P3P pillars. Initially, the comparison validated the fact that

optimised stress levels were observed around the periphery of the pore with the largest diameter as compared to a dense same sized CAD model.

FEA of CAD models representing the P3P pillars showed that stress concentration and variation are higher in porous as compared to non-porous structures at stresses sustained by the pillars in both regimes. Inclination towards negative skew in porous models in both stress regimes implied more nodes undergoing stresses as compared to dense models. The variation in stress levels is observed around the voids suggesting uniformity in FEA but very limited dependence on the size of the void. Though the maximum stress was highly localised around the void with the largest diameter, further propagation in the bulk was observed to saturate despite the increase in applied stress in the lower stress regime.

Similar such findings were observed in the FEA of CAD models representing the distribution of pores in the MP3P pillars. But it was observed that the density of stress concentration was higher as compared to the P3P pillars in the region between the pores. This shows the possibility of producing optimised stress concentration zones by increasing porosity i.e. the distance between the two pores. Based on this consideration further investigation was done on the basis of pore fraction and pore shape in different CAD models.

In the case of increasing the pore fraction, the distance between the pores would decrease and this was observed to be relatively denser areas of stress concentration since separate stress concentration zones of two separate pores would merge together to form a bigger zone.

By reducing the distance between the pores, it was observed that the zone of maximum stress shifted from the left in the case of single pore CAD model to between the two pores in the case of

two-pore CAD model. The stress concentration zone area is bigger if the distance between two pores is lesser, implying that the possibility of higher stress-induced phase transformation.

In the case of varying the shape of the pore, all the shapes showed optimised stress levels around the pore periphery. The maximum stress was observed in the case of the two-pore layout with square-shaped pores. Further to this it was also observed that the density of the nodes sustaining the maximum stress is higher in the square-shaped pores as compared to other shaped pores. The region between the two square-shaped pores is in the shape of vertical column. This vertical column bears resemblance to the shape of the micropillars with high surface area to volume ratio which could sustain the critical stress and thereby exhibit the shape memory behaviour. In the case of this vertical section being able to accommodate the strain produced during the martensitic transformation, the structure in the bulk could display the shape memory behaviour. This highlights the transition from polycrystalline microstructure to oligocrystalline and further to single-crystal structures despite in bulk applications. These results from the FEA analysis highlight that with the advent of AM wherein higher control can be shown in designing a porous microstructure such structures can be fabricated with effective accuracy. This would, in essence, mitigate the brittle fracture but also aid in exhibiting the shape memory effect in bulk applications.

Section 6.1: Future work

Future work on the effect of thermal treatment on CZ and its subsequent effect on stress-induced phase transformation.

The thermally treated CZ powder can be used in powder-based AM techniques. Ceramic structures which can be 3D printed with, e.g. CZ powder thermally treated at 1100°C will have a maximum number of facets and straight edges, compression of which can aid in optimised levels of MC

which may not be possible in the case of non-thermal treated CZ powder. This is similar to the granular packings of shape memory ceramics which exhibit the stress-induced phase transformation, but the only difference is that the particles are single crystal and therefore have large constraint-free surface area as compared to larger (micron) sized particles comprising of two or more grains. Thus, stress accumulation at the grain boundaries can be avoided in the case of single-crystal particles. This is further to the optimised stress-induced phase transformation seen due to the faceting and the associated stress concentration in the CZ nanoparticles.

Taking into consideration that sintering is a crucial step in the post-processing of ceramic structures techniques like spark plasma sintering (SPS) can be used for sintering. SPS technique has shown evidence of retaining the morphology post sintering despite densifying the structure [114], [115]. This would densify the structure made from faceted particles of CZ and quite likely would retain the shape and the facets in the particles besides the effective formation of mechanical properties.

Also, in regime II, the sudden drop and rise in MC form interesting results. This is most likely due to the necking which forms between particles resulting in the force distribution over a larger area. However, this hypothesis requires further investigation and thus would be an important part of future work.

In the work focused on thermal treatment of pellets for the optimised tetragonal phase recovery, the results showed both peak temperature and dwell time at peak temperature dependence. So further investigations should be focused on analysing the tetragonal phase recovered as a function of peak temperature and as dwell time at peak temperature independently.

Future work on the slurry-based pseudo-3D printing and the related stress-induced phase transformation.

The P3P pillars could not sustain applied stress above ~90 MPa due to the weak internal structure that was resulting in failure. Though saturation in MC was observed, refinement in the engineering process flow can be done to improve the capability of the structure to sustain higher stresses. The adhesion between pellets can be improved by exploring methods in vacuum suction to remove air pockets between pellets that would essentially expand during de-binding and sintering. Also, slower heating during both de-binding and sintering process can be used as methods to improve inter-pellet bonding.

Taking into consideration that the shape memory effect hinges on the structures capability to sustain critical stress levels, a valid indicator would be the optimised levels of the MC. Therefore, quenching the pillars with a view to introduce dislocations in the ceramic pillars and then subject them to compression could quite possibly optimise stress-induced phase transformation. The dislocations and the energy associated with the dislocations would interact with the different levels of stresses developed in the bulk of the pillar during compression. This interaction between the elastic energy of the dislocations and the stress might produce future prospects in optimising stress-induced phase transformation.

Future directions in microstructure optimisation based on FEA analysis

The findings of these simulations suggest that the shape of the pore plays a vital role in optimising the stress in the bulk of the structure. In the case of AM, each single layer can be accurately and precisely cured and therefore the overall shape or the pore can be effectively defined in the microstructure. The details from the FEA can be integrated with powder-based AM methods to

produced optimised stress levels in the bulk. Similar such approach can also be used in the case of slurry-based techniques using stereolithography. However, due considerations need to be taken in the case of sintering, since sintering would enlarge the size of the pores and possibly distort sharp features around the pores in the case of conventional sintering techniques. This would limit the stress optimisation capabilities in the regions around the pores. Also, it is worth noting that pores would offer free surfaces to grains in the vicinity of the pores. The deformation associated with the martensitic transformation can be accommodated in the case of columnar structure between two square shaped pores. However, this can also lead to brittle fracture, hence considerations in this direction need to be taken.

References

[1] W. D. Callister, *Materials Science and Engineering: An Introduction.* .

[2] M. Bengisu, *Engineering Ceramics*. .

[3] "General classification of ceramics [SubsTech]." [Online]. Available: https://www.substech.com/dokuwiki/doku.php?id=general_classification_of_ceramics. [Accessed: 11-Jun-2019].

[4] "Young's Modulus - Density." [Online]. Available: http://www-materials.eng.cam.ac.uk/mpsite/interactive_charts/stiffness-density/NS6Chart.html. [Accessed: 11-Jun-2019].

[5] "Ionic and covalent bonding [SubsTech]." [Online]. Available: https://www.substech.com/dokuwiki/doku.php?id=ionic_and_covalent_bonding. [Accessed: 11-Jun-2019].

[6] "Zirconia (Zirconium Oxide, ZrO2) | Fine Ceramics (Advanced Ceramics) | KYOCERA." [Online]. Available: https://global.kyocera.com/prdct/fc/list/material/zirconia/zirconia.html. [Accessed: 04-Oct-2019].

[7] P. F. Manicone, P. Rossi Iommetti, and L. Raffaelli, "An overview of zirconia ceramics: Basic properties and clinical applications," *J. Dent.*, vol. 35, no. 11, pp. 819–826, 2007.

[8] C. Piconi and G. Maccauro, "Review Zirconia as a biomaterial," *Compr. Biomater.*, vol. 1, pp. 95–108, 2011.

[9] J. H. Lee, “Review on zirconia air-fuel ratio sensors for automotive applications,” *J. Mater. Sci.*, vol. 38, no. 21, pp. 4247–4257, 2003.

[10] X. J. Jin, “Martensitic transformation in zirconia containing ceramics and its applications,” *Curr. Opin. Solid State Mater. Sci.*, vol. 9, no. 6, pp. 313–318, 2005.

[11] P. Duwez and F. Odell, “Phase Relationships in the System Zirconia-Ceria,” *Netsu Sokutei*, vol. 24, no. 4, pp. 171–178, 1997.

[12] P. F. Becher and M. V. Swain, “Grain-Size-Dependent Transformation Behavior in Polycrystalline Tetragonal Zirconia Paul,” *J. Am. Ceram. Soc.*, vol. 75, no. 3, pp. 493–502, 1992.

[13] R. H. J. Hannink, P. M. Kelly, and B. C. Muddle, “Transformation Toughening in Zirconia-Containing Ceramics,” *J. Am. Ceram. Soc.*, vol. 83, no. 3, pp. 461–487, 2004.

[14] H. A. Rauch, Y. Chen, K. An, and H. Z. Yu, “In situ investigation of stress-induced martensitic transformation in granular shape memory ceramic packings,” *Acta Mater.*, vol. 168, pp. 362–375, 2019.

[15] J. Chevalier, L. Gremillard, A. V. Virkar, and D. R. Clarke, “The tetragonal-monoclinic transformation in zirconia: Lessons learned and future trends,” *J. Am. Ceram. Soc.*, vol. 92, no. 9, pp. 1901–1920, 2009.

[16] K. Ōtsuka and C. M. Wayman, *Shape memory materials*. Cambridge University Press, 1998.

[17] P. E. Reyes-Morel and I. -W Chen, “Transformation Plasticity of CeO2-Stabilized Tetragonal Zirconia Polycrystals: I, Stress Assistance and Autocatalysis,” *J. Am. Ceram. Soc.*, vol. 71, no. 5, pp. 343–353, 1988.

[18] A. Lai, Z. Du, C. L. Gan, and C. A. Schuh, “Shape memory and superelastic ceramics at small scales.,” *Science*, vol. 341, no. 6153, pp. 1505–8, 2013.

[19] X. M. Zeng, A. Lai, C. L. Gan, and C. A. Schuh, “Crystal orientation dependence of the stress-induced martensitic transformation in zirconia-based shape memory ceramics,” *Acta Mater.*, vol. 116, pp. 124–135, 2016.

[20] Z. Du, X. M. Zeng, Q. Liu, C. A. Schuh, and C. L. Gan, “Superelasticity in micro-scale shape memory ceramic particles,” *Acta Mater.*, vol. 123, pp. 255–263, 2017.

[21] X. Song, Y. Chen, T. W. Lee, S. Wu, and L. Cheng, “Ceramic fabrication using Mask-Image-Projection-based Stereolithography integrated with tape-casting,” *J. Manuf. Process.*, vol. 20, pp. 456–464, 2015.

[22] L. Gorjan, G. Blugan, T. Graule, and J. Kuebler, “Effectiveness of wick-debinding inside powder bed for ceramic laminates made by tape casting,” *Powder Technol.*, vol. 273, pp. 197–202, 2015.

[23] J. W. Halloran, “Ceramic Stereolithography: Additive Manufacturing for Ceramics by Photopolymerization,” *Annu. Rev. Mater. Res*, vol. 46, pp. 19–40, 2016.

[24] Z. Du *et al.*, “Synthesis of monodisperse CeO 2 -ZrO 2 particles exhibiting cyclic superelasticity over hundreds of cycles,” *J. Am. Ceram. Soc.*, vol. 38, no. 1, pp. 42–49, 2017.

[25] X. Zhao, A. Lai, and C. A. Schuh, “Shape memory zirconia foams through ice templating,” *Scr. Mater.*, vol. 135, pp. 50–53, 2017.

[26] H. Z. Yu, M. Hassani-Gangaraj, Z. Du, C. L. Gan, and C. A. Schuh, “Granular shape memory ceramic packings,” *Acta Mater.*, vol. 132, pp. 455–466, 2017.

[27] X. Zeng, Z. Du, C. A. Schuh, and C. L. Gan, “Enhanced shape memory and superelasticity in small-volume ceramics: A perspective on the controlling factors,” *MRS Commun.*, vol. 7, no. 4, pp. 747–754, 2017.

[28] A. S. Wagh, R. B. Poeppel, and J. P. Singh, “Open pore description of mechanical properties of ceramics,” *J. Mater. Sci.*, vol. 26, no. 14, pp. 3862–3868, 1991.

[29] C. YP, “On the Stress Field Due to Initial Strains in a Cuboid Surrounded by an Infinite Elastic Space.,” *J. Appl. Mech*, vol. 44(4), pp. 587–590, 1977.

[30] L. Gremillard, J. Chevalier, T. Epicier, and G. Fantozzi, “Improving the Durability of a Biomedical-Grade Zirconia Ceramic by the Addition of Silica,” *J. Am. Ceram. Soc.*, vol. 85, no. 2, pp. 401–7, 2002.

[31] “Additive Manufacturing v/s Subtractive Manufacturing - MANUFACTUR3D.” [Online]. Available: https://manufactur3dmag.com/additive-manufacturing-v-s-subtractive-manufacturing/. [Accessed: 12-Jun-2019].

[32] I. Denry and J. R. Kelly, “State of the art of zirconia for dental applications,” *Dent. Mater.*, vol. 24, no. 3, pp. 299–307, 2008.

[33] T. O. Mason, “Advanced Ceramics,” *Encycl. Br.*, vol. 5456, no. January, 2015.

[34] E. Traversa, “Ceramic sensors for humidity detection: the state-of-the-art and future developments,” *Sensors Actuators B. Chem.*, vol. 23, no. 2–3, pp. 135–156, 1995.

[35] N. Q. Minh, “Ceramic Fuel Cells,” *J. Am. Ceram. Soc.*, vol. 76, no. 3, pp. 563–588, 1993.

[36] T. E. Strangman, “Thermal barrier coatings for turbine airfoils,” *Thin Solid Films*, vol. 127, no. 1–2, pp. 93–106, 1985.

[37] A. Zocca, P. Colombo, C. M. Gomes, and J. Günster, "Additive Manufacturing of Ceramics: Issues, Potentialities, and Opportunities," *J. Am. Ceram. Soc.*, vol. 98, no. 7, pp. 1983–2001, 2015.

[38] Z. X. Khoo *et al.*, "3D printing of smart materials: A review on recent progresses in 4D printing," *Virtual Phys. Prototyp.*, vol. 10, no. 3, pp. 103–122, 2015.

[39] A. Sydney Gladman, E. A. Matsumoto, R. G. Nuzzo, L. Mahadevan, and J. A. Lewis, "Biomimetic 4D printing," *Nat. Mater.*, vol. 15, no. 4, pp. 413–418, 2016.

[40] T. Chartier *et al.*, "Additive manufacturing to produce complex 3D ceramic parts," *J. Ceram. Sci. Technol.*, vol. 6, no. 2, pp. 95–104, 2015.

[41] J. Gardan, "Additive manufacturing technologies: state of the art and trends," *Int. J. Prod. Res.*, vol. 7543, no. August, pp. 1–15, 2015.

[42] R. A. Day, J. D. Gelorme, D. J. Russell, and S. J. Witt, "US-5304457," pp. 0–3, 1994.

[43] C. Cremers, F. Bouamrane, L. Singleton, and R. Schenk, "SU-8 as resist material for deep X-ray lithography," *Microsyst. Technol.*, vol. 7, no. 1, pp. 11–16, 2001.

[44] A. Del Campo and C. Greiner, "SU-8: a photoresist for high-aspect-ratio and 3D submicron lithography," *J. Micromechanics Microengineering*, vol. 17, no. 6, pp. R81–R95, 2007.

[45] M. L. Griffith and J. W. Halloran, "Freeform Fabrication of Ceramics via Stereolithography," *J. Am. Ceram. Soc.*, vol. 79, no. 10, pp. 2601–2608, Aug. 1996.

[46] O. O. Omatete, M. a. Janney, and S. D. Nunn, "Gelcasting: From laboratory development toward industrial production," *J. Eur. Ceram. Soc.*, vol. 17, no. 2–3, pp. 407–413, 1997.

[47] C. Müller, T. Hanemann, G. Wiche, C. Kumar, and J. Goettert, "Fabrication of ceramic

microcomponents using deep X-ray lithography," *Microsyst. Technol.*, vol. 11, no. 4–5, pp. 271–277, 2005.

[48] S. P. Gentry and J. W. Halloran, "Depth and width of cured lines in photopolymerizable ceramic suspensions," *J. Eur. Ceram. Soc.*, vol. 33, no. 10, pp. 1981–1988, 2013.

[49] J. W. Halloran *et al.*, "Photopolymerization of powder suspensions for shaping ceramics," *J. Eur. Ceram. Soc.*, vol. 31, no. 14, pp. 2613–2619, Nov. 2011.

[50] S. P. Gentry and J. W. Halloran, "Absorption effects in photopolymerized ceramic suspensions," *J. Eur. Ceram. Soc.*, vol. 33, no. 10, pp. 1989–1994, 2013.

[51] S. P. Gentry and J. W. Halloran, "Light scattering in absorbing ceramic suspensions: Effect on the width and depth of photopolymerized features," *J. Eur. Ceram. Soc.*, vol. 35, no. 6, pp. 1895–1904, 2015.

[52] T. Chartier, A. Badev, Y. Abouliatim, P. Lebaudy, and L. Lecamp, "Stereolithography process: Influence of the rheology of silica suspensions and of the medium on polymerization kinetics - Cured depth and width," *J. Eur. Ceram. Soc.*, vol. 32, no. 8, pp. 1625–1634, 2012.

[53] T. Chartier, C. Chaput, F. Doreau, and M. Loiseau, "Stereolithography of structural complex ceramic parts," *J. Mater. Sci.*, vol. 37, no. 15, pp. 3141–3147, 2002.

[54] R. E. Chinn, *Ceramography : Preparation and Analysis of Ceramic Microstructures*. ASM International, 2002.

[55] H. X. Zhu and A. H. Windle, "Effects of cell irregularity on the high strain compression of open-cell foams," *Acta Mater.*, vol. 50, no. 5, pp. 1041–1052, 2002.

[56] H. Zhu, J. R. Hobdell, and A. H. Windle, “Effects of Cell Irregularity on the Elastic Properties of Open-Cell Foams Effects of Cell Irregularity on the Elastic Properties of Open-Cell Foams,” *J. Mech. Phys. Solids*, vol. 49, no. 4, pp. 857–870, 2000.

[57] S.-Y. Chung, C. Lehmann, M. Abd Elrahman, and D. Stephan, “Pore Characteristics and Their Effects on the Material Properties of Foamed Concrete Evaluated Using Micro-CT Images and Numerical Approaches,” *Appl. Sci.*, vol. 7, no. 6, p. 550, 2017.

[58] A. E. Simone and L. J. Gibson, “Aluminum foams produced by liquid-state processes,” *Acta Mater.*, vol. 46, no. 9, pp. 3109–3123, 1998.

[59] M. Kunze, HD; Baumeister, J; Banhart, J; Weber, “P/M Technology for the production of metal foams,” *Powder Metall. Int.*, vol. 25, no. 4, pp. 182–185, 1993.

[60] D. J. McGregor, S. Tawfick, and W. P. King, “Mechanical properties of hexagonal lattice structures fabricated using continuous liquid interface production additive manufacturing,” *Addit. Manuf.*, vol. 25, no. November 2018, pp. 10–18, 2019.

[61] S. Yan, Y. Huang, D. Zhao, F. Niu, G. Ma, and D. Wu, “3D printing of nano-scale Al2O3 –ZrO2 eutectic ceramic: Principle analysis and process optimization of pores,” *Addit. Manuf.*, vol. 28, no. April, pp. 120–126, 2019.

[62] J. Wilkes, Y. C. Hagedorn, W. Meiners, and K. Wissenbach, “Additive manufacturing of ZrO2-Al2O3ceramic components by selective laser melting,” *Rapid Prototyp. J.*, vol. 19, no. 1, pp. 51–57, 2013.

[63] H. Yves-Christian, W. Jan, M. Wilhelm, W. Konrad, and P. Reinhart, “Net shaped high performance oxide ceramic parts by Selective Laser Melting,” *Phys. Procedia*, vol. 5, no.

PART 2, pp. 587–594, 2010.

[64] A. G. Athanassiadis *et al.*, “Particle shape effects on the stress response of granular packings,” *Soft Matter*, vol. 10, no. 1, pp. 48–59, 2014.

[65] R. Kandasami and T. Murthy, “Effect of particle shape on the mechanical response of a granular ensemble,” in *Geomechanics from Micro to Macro*, 2014, no. November 2016, pp. 1093–1098.

[66] G.-C. Cho, J. Dodds, and J. C. Santamarina, “Particle Shape Effects on Packing Density, Stiffness, and Strength: Natural and Crushed Sands,” *J. Geotech. Geoenvironmental Eng.*, vol. 132, no. 5, pp. 591–602, 2006.

[67] A. B. Yu and N. Standish, “Characterisation of non-spherical Particles From Their Packing Behaviour,” *Powder Technol.*, vol. 74, pp. 205–213, 1993.

[68] R. D. Hryciw, M.ASCE, J. Zheng, S.M.ASCE, K. Shetler, and S.M.ASCE, “Particle Roundness and Sphericity from Images of Assemblies by Chart Estimates and Computer Methods,” *J. Geotech. Geoenvironmental Eng.*, vol. 142, no. 1935, p. 360, 2016.

[69] R. P. Zou and A. B. Yu, “Evaluation of the packing characteristics of mono-sized non-spherical particles,” *Powder Technol.*, vol. 88, no. 1, pp. 71–79, 1996.

[70] K. Krumbein and W. C. Krumbein, *Stratigraphy and sedimentation*. 1951.

[71] T. P. Meloy, “Fast Fourier Transforms Applied to Shape Analysis of Particle Silhouettes to obtain Morphological Data,” *Powder Technol.*, vol. 17, pp. 27–35, 1977.

[72] J. P. Hyslip and L. E. Vallejo, “Fractal analysis of the roughness and size distribution of granular materials,” *Eng. Geol.*, vol. 48, no. 3–4, pp. 231–244, 1997.

[73] Y. Li, “Effects of particle shape and size distribution on the shear strength behavior of composite soils,” *Bull. Eng. Geol. Environ.*, vol. 72, no. 3–4, pp. 371–381, 2013.

[74] Y. Fu and A. G. Evans, “Some effects of microcracks on the mechanical properties of brittle solids—I. Stress, strain relations,” *Acta Metall.*, vol. 33, no. 8, pp. 1515–1523, Aug. 1985.

[75] H. Gao, L. Zhang, W. D. Nix, C. V. Thompson, and E. Arzt, “Crack-like grain-boundary diffusion wedges in thin metal films,” *Acta Mater.*, vol. 47, no. 10, pp. 2865–2878, 1999.

[76] A. E. Jakus, N. R. Geisendorfer, P. L. Lewis, and R. N. Shah, “3D-printing porosity: A new approach to creating elevated porosity materials and structures,” *Acta Biomater.*, vol. 72, pp. 94–109, 2018.

[77] J. Maurath and N. Willenbacher, “3D printing of open-porous cellular ceramics with high specific strength,” *J. Eur. Ceram. Soc.*, vol. 37, no. 15, pp. 4833–4842, 2017.

[78] A. García, I. Izquierdo-Barba, M. Colilla, C. L. De Laorden, and M. Vallet-Regí, “Preparation of 3-D scaffolds in the SiO 2 -P 2 O 5 system with tailored hierarchical meso-macroporosity,” *Acta Biomater.*, vol. 7, no. 3, pp. 1265–1273, 2011.

[79] L. C. Hwa, S. Rajoo, A. M. Noor, N. Ahmad, and M. B. Uday, “Recent advances in 3D printing of porous ceramics: A review,” *Curr. Opin. Solid State Mater. Sci.*, vol. 21, no. 6, pp. 323–347, 2017.

[80] “Fundamentals of Direct-Ink-Writing | Manufacturing Processes and Machinery Lab | Washington State University.” [Online]. Available: https://labs.wsu.edu/mpml/projects/. [Accessed: 30-Aug-2020].

[81] M. V Swain and R. H. J. Hannink, “Metastability of the martensitic-transformation in a 12

mol-percent ceria zirconia alloy .2. Grinding studies," *J. Am. Ceram. Soc.*, vol. 72, no. 8, pp. 1358–1364, 1989.

[82] C. Mochales *et al.*, "Monoclinic phase transformations of zirconia-based dental prostheses, induced by clinically practised surface manipulations," *Acta Biomater.*, vol. 7, no. 7, pp. 2994–3002, 2011.

[83] R. C. Garvie and P. S. Nicholson, "Phase Analysis in Zirconia Systems," *J. Am. Ceram. Soc.*, vol. 55, no. 6, pp. 303–305, 1972.

[84] E. D. Whitney, "Kinetics and Mechanism of the Transition of Metastable Tetragonal to Monoclinic Zirconia," *Trans. Faraday Soc.*, vol. 61, pp. 1991–2000, 1965.

[85] B. D. Cullity and S. R. Stock, *Elements of x-ray diffraction*, 3rd ed. Prentice Hall.

[86] G. K. Williamson and W. H. Hall, "X-RAY LINE BROADENING FROM FILED ALUMINIUM AND WOLFRAM," *Acta Metall.*, vol. 1, p. 22, 1953.

[87] A. Khorsand Zak, W. H. Abd. Majid, M. E. Abrishami, and R. Yousefi, "X-ray analysis of ZnO nanoparticles by Williamson-Hall and size-strain plot methods," *Solid State Sci.*, vol. 13, no. 1, pp. 251–256, 2011.

[88] X.-D. Zhou and W. Huebner, "Size-induced lattice relaxation in CeO2 nanoparticles," *Appl. Phys. Lett.*, vol. 79, no. 21, pp. 3512–3514, 2001.

[89] C. Suciu, L. Gagea, A. C. Hoffmann, and M. Mocean, "Sol-gel production of zirconia nanoparticles with a new organic precursor," *Chem. Eng. Sci.*, vol. 61, no. 24, pp. 7831–7835, 2006.

[90] M. M. R. Boutz, A. J. A. Winnubst, and A. J. Burggraaf, "Yttria-Ceria Stabilized Tetragonal

Zirconia Polycrystals: Sintering, Grain Growth and Grain Boundary Segregation," *J. Euopean Ceram. Soc.*, vol. 13, pp. 89–102, 1994.

[91] R. H. Dauskardt, D. K. Veirs, and R. O. Ritchie, "Spatially Resolved Raman Spectroscopy Study of Transformed Zones in Magnesia-Partially-Stabilized Zirconia," *J. Am. Ceram. Soc.*, vol. 72, no. 7, pp. 1124–1130, 1989.

[92] K. Tsukuma and M. Shimada, "Strength, fracture toughness and Vickers hardness of CeO2-stabilized tetragonal ZrO2 polycrystals (Ce-TZP)," *J. Mater. Sci.*, vol. 20, no. 4, pp. 1178–1184, 1985.

[93] A. Savin *et al.*, "Monitoring techniques of cerium stabilized zirconia for medical prosthesis," *Appl. Sci.*, vol. 5, no. 4, pp. 1665–1682, 2015.

[94] "Stereographic Projection of Crystal Faces." [Online]. Available: https://www.tulane.edu/~sanelson/eens211/stereographic_projections.htm. [Accessed: 27-Aug-2019].

[95] V. S. Raut, T. S. Glen, H. A. Rauch, H. Z. Yu, and S. T. Boles, "Stress-induced phase transformation in shape memory ceramic nanoparticles," *J. Appl. Phys.*, vol. 215109, no. November, 2019.

[96] R. C. Garvie and M. V. Swain, "Thermodynamics of the tetragonal to monoclinic phase transformation in constrained zirconia microcrystals - Part 1 In the absence of an applied stress field," *J. Mater. Sci.*, vol. 20, no. 4, pp. 1193–1200, 1985.

[97] I. Chen and P. E. Reyes-Morel, "Implications of transformation plasticity in ZrO2-containing ceramics: I, Shear and dilatation effects," *J. Am. Ceram. Soc.*, vol. 69, no. 3, pp.

181–89, 1986.

[98] I. W. Chen and Y. H. Chiao, “Theory and experiment of martensitic nucleation in ZrO2 containing ceramics and ferrous alloys,” *Acta Metall.*, vol. 33, no. 10, pp. 1827–1845, Oct. 1985.

[99] A. H. Heuer, N. Claussen, W. M. Kriven, and M. Ruhle, “Stability of Tetragonal ZrO2 Particles in Ceramic Matrices,” *J. Am. Ceram. Soc.*, vol. 65, no. 12, pp. 642–650, 1982.

[100] D. Nečas and P. Klapetek, “Gwyddion: an open-source software for SPM data analysis,” *Open Phys.*, vol. 10, no. 1, pp. 181–188, Jan. 2012.

[101] H. Z. Yu and C. V. Thompson, “Correlation of shape changes of grain surfaces and reversible stress evolution during interruptions of polycrystalline film growth,” *Appl. Phys. Lett.*, vol. 104, no. 14, 2014.

[102] J. R. Heffelfinger and C. B. Carter, “Mechanisms of surface faceting and coarsening,” *Surf. Sci.*, vol. 389, no. 1–3, pp. 188–200, 1997.

[103] Herring Conyers, “Some Theorems on the Free Energies of Crystal Surfaces,” *Phys. Rev.*, vol. 82, no. 1, pp. 87–93, 1951.

[104] W. W. Mullins, “Theory of linear facet growth during thermal etching,” *Philos. Mag.*, vol. 6, no. 71, pp. 1313–1341, 1961.

[105] C. M. Phillippi and K. S. Mazdiyasni, “Infrared and Raman Spectra of Zirconia Polymorphs,” *J. Am. Ceram. Soc.*, vol. 54, no. 5, pp. 254–258, 1971.

[106] Y. Gaillard, M. Anglada, and E. Jiménez-Piqué, “Nanoindentation of yttria-doped zirconia: Effect of crystallographic structure on deformation mechanisms,” *J. Mater. Res.*, vol. 24,

no. 03, pp. 719–727, 2009.

[107] H. Zhu, T. Hirata, and Y. Muramatsu, “Phase Separation in 12 mol% Ceria-Doped Zirconia Induced by Heat Treatment in H2 and Ar,” *J. Am. Ceram. Soc.*, no. m, pp. 2843–2848, 1992.

[108] H. T and Z. H, “RAMAN STUDY OF THE PHASE SEPARATION IN ZrO2-12 mol% CeOz CERAMIC,” *Solid State Commun.*, vol. 80, no. 12, pp. 991–994, 1991.

[109] P. E. Reyes-Morel, J.-S. Cherng, and I.-W. Chen, “Transformation Plasticity of Ce02-Stabilized Tetragonal Zirconia Polycrystals: II, Pseudoelasticity and Shape Memory Effect,” *J. Am. Ceram. Soc.*, vol. 71, no. 8, pp. 648–57, 1988.

[110] C. M. Wayman, “The phenomenological theory of martensite crystallography: Interrelationships,” *Metall. Mater. Trans. A*, vol. 25, no. 9, pp. 1787–1795, 1994.

[111] M. Skovgaard, A. Ahniyaz, B. F. Sørensen, K. Almdal, and A. van Lelieveld, “Effect of microscale shear stresses on the martensitic phase transformation of nanocrystalline tetragonal zirconia powders,” *J. Eur. Ceram. Soc.*, vol. 30, no. 13, pp. 2749–2755, 2010.

[112] T. Davis, D. Healy, A. Bubeck, and R. Walker, “Stress concentrations around voids in three dimensions: The roots of failure,” *J. Struct. Geol.*, vol. 102, pp. 193–207, 2017.

[113] J. C. (John C. Jaeger, N. G. W. Cook, and R. W. Zimmerman, *Fundamentals of rock mechanics*. Blackwell Pub, 2007.

[114] M. Cologna, B. Rashkova, and R. Raj, “Flash sintering of nanograin zirconia in <5 s at 850°C,” *J. Am. Ceram. Soc.*, vol. 93, no. 11, pp. 3556–3559, 2010.

[115] J. G. Santanach, A. Weibel, C. Estourns, Q. Yang, C. Laurent, and A. Peigney, “Spark plasma sintering of alumina: Study of parameters, formal sintering analysis and hypotheses

on the mechanism(s) involved in densification and grain growth," *Acta Mater.*, vol. 59, no. 4, pp. 1400–1408, 2011.

[116] J. Wu, X. Guo, A. P. Zhang, and H. Y. Tam, "Rapid 3D micro-printing of optical whispering-gallery mode resonators," *IEEE-NANO 2015 - 15th Int. Conf. Nanotechnol.*, vol. 23, no. 23, pp. 1271–1273, 2016.

Chapter 7 Appendix

Section 7.1: Appendix I

Characterisation of cure depth

Materials and experimental methods

Cure depth characterisation of ZrO_2 using stereolithography

The stereolithography setup as shown in Figure 63 consists of a high power ultraviolet light source procured from (OmniCure 2000 System, Lumen Dynamic Group Inc.) and a high-speed spatial light modulator, i.e. digital micro-mirror device (DMD, DLi4120 0.7" XGA, Texas Instruments). A bitmap image of the structure to be fabricated is stored in the DMD device through an in-house software. This image is then projected through a lens system on top of a spin-coated quartz substrate [116].

Zirconia is procured from Sigma Aldrich and 16% (mole) ceria doped zirconia from Ganzhou Wanfeng Advanced MaterialsTech. Co. Ltd. China. The slurry formulated for stereolithography had a ceramic solid loading of 30% (vol.) and SU-8 consisting the remaining composition. The SU-8 photoresist is producusing EPON SU-8 resin (Momentive Ltd.), Tributylamine (TBA) (Meryer Chemical Technology Co., Ltd.) and PC-2506 (Polyset) as a photo inhibitor and ultraviolet polymerization catalyst respectively. The resin and photopolymerisation species are then dissolved in cyclopentanone (CP) in a weight ratio of 24:0.0325:0.6:23.2674 (SU-8 resin:TBA:PC-2506:CP). The raw materials are then mixed using a magnetic stirrer and hotplate setup. The slurry is spin-coated on a quartz substrate followed by a pre-bake and then exposed to the ultraviolet light aided curing of the bitmap image. The curing is followed by a hard bake for

cross-linking of the polymer. Later the substrate is immersed in a crucible of propylene glycol monomethylether (PGMEA) to remove uncured slurry and retain the cured structure.

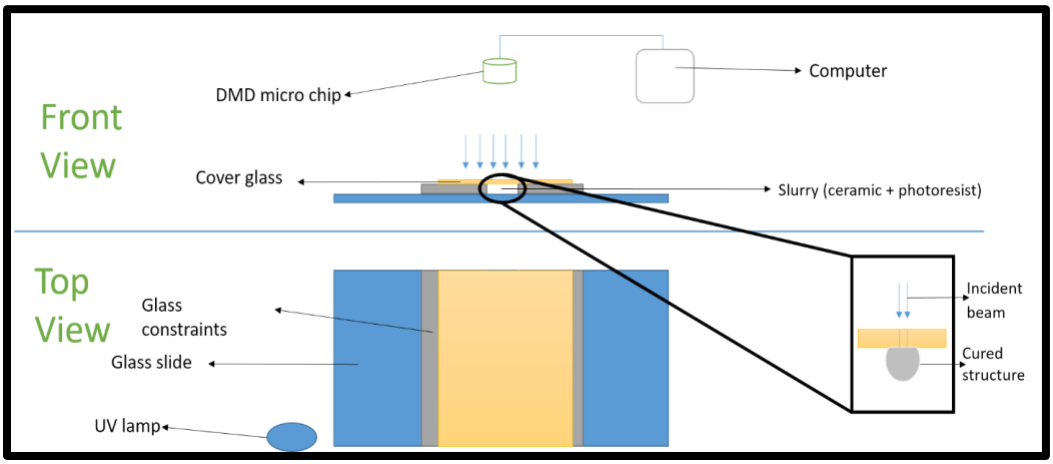

Figure 63 Assembly of the stereolithography setup is shown above in two parts, front view and top view. The Digital Micro-Mirror is loaded with the bitmap images of the mask using the computer. The UV lamp shown in the Top View focuses the incident beam on the DMD, which reflects through a lens system on the cover glass.

A wide spectrum of dosages can be generated by controlling the combinations of the intensity of the UV lamp and the amount of time to be provided for each exposure. The power generated in mW/cm^2 by the UV lamp source in the stereolithography setup was measured for various intensities using a power meter. The energy dose is then calculated by taking the product of power generated for a given intensity and time (s). Figure 64 shows the energy dosage as a function of intensity multiplied by the time in s. The thickness of the structures cured is then plotted against the energy dosage.

The thickness of the cured structures is below 100 microns, so a profilometer was used to measure their height. The depth profile of a rectangular cured structure is shown in Figure 65. Similar structures to that shown in Figure 63 were cured and their depth profiles measured. The cure depths

as a function of energy dosages are shown in Figure 67. It can be observed from the graph that the cure depth increases as a function of energy dosage. Zirconia is a high refractive index ceramic hence it requires a large energy dose for a significant cure [49].

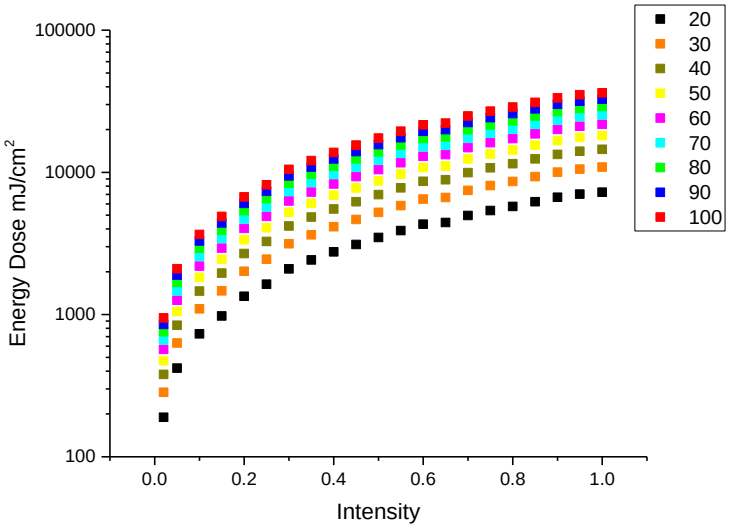

Figure 64 Energy dosage generated by the stereolithography setup calculated as a product of power generated for a given percentage of intensity of the lamp (mW/cm^2) and time (seconds) shown in the rectangular box.

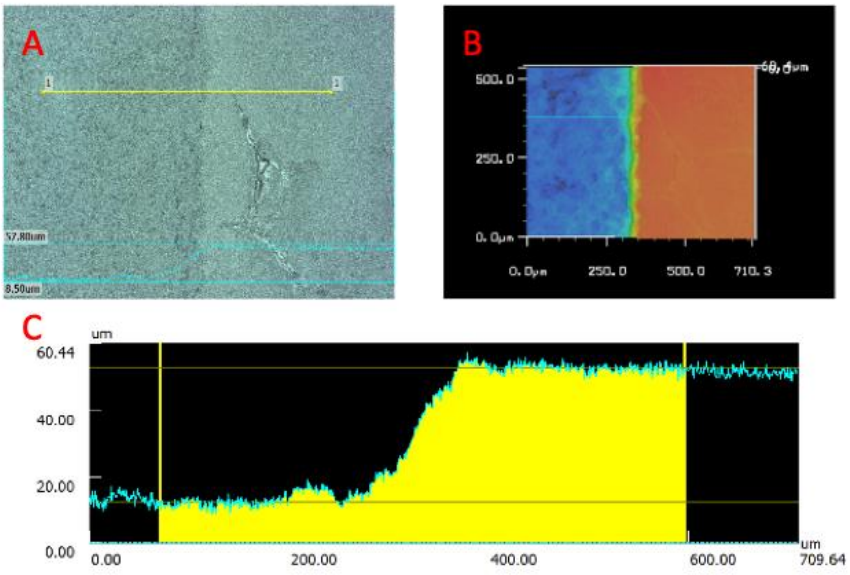

Figure 65 Laser-based Profilometer was used to measure the cure depth of the cured profile. Image (A) shows the top view of the cured structure which has the yellow marker line which defines the region of interest for the measurement. Image (B) show the topography of the substrate with the cured structures at a higher elevation in red and the uncured region in blue with an interface between them. Image (C) is a graphical reconstruction of the cross-section of cured structure based on the data from Image (B) and the two perpendicular lines are the two-end point of the horizontal marker line in image (A).

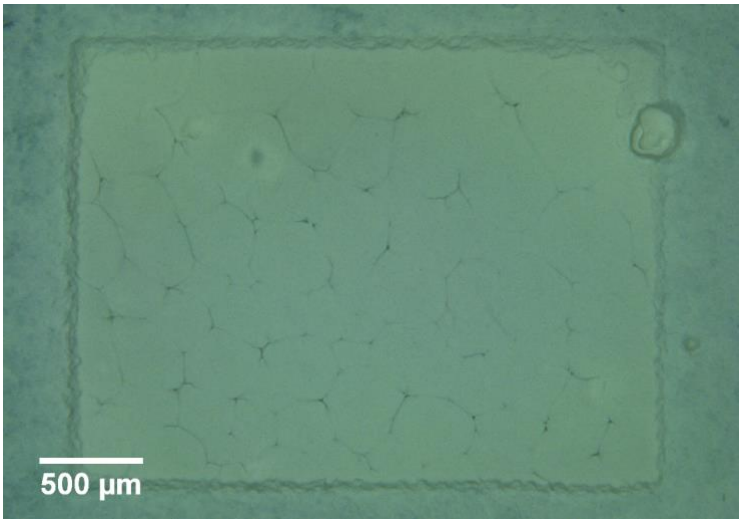

Figure 66 Rectangular profile cured using stereolithography setup.

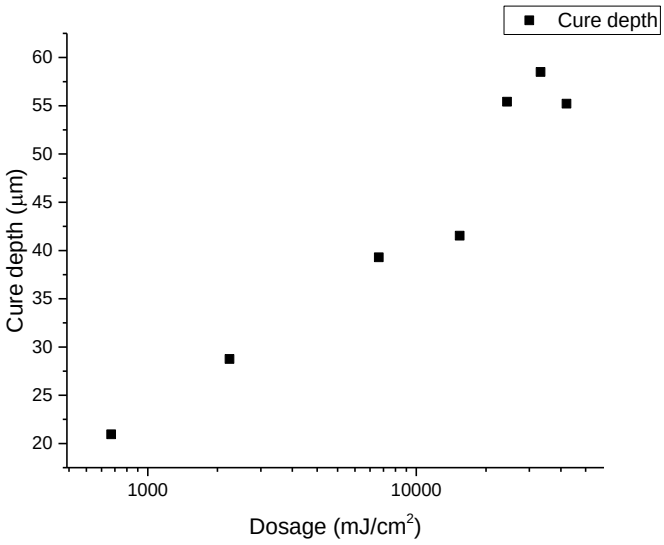

Figure 67 Cure depth characterised using Profilometer for pure zirconia with a solid loading of 25 vol. %.

By using micro stereolithography, initially, it was attempted to produce micro high aspect ratio structures. Subsequently at lower volume ceramic loadings cure depth was characterised. But on increasing the volume loading the cure depth saturated and there was significant distortion of the UV energy. Besides, pre-bake causing the slurry to harden and adhere to the substrate preventing curing of any structure. 16% (mole) ceria doped zirconia slurry with 30% solid loading showed structure up to 60 microns could be produced. It is apparent from the findings that high-resolution structure can quite likely be produced. Though broadening could be expected besides the excess hardening of the slurry due to pre-bake. Sintering at different stages above 1100°C reveal evolving grain size. At 1100°C the grain size is small so it cannot be quantified, but above 1200°C the grain size is measured to be around 300 nanometres and it increases gradually up to 3500 nanometres. Porosity fraction at 1350°C is 0.45 and at 1550°C is 0.35 which is quite likely due to densification observed at higher temperatures. Vickers hardness of around 9 GPa was observed in samples sintered at 1550°C which is quite similar the literature reported elsewhere. The objective of this study was to characterise the minimum feature size for a given energy dose with a given solid loading in the slurry. With limited manoeuvrability in the Z direction to scale the fabrication process in order to produce macroscale structures, based on the findings of this section process flow was refined.

Section 7.2: Appendix II

Table 1: Dimension of the pillars used for compression testing with the measured stress in P3P pillars.

Applied stress (MPa)	**Area** mm^2	**Height** mm
77.61	32.21	4.88
61.67	40.52	5.98
69.59	32.21	5.44
84.63	35.45	4.85
42.63	33.45	5.17
22.08	38.79	5.68
40	37.9	5.73
31.6	25.45	6.16
12.07	34.11	3.61
88.5	33.9	2.8

Table 2 Stress measured in 3D printed pillars during compression and calculated equivalent constraints for FEA simulation in the lower stress regime.

Applied stress (MPa)	**P3P**		**FEA (input)**	**FEA (output)**	
	Area m^2 (10^{-5})	**Load kN**	**Equivalent Load N**	**Stress minimum MPa**	**Stress maximum MPa**
77.61	3.22	2.5	0.78	3.1882	257.6
61.67	4.05	2.5	0.62	2.533	204.69
69.59	3.22	2.24	0.7	2.8586	230.96
84.63	3.55	3	0.85	3.4762	280.86
42.63	3.35	1.43	0.43	1.751	141.47
22.08	3.88	0.86	0.22	0.9072	73.298
40	3.79	1.52	0.4	1.6428	132.73
31.6	2.55	0.81	0.32	1.297	104.85
12.07	3.41	0.41	0.12	0.4958	40.062
88.5	3.39	3	0.88	3.635	293.69

Table 2: Dimension of the pillars used for compression testing with the measured stress in the higher stress regime.

Applied stress (MPa)	**Area** mm^2	**Height** mm
124	94.687	8.06
275	89.08	7.14
288	84.94	7.6
214	91.2	3.95

Table 3: Stress measured in 3D printed pillars during compression and calculated equivalent constraints for FEA simulation in the higher stress regime.

Applied stress (MPa)	**MP3P**		**FEA inputs**	**FEA**	
	Area m^2 (10^{-5})	**Load kN**	**Equivalent Load N**	**Stress minimum MPa**	**Stress maximum MPa**
124	9.47	11.772	0.186	13.363	291.22
275	8.91	24.50	0.4125	20.431	489.74
288	8.49	24.46	0.432	21.396	512.89
214	9.12	19.52	0.321	15.899	381.1

Table 5: Applied stress during compression of pellets fabricated using PCP.

Area (m^2)	**Load (tons)**	**Force (N)**	**Stress (N/M^2)**	**Stress (MPa)**
8.65E-05	1.1	10791	1.25E+08	124.75
8.17E-05	2.4	23544	2.88E+08	288.18
8.82E-05	5.4	52974	6.01E+08	600.61
	5.84	57290.4	6.50E+08	649.55
	6.29	61704.9	7.00E+08	699.60
	6.74	66119.4	7.50E+08	749.65

Section 7.3: Appendix III

Fabrication of micro pillars using micro-stereolithography

Slurry with low ceramic loading was used to fabricate high aspect ratio micro-pillars. The ceramic material used was zirconia from Sigma-Aldrich. The setup shown in Figure 63 was used to fabricate the micro-pillars. The CAD file used to fabricate these structures was made using Microsoft Paint. The CAD model consisted of an array of square-shaped structures made from 1 pixel to 5 pixels, in increments of 1 pixel. So, in the case of 1 pixel, the CAD model was a single pixel, in the case of 2 pixels it was a 2 by 2 model, in the case of 3 it was a 3 by 3 model, so on and so forth. The CAD model resembled a mask used in photolithography as compared to a 3D model in the case of stereolithography. The motivation behind doing this work was to fabricate microstructures. In Figure 68, the image on the left shows the array of micro-pillars fabricated using the mask. The single figure on the left of the array is number 1 followed by 2, 3, 4 and 5 as it moves to the right. The system could not fabricate a structure with a single pixel, however, the smallest structure that can be seen is above number 2. These structures are observed to get bigger as they move from 2 to 5. Each pixel in the digital micro-mirror device (DMD) is 2.723 microns in size. The image on the right shows a zoomed-in image of the structure made using 5 by 5-pixel slot in the mask.

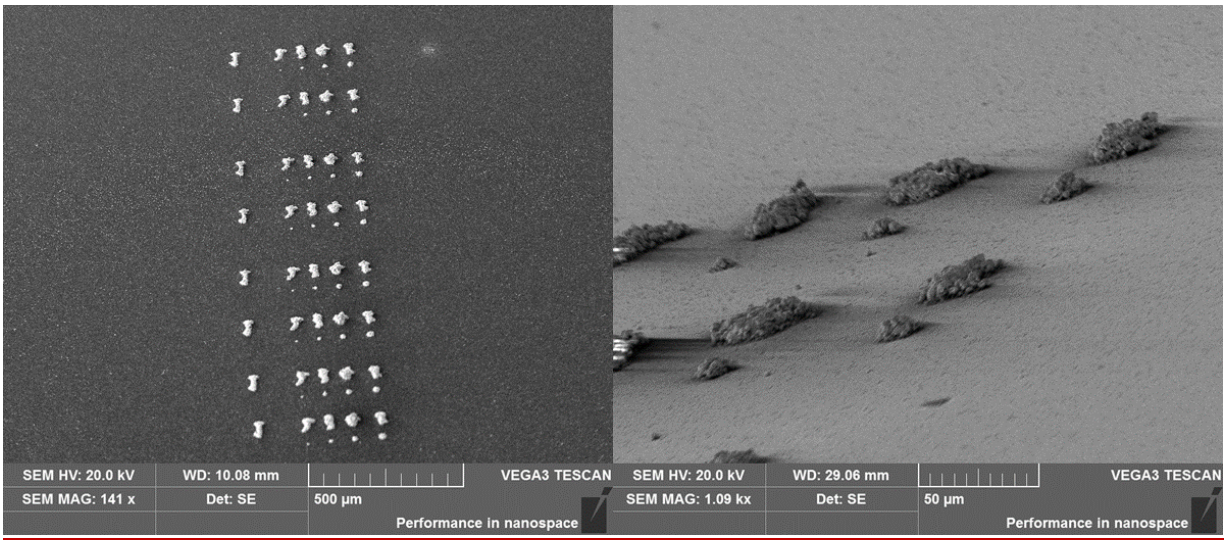

Figure 68 Image on the left shows an array of micro-pillars like structures and image on the right shows a closer view of those structures.

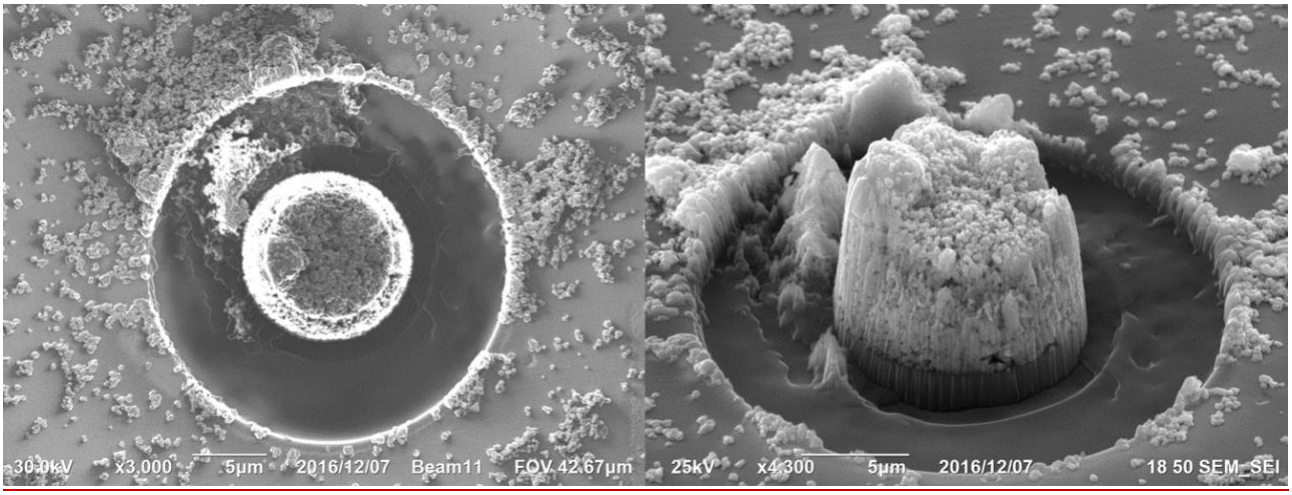

Figure 69 Image on the right shows a top view of the micro-pillar post FIB milling and image on the right shows a side view of the micro-pillar.

One such micro-pillar is FIB milled to achieve a desirable aspect ratio (2:1 height: diameter). The micro-pillars are to be designed on the lines of micro pillars used to exhibit the shape memory behaviour in Figure 4. The micro-pillar post FIB milling can be seen in Figure 69. In the image on

the right in Figure 69, the side view of milled-micro pillar reveals the presence of pores. The arrays of micro-pillars shown in Figure 69 were sintered at 1000°C.

The micro-pillars in Figure 4 reveal a larger size of grains and the higher surface to volume ratio in these micro-pillars eliminate the formation of the triple junction. Hence upon the application of critical stress, the structure would undergo phase transformation and the strain formed can be accommodated thereby, exhibiting the shape memory behaviour. In Figure 69 the grains are quite small or due to the lack of the sintering effect observed at a higher temperature, the initial particle size of the material has still been retained. Based on the understanding of the evolution of particle size observed in Figure 23, it suggests that the micro-pillars fabricated should be sintered at the temperatures above 1500°C. However, future work at the onset needs to focus on finding ways to remove/peel the micro-structure fabricated from the fused-silica substrate. Then these structures can be subjected to thermal treatment at a temperature above 1500°C. The thermally treated micro-structure would ideally have a grain size of ~3-5 microns which can be milled to a diameter of ~1-2 microns. The structure post-milling would thus resemble the structure shown in Figure 4. These structures can then be used for micro-compression and subsequent shape memory behaviour characterisation.

Section 7.4: Appendix IV

Mesh size analysis

To determine the right size of the mesh, different mesh sizes were used for simulations. In the case of coarse mesh the maximum stress was observed to be around 316 MPa and in the case of medium and fine mesh the maximum stress is observed to be around 306 MPa. Taking into consideration that there was no change in the maximum stress that was observed between medium and fine mesh,

the element size can be used for further simulations. Figure 70shows stress-distribution in the CAD model with coarse, medium and fine mesh size.

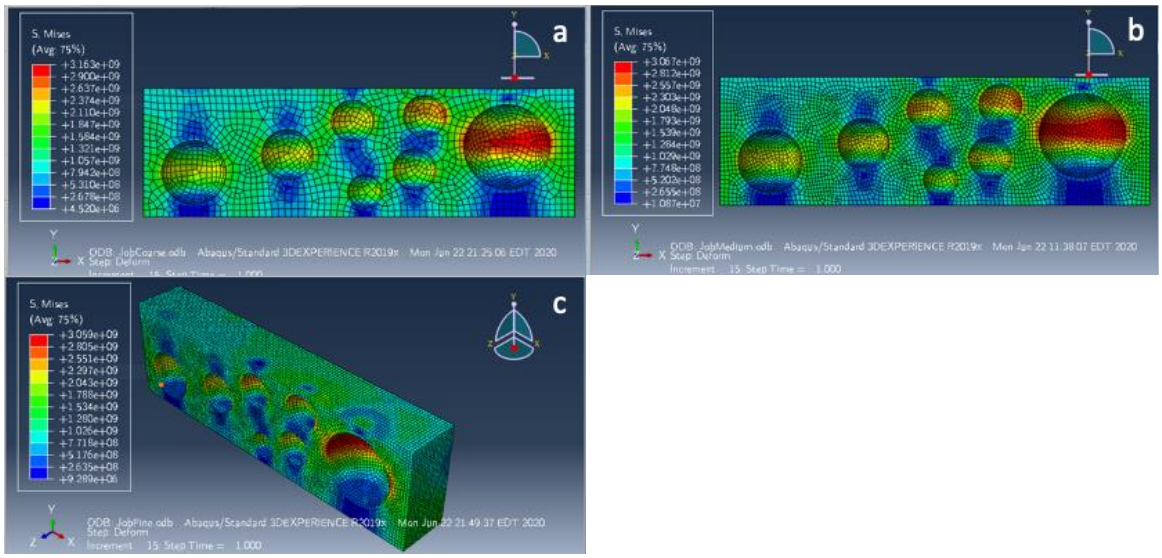

Figure 70 (a) coarse sized mesh (19690 elements), (b) medium mesh (74430 elements) and (c) fine mesh (98000 elements).

Figure 71 shows the maximum von-Mises stress observed in the CAD models with different mesh sizes as a function of the total number of nodes in the model. The coarse mesh size CAD model would have lesser number of elements as compared to medium and fine mesh with a higher number of elements.

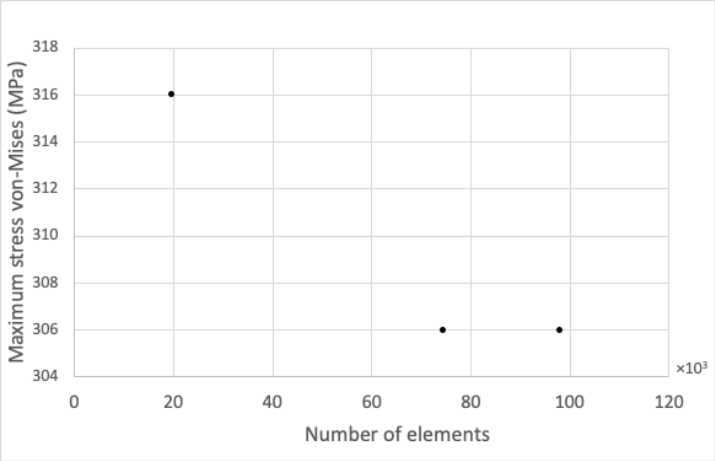

Figure 71 Maximum stress observed as a function of number of nodes/mesh size.